



The  
University  
Of  
Sheffield.

# Developing a Tip-Enhanced Fluorescence Microscope for Applications in Super-Resolution and Correlative Imaging

Amy Nadine Moores

Submitted for the Degree of Doctor of  
Philosophy  
Department of Physics and Astronomy  
University of Sheffield

September 2017



---

## ABSTRACT

---

This thesis describes the development of a tip-enhanced fluorescence microscope, based upon combining confocal fluorescence methods with a commercially-available atomic force microscope (AFM).

A microscope which is capable of simultaneous fluorescence and atomic force measurements has been realised. This has been achieved by mounting an AFM onto an inverted optical microscope, allowing the sample to be fluorescently excited from underneath. The incident position of the excitation spot at the sample can be controlled by a 2D galvanometer present in the excitation beam path. A program has been developed which aligns the laser spot with the AFM-tip by correlating sample features, and then applying a corresponding voltage to the galvanometer, in order to translate the beam towards the AFM-tip. A result of this process is that the fields-of-view of the fluorescence and atomic force images are also aligned, enabling simultaneous correlative microscopy. The benefits of performing these techniques simultaneously include eliminating the need to image over large areas with both techniques to ensure overlapping fields-of-view (as would be required if these measurements were being performed consecutively). It also unlocks the potential to track the mechanical changes of a known structure over time. Moreover, elements of the alignment program may be useful for general applications in correlative microscopy, providing an automated tool for overlaying images which have been obtained using different techniques.

Alongside simultaneous imaging, this alignment method is also a potential technique for introducing a tip-enhancement effect into this particular instrument. A method has been developed which acquires data from a single photon counting module (SPCM) and the AFM using a LabVIEW field programmable gate array (FPGA), and subsequently correlates the number of detected photons from the sample with the position of the AFM-tip at that time. Although fluorescence enhancement was not detected using this instrument, the method was sufficient enough to detect scatter as the AFM-tip made contact with the sample; this is evidence that the method can successfully measure the number of photons detected with respect to tip-sample separation and should be able to also detect an increase in photons due to enhancement, if the effect can be optimised.



---

## ACKNOWLEDGEMENTS

---

There are a large number of people without whom this work would not have been possible.

Firstly, I would like to thank my supervisor Dr Ashley Cadby. The last few years have been very busy for both of us, but he has continued to find the time to support me, even with multiple time zones between us, and the addition of a little girl! Not only did he conceive many of the original ideas for this thesis, but he has also given me a number of amazing opportunities alongside my work, particularly to travel to some incredible places. More importantly, he has trusted me to "play" with some especially expensive pieces of equipment without ever letting on how distressed he might be at the thought of it, and he has given me the freedom to explore my own ideas.

I would also like to thank all past and present members of Ashley's high-resolution imaging group in the physics department at the University of Sheffield. Your company and advice in the laboratory and office, as well as our numerous pie-and-pint evenings at the Nottingham House, have kept me sane over the last few years. In particular, I have solicited help from a number of people within the department to make various samples for testing my microscope. These people include: Dr Andy Parnell, Dr Nic Mullin, Raveen Tank and Liyana Valiya Peedikakkal. I would also like to especially thank Dr Charlotte Nicolaou, a previous member of the Cadby group who originally taught me how to use the atomic force microscope.

I have lived and worked in Sheffield for the past eight years, and I have thoroughly enjoyed every minute of it - partly due to the wonderful department that I have been a part of, but mostly due to the terrific group of friends that I have made along the way. I will miss you all greatly, but I look forward to seeing where your careers take you.

Lastly - but definitely not least - I would like to thank my family and partner. My parents in particular have always encouraged me to do whatever I want to do, and undertaking this postgraduate research degree has been no exception. I am extremely grateful to all of my friends and family for supporting me through the last four years and helping me to reach the end.

"It always seems impossible until it's done." — Nelson Mandela



---

## PUBLICATIONS AND PRESENTATIONS

---

Aspects of this thesis have previously been presented in the following:

### PRESENTATIONS

A. Moores, 'Simultaneous AFM and Fluorescence imaging - A method for aligning an AFM probe with an excitation laser', in Microscience microscopy congress, Manchester (2017), Oral and Poster presentation

A. Moores, 'Simultaneous AFM and Fluorescence imaging - A method for aligning an AFM probe with an excitation laser', in Focus on microscopy, Bordeaux (2017), Poster presentation

A. Moores, 'Developing a tip-enhanced fluorescence microscope', in Imagine symposium, Sheffield (2016), Poster presentation

A. Moores, 'Developing a tip-enhanced fluorescence microscope', in Focus on microscopy, Taipei (2016), Oral presentation

A. Moores, 'Developing a tip-enhanced fluorescence microscope for imaging protein-line samples', in Focus on microscopy, Göttingen (2015), Poster presentation

### PUBLICATIONS

A. Moores and A. Cadby, 'Simultaneous AFM and fluorescence imaging - a method for aligning an AFM-tip with an excitation beam using a 2D galvanometer', Review of Scientific Instruments, (in press).



---

## CONTENTS

---

1	Introduction	1
1.1	Light Microscopy and its Limitations . . . . .	1
1.2	Outline and Scope of this Thesis . . . . .	5
2	Background	9
2.1	Beating the Diffraction Limit: Other Forms of Microscopy	9
2.2	Theory: How Does the Technique Work? . . . . .	13
2.3	Previous Work: a Review . . . . .	17
2.3.1	Near-Field Scanning Optical Microscopy . . . . .	17
2.3.2	Apertureless Near-Field Scanning Optical Microscopy . . . . .	18
2.3.3	Other Approaches in Near-Field Scanning Optical Microscopy . . . . .	21
2.4	Summary . . . . .	22
3	Methods and Materials	33
3.1	Atomic Force Microscopy . . . . .	33
3.2	Fluorescence Microscopy . . . . .	37
3.3	Single Photon Counting Module . . . . .	40
3.4	Field Programmable Gate Array . . . . .	43
4	Building a Fluorescence Microscope	47
4.1	Introduction . . . . .	47
4.2	Method . . . . .	48
4.2.1	Experimental Arrangement . . . . .	48
4.2.2	A Customised Sample Holder . . . . .	51
4.2.3	Aligning the Optical Pathways . . . . .	52
4.3	Results . . . . .	54
4.3.1	Fluorescence Microscopy of Thin-Film Fluorescent Polymer . . . . .	54
4.3.2	Fluorescence Microscopy of Bovine Endothelial Cells . . . . .	56
4.3.3	Fluorescence Microscopy of ThermoFisher Fluospheres . . . . .	60
4.4	Discussion and Conclusion . . . . .	66
5	Using Correlative Microscopy to Align the Tip-Enhanced Fluorescence Microscope	69
5.1	Introduction . . . . .	69
5.2	Theory . . . . .	70
5.3	Method . . . . .	73

## Contents

5.3.1	The MATLAB Alignment Program . . . . .	73
5.3.2	Calibrating the Galvanometer . . . . .	74
5.3.3	Sample Preparation . . . . .	74
5.4	Results . . . . .	76
5.4.1	Demonstrating the Ability to Obtain Beam-Tip Alignment . . . . .	76
5.4.2	Demonstrating the Ability to Maintain Beam-Tip Alignment . . . . .	79
5.5	Discussion . . . . .	83
5.6	Conclusion . . . . .	86
5.7	Supplementary Information . . . . .	87
6	A Fully-Automated Correlation Program to Facilitate Microscope Alignment and Correct for Drift . . . . .	89
6.1	Introduction . . . . .	89
6.2	Theory . . . . .	90
6.2.1	Otsu Thresholding . . . . .	90
6.2.2	Cross-Correlation . . . . .	91
6.3	Method . . . . .	92
6.4	Results . . . . .	93
6.4.1	Initial Testing of the Automated Program . . . . .	93
6.4.2	Reproducing Results for Differing Samples . . . . .	94
6.5	Discussion . . . . .	100
6.6	Conclusion . . . . .	102
6.7	Supplementary Information . . . . .	103
7	Tip-Enhanced Fluorescence: a Novel Method for Detecting Tip-Enhancement . . . . .	105
7.1	Introduction . . . . .	105
7.2	Theory . . . . .	105
7.3	Method . . . . .	107
7.3.1	Creation of Data Acquisition Program . . . . .	107
7.3.2	Creation of the Histogram . . . . .	110
7.3.3	Development of Customised Coverslips to Aid Alignment . . . . .	111
7.4	Results . . . . .	112
7.5	Discussion . . . . .	117
7.6	Conclusion . . . . .	119
8	Conclusions . . . . .	121
8.1	Microscope Status . . . . .	121
8.2	Future Work . . . . .	123
A	Aligning the Tip-Enhanced Fluorescence Microscope: An Alternative Method Incorporating Lock-In Amplification . . . . .	143
A.1	Introduction . . . . .	143

A.2	Theory . . . . .	144
	A.2.1 Lock-In Amplification . . . . .	144
	A.2.2 Experimental Hypothesis . . . . .	146
A.3	Method . . . . .	146
	A.3.1 Experimental Arrangement . . . . .	146
	A.3.2 Developing a Signal-Conditioner to Assist Lock- In Amplification . . . . .	148
A.4	Results . . . . .	149
A.5	Discussion . . . . .	153
A.6	Conclusion . . . . .	156



---

## LIST OF ACRONYMS

---

AFM	atomic force microscope
ANSOM	apertureless near-field scanning optical microscopy
CNT	carbon nanotube
FIFO	first in first out
FPGA	field programmable gate array
FWHM	full width at half maximum
NA	numerical aperture
NSOM	near-field scanning optical microscopy
P <sub>3</sub> HT	poly(3-hexylthiophene-2 5-diyl)
PHB-V	poly(hydroxybutyrate-co-valerate)
QNM	quantitative nanomechanical mapping
SEM	scanning electron microscopy
SIM	structured illumination microscopy
SNR	signal-to-noise ratio
SPAD	single photon avalanche diode
SPCM	single photon counting module
SPM	scanning probe microscopy
STED	stimulated emission depletion
STM	scanning tunnelling microscopy
STORM	stochastic optical reconstruction microscopy
TEM	transmission electron microscopy
TIRF	total internal reflection fluorescence



---

## INTRODUCTION

---

### 1.1 LIGHT MICROSCOPY AND ITS LIMITATIONS

One of the main driving forces behind the research and development of microscopy is the desire to image details that are smaller in size. The push for more detail is beneficial for any field in which microscopy is used, but a classic example demonstrating the need for more powerful microscopes is in the field of microbiology, where many intracellular features in microbial samples are just nanometres in size. It could be argued that being able to image and gather information on these types of structures has never been more important, especially with the growing problem of antibiotic resistance in bacteria. Any information that we can collect on the mechanisms behind how a bacterium thrives and grows can hint at methods to prevent cell division, potentially paving the way for new antibiotics.

The performance of any optical device is defined by a parameter known as *resolution*. The resolution of traditional light microscopy is dependent upon a number of different aspects of the system. Relating the problem to cameras, one might assume that if the perfect detector can be created with an infinitesimal spacing of individual infinitesimally small pixels, a perfect imaging system can be created with the ability to image details which are infinitesimal in size. However, even if the perfect detector can be created, there is an inherent fundamental limit to resolution which arises from the diffraction effects of light: this concept is known as the *diffraction limit of resolution*.

As light from a point source in the object plane travels through a lens, it does not create a perfect point in the image plane - the image of the source is blurred. Because light is travelling through an aperture, it diffracts, creating a diffraction pattern known as an Airy disk. An intensity profile can be taken through the image, with the intensity as a function of position more commonly known in the field of optics as a *point-spread function* (see Figure 1.1). If just one point source of light is present, the position of the original source can quite

## INTRODUCTION

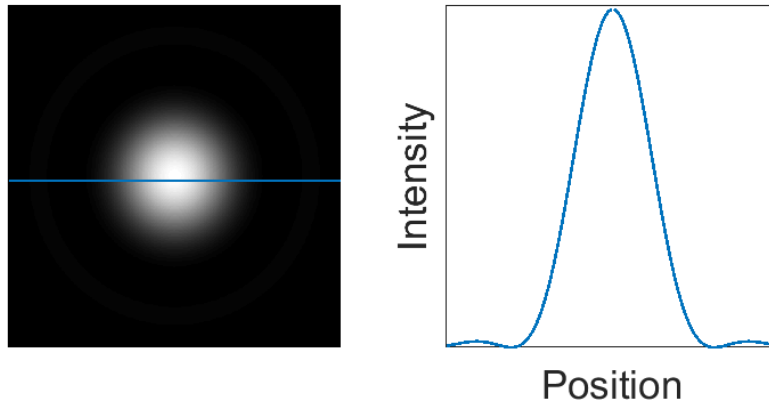


Figure 1.1.: Example of a point spread function from a single-point light source. Left is the image of a point source through a lens, displayed as an Airy disk due to diffraction effects. Taking an intensity profile (blue) through the centre of the image in any direction (here, horizontally) gives the point spread function (right).

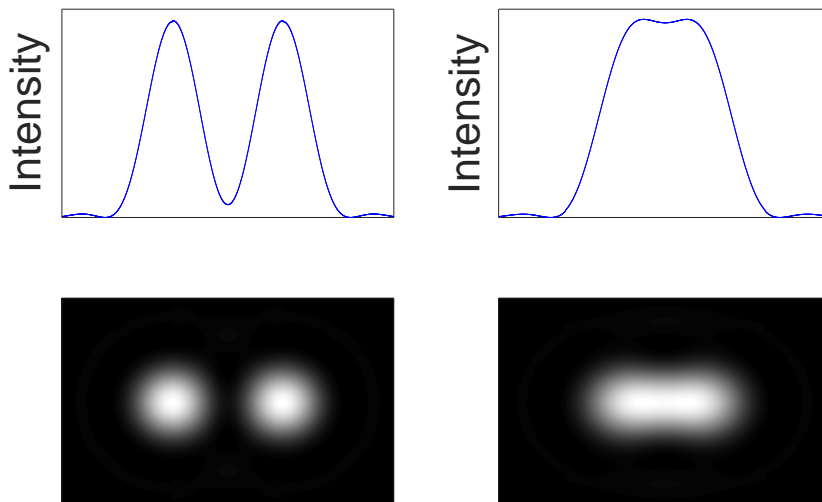


Figure 1.2.: Conditions for resolving multiple point sources of light. Left: when two pointlike sources are positioned far apart, their point spread functions can easily be distinguished, meaning that the two objects can be resolved by the optical system. If the two sources are close together (right), their point spread functions can overlap to such an extent whereby it becomes difficult to determine the number of sources present: the two objects are not resolvable by the optical system.

easily be determined - the most likely position of the original source will be the position of maximum intensity in the point spread function. However, when there are multiple sources of light close together in the object plane, they each create overlapping point spread functions in the image plane (see Figure 1.2). Once point spread functions begin to overlap, it can become very difficult to determine the positions of each of the original sources, meaning that the details which they represent become unresolvable by the optical system. In 1879 [1], Rayleigh suggested that in order for two points to be resolved, the sum of their point spread functions should drop to a value of 80 % of the maximum intensity or less [2]. It was found that, if the two point spread functions are identical, this occurs when the maximum of one overlaps with the first minima of the second in the image plane (Figure 1.3). It follows that, in order to only just be resolvable, the point spread functions should have a minimum angular separation,  $\theta_{\min}$ , given by:

$$\theta_{\min} = \frac{1.22\lambda}{D} \tag{1.1}$$

where  $\lambda$  is the wavelength of the light, and  $D$  is the diameter of the lens [2–7]. This relation is known as the Rayleigh criterion.

However this equation corresponds to an angular distance in the image plane: it does not describe the separation required in the object plane in order to resolve the two sources. This minimum linear separation can be calculated using the minimum angular separation from the Rayleigh criterion and some basic geometry (see Figure 1.4). The minimum separation between two resolvable objects  $x_{\min}$  is given by:

$$x_{\min} = f \frac{1.22\lambda}{D} = \frac{1.22\lambda}{\text{NA}} = \frac{1.22\lambda}{n \sin \alpha} \tag{1.2}$$

where  $f$  is the focal length of the lens, and numerical aperture (NA) is the ratio  $D/f$  of the lens [2] for the case of air, or more generally,  $n \sin \alpha$  [8] where  $n$  is the refractive index of the medium in which the lens is working and  $\alpha$  is the half-angle of the cone of light which can enter or exit the lens (equivalent to  $\frac{\theta}{2}$  in Figure 1.4).

Equation 1.2 is generally recognised as the resolution limit for a single lens [2]: that is, the minimum distance apart that two objects need to be in order to be resolved by the optical system. It should be noted that there are other variations on this resolution limit (such as Abbe’s limit [9] and Sparrow’s limit [10]), depending on the original

INTRODUCTION

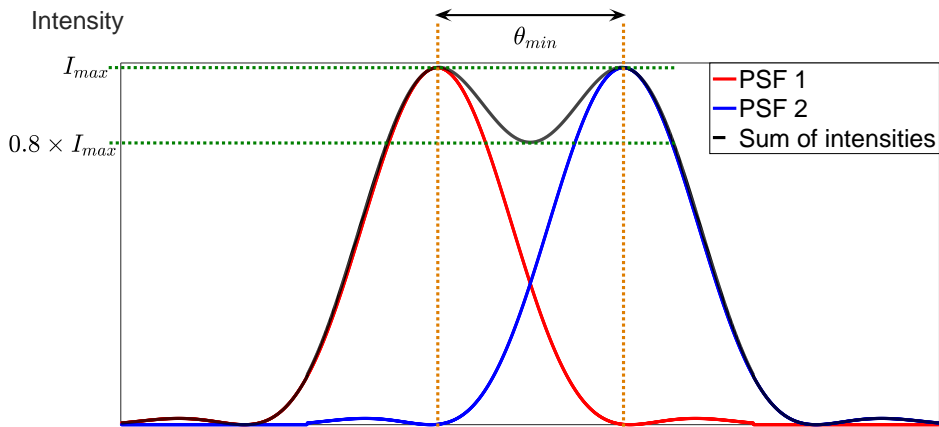


Figure 1.3.: Rayleigh criterion for two overlapping point spread functions. Two overlapping point spread functions are shown (red and blue) along with the sum of the two (black). The two point spread functions are resolvable when their sum drops to 80 % of the maximum intensity  $I_{max}$ . This is satisfied when the maximum of one point spread function overlaps with the first minima of the other, or when they are further apart than this.  $\theta_{min}$  can be described as the minimum angular separation for two point spread functions to be resolved.

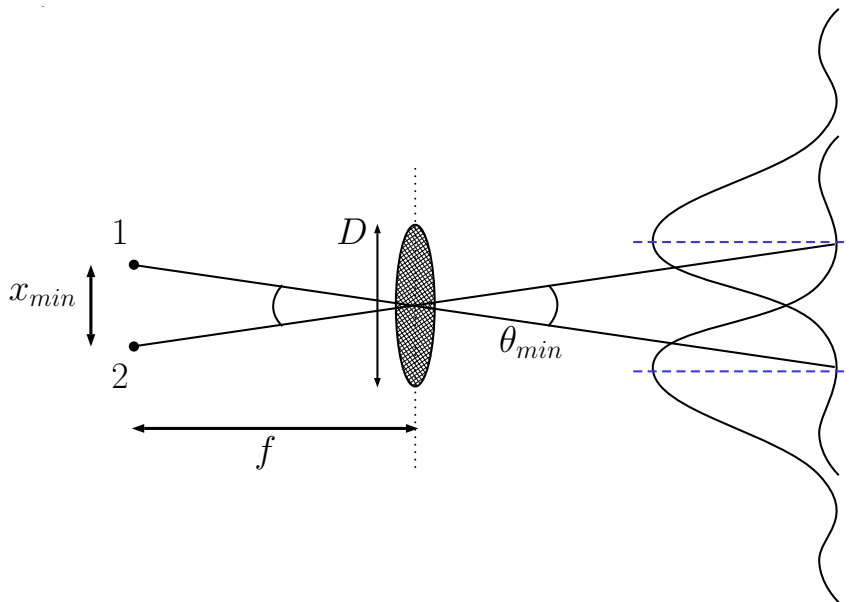


Figure 1.4.: Calculation of the resolution of the optical system  $x_{min}$  from the Rayleigh criterion. Knowing that the point spread functions need to be separated by an angle of  $\theta_{min}$  to be resolved at the image plane, the physical distance that the corresponding sources 1 and 2 need to be separated by at the object plane can be calculated.

resolving criteria. This diffraction effect is present in all microscopes which use light, and therefore all conventional light microscopes are diffraction-limited. Each microscope has its own finite resolution limit.

It can be seen from Equation 1.2 that the resolution limit for a particular optical system can be increased by either:

- increasing the NA of the lens
- decreasing the wavelength of light being used for imaging

Other methods of microscopy irradiate samples with light at much smaller wavelengths in order to make the resolution limit practically negligible (for example, in x-ray crystallography or electron microscopy): these methods will be discussed in Section 2.1.

Using the range of wavelengths in the visible light spectrum and the NA value of an oil objective<sup>1</sup>, we can expect a maximum resolution of around 300 nm with a traditional light microscope. This means that only features which are around a few hundred nanometres apart from each other will be resolvable by light microscopy. Going back to the example of microbiology, given that a single *Staphylococcus aureus* bacterium has a radius of just 500 nm, a conventional light microscope will not be useful for resolving the intracellular features of this bacteria.

In order to overcome the diffraction limit, a number of microscopy techniques have been developed over the years, including the technique being established in this thesis - tip-enhanced fluorescence microscopy. This near-field optical technique is a super-resolution method which in this case combines optical methods with scanning probe microscopy (SPM). The technique itself will be discussed in more detail in Chapter 2.

## 1.2 OUTLINE AND SCOPE OF THIS THESIS

This thesis outlines the steps towards realising a tip-enhanced fluorescence microscope via the modification of a commercially-available atomic force microscope (AFM).

Having already introduced the diffraction-limit of resolution as the main motivation behind the development of this technique, Chapter 2 begins by discussing some other microscopy methods which have been developed to overcome the inherent limit imposed on resolution. Background to the technique itself is then presented, by discussing possible

<sup>1</sup> the best performing objective lenses today have an NA value of 1.6

mechanisms for the enhancement effect and outlining the previous key works in the field.

Chapter 3 introduces some of the methods and materials that have been used in the development of the instrument and in the work performed towards this thesis.

Chapter 4 outlines the steps taken towards building the hardware of the tip-enhanced fluorescence microscope, and the field programmable gate array (FPGA) program developed for aligning the two light pathways incorporated in the microscope. The instrument at this stage functioned successfully as a confocal fluorescence microscope, onto which tip-enhancement could be incorporated with additional alignment of the two pathways with the AFM-tip, setting the foundations for the rest of this thesis.

A method for aligning the excitation beam with the AFM-tip is discussed in Chapters 5 and 6. A program was developed which correlates sample features in simultaneously acquired AFM and fluorescence images, and induces a corresponding response by the galvanometer in order to bring the excitation beam into alignment with the AFM-tip. Shown to be more reliable across the wide range of samples used in this thesis, the manual version of the program is introduced in Chapter 5. An automated version of the alignment program is outlined in Chapter 6, where it is shown that it is possible to use this technique by tailoring an image-processing algorithm to the sample being used. Alongside being used as an alignment method for tip-enhanced fluorescence microscopy, this alignment process has immediate applications in correlative microscopy, ensuring that both fluorescence and atomic force techniques are imaging exactly the same area of sample simultaneously. This unlocks the ability to track the mechanical properties of a known structure in real-time: an application which is not possible when the two techniques are being performed consecutively. Aspects of this program can also be used as a standalone overlaying tool for general purposes in correlative microscopy, whether the techniques have been performed simultaneously or otherwise.

The alignment method developed in Chapter 5 was subsequently used on the instrument for investigations into tip-enhancement. Knowing that tip-enhancement occurs for small tip-sample separations, a detection method was developed which correlates the average number of detected photons to the tip-position, in order to detect whether the fluorescence enhancement process has occurred. The results of this experiment can be found in Chapter 7.

Finally, Chapter 8 summarises and evaluates all work performed towards this thesis, and presents a recommendation for potential future works<sup>2</sup>.

REFERENCES

- <sup>1</sup>L. Rayleigh, 'XXXI. Investigations in optics, with special reference to the spectroscope', *The London, Edinburgh, and Dublin Philosophical Magazine and Journal of Science* **8**, 261–274 (1879).
- <sup>2</sup>F. L. Pedrotti, *Introduction to optics*, edited by L. S. ( S. Pedrotti, 2nd ed. (Englewood Cliffs, N.J. : Prentice Hall, c1993, Englewood Cliffs, N.J., 1993).
- <sup>3</sup>F. Graham-Smith, *Optics*, edited by J. H. ( H. Thomson and J. H. Thomson (London, London, 1971).
- <sup>4</sup>M. Born and E. Wolf, *Principles of optics:electromagnetic theory of propagation, interference and diffraction of light* (Elsevier, 1980).
- <sup>5</sup>G. A. Boutry, R. Auerbach and W. T. Wintringham, 'Instrumental optics', *Physics Today* **15**, 68–70 (1962).
- <sup>6</sup>B. Rossi, *Optics*. (Reading Mass., Reading (Mass.), 1957).
- <sup>7</sup>E. Hecht, *Schaum's outline of theory and problems of optics* (New York, New York, 1975).
- <sup>8</sup>E. Abbe, 'VII.—On the Estimation of Aperture in the Microscope.', *Journal of the Royal Microscopical Society* **1**, 388–423 (1881).
- <sup>9</sup>E. Abbe, 'Beiträge zur Theorie des Mikroskops und der mikroskopischen Wahrnehmung', *Archiv für mikroskopische Anatomie* **9**, 413–418 (1873).
- <sup>10</sup>E. Hecht, 'Optics 4th edition', *Optics, 4th Edition*, Addison Wesley Longman Inc, 1998 (1998).

---

<sup>2</sup> An additional chapter is included in the Appendix which outlines a beam-tip alignment method based on lock-in amplification that proved unsuccessful for this particular instrument.



# 2

---

## BACKGROUND

---

Tip-enhanced fluorescence microscopy - the technique which is focussed upon in this work - is a near-field super-resolution technique. The method relies upon near-field interactions between a scanning probe and the fluorescing molecule to increase the photons detected from the emitter in the far-field. The technique is also known as apertureless near-field scanning optical microscopy (ANSOM), although this can apply more generally to any optical process, not just fluorescence enhancement.

Chapter 1.1 outlined the motivation behind developing this technique; chiefly, to overcome the limit on resolution set by diffraction effects in light microscopes. This chapter begins by discussing some of the other microscopy techniques which have been developed to image at greater resolutions than that imposed by the diffraction limit. Following this, the concept of tip-enhanced fluorescence microscopy is introduced, outlining the possible mechanisms for the enhancement effect. Some of the key works in the area will also be discussed in more detail in Section 2.3.

### 2.1 BEATING THE DIFFRACTION LIMIT: OTHER FORMS OF MICROSCOPY

Several different methods have been developed in an attempt to overcome the limitation on imaging systems that is associated with the diffraction of light. A few of these methods include: electron microscopy, super-resolution microscopy and scanning probe microscopy (SPM). These categories can be differentiated further into a huge number of individual methods, all of which have their own advantages and disadvantages. This section will begin to discuss and compare some of the more popular microscopy techniques out of these three extensive categories.

Electron microscopy can be split into two main groups: transmission electron microscopy (TEM) and scanning electron microscopy (SEM).

Electron microscopy uses an accelerated beam of electrons as a source of illumination. With electrons being accelerated to energies up to 1000 keV, their de Broglie wavelength can be over 100 000 times shorter than the wavelength of visible light [11], meaning diffraction effects are negligible (as per Equation 1.2). Conventional TEM has been used to image individual light atoms such as carbon and even hydrogen [12], whilst SEMs are commercially available with resolution limits down to 0.4 nm [13]. Typically SEM has a resolution which is at least one order of magnitude poorer than TEM. However, because SEM only relies on electron scatter from the surface, the technique can be performed on large samples that are many centimetres thick. On the other hand, with TEM, there is a need for particularly thin slices of specimen (<100 nm) for sufficient transmission of electrons. Scanning transmission electron microscopes have also become available which, when corrected for spherical aberration, are capable of obtaining images at sub-Å resolution [14]. It can be said that electron microscopy remains the "gold-standard" when it comes to resolution achievements. This does not always make it the technique of choice however. For all types of electron microscopy the sample is required to be placed into a vacuum which, for biological samples in particular, can be hugely damaging. As well as this, electron microscopes are notoriously expensive to purchase and maintain [15].

An alternative to electron microscopy is SPM, which relies upon a very small probe interacting with the sample. The interaction mechanism depends entirely upon the scanning probe technique. For example, with scanning tunnelling microscopy (STM) the interaction is based upon quantum tunnelling. A bias voltage is applied between the probe and the sample, allowing electrons to tunnel through a vacuum between the two. As the tip scans across the surface, the resulting tunnelling current (which is a function of the sample height) can be monitored, allowing a topographical image to be created. STM can achieve resolutions down to a few Å and less than one Å in the lateral and vertical directions, respectively [16]. Perhaps the most popular SPM technique however is atomic force microscopy (AFM) [17]. The method uses a tip (usually about 10 nm to 20 nm in diameter) which scans over the surface of the sample in order to create a height-map. The concept of AFM is actually age-old, with Schmalz developing an instrument known as the stylus profilometer in 1929 [18]. In this first instrument, a small probe was pressed against the surface of a sample, with a beam of light being reflected off the probe onto a photographic emulsion: moving the probe across the sample allowed a magnified profile of the surface to be built up on the film [19]. With improve-

ments in probe-sharpness, scanning mechanisms and light detectors, the resolution of images from modern-day AFMs is around 0.5 nm to 2 nm in the lateral direction [20–23] and 0.1 nm to 0.2 nm in the vertical direction [23–25]. AFM can also be used for additional measurements. For instance the tip can be used to determine interaction forces between the probe and the sample, such as adhesion, as well as mechanical properties such as stiffness. Unlike STM, electrical conductivity of the sample is not required with AFM: this means that AFM is capable of imaging practically any solid moderately-flat surface without the need for special sample preparation or a vacuum [26]. The ability to obtain site-specific measurements on a wide variety of samples with high-resolution makes AFM a highly attractive technique.

AFM is a technique which is pivotal to the method developed in this thesis. The theory of AFM operation will therefore be discussed in more detail in Section 3.1.

Although the technique developed in this thesis makes use of AFM, tip-enhanced fluorescence microscopy technically falls into the final category of microscopy techniques: super-resolution microscopy. This category is perhaps the most broad of the three, which makes it difficult to draw comparisons between its different methods. To simplify things, we can separate super-resolution microscopy into far-field techniques and near-field techniques.

Of the far-field methods, an attempt can be made to further separate these into two groups. The first group is those that make use of special sample properties to achieve super-resolution images. Arguably, the most widely used of these techniques is stochastic optical reconstruction microscopy (STORM). STORM exploits special fluorophores (used to label the sample of interest) which, after excitation, readily fall into a cycle of transitioning between an optically active state and a dark state, emitting photons in the process. The probability of a particular fluorophore being in the dark state is much larger than the probability of it being in an optically active state. This means that once the whole sample is initially excited, the majority of the fluorophores in the sample will be in their dark states and only a few molecules will be emitting light at any one time. The result of this is that having two adjacent fluorophores emitting light simultaneously is highly unlikely. With no overlapping point spread functions, the individual molecules can be located at different times. With the likely positions of fluorophores being stored for each frame, a map can be created of their locations, allowing an image of the sample to be reconstructed. Two-dimensional STORM has a typical spatial resolution of around 20 nm, a ten-fold increase over the traditional diffraction limit [27, 28].

The second group within the far-field methods use different illumination or collection strategies to create super-resolution images. Two techniques to note are structured illumination microscopy (SIM) and stimulated emission depletion (STED). SIM utilises the concept of Moiré patterns - a beat pattern which appears in two superposed fine patterns - to obtain high frequency information which would otherwise be lost in a normal light microscope [29]. One of the fine patterns is the structured illumination pattern, whilst the other is that of the unknown sample structure (specifically, the unknown spatial distribution of the fluorescent molecules). The observed emission can be used to reconstruct an image of the sample structure, knowing the illumination structure. A large number of patterns have been created for structured illumination, including lines, multispots and single points [30]. Classical SIM still has a limit on its resolution - typically around half of that of Abbe's diffraction limit (approximately 100 nm) [30]. However with non-linear SIM, a resolution of 40 nm has been achieved [31, 32]. STED makes use of an illumination pattern of a different kind: in this technique, two illumination spots of different shapes are deployed. A diffraction-limited spot (around 200 nm in diameter) acts to excite the sample. Centered on top of this, a "doughnut"-shaped spot (with the same outer diameter) has a wavelength such that it quenches fluorescence. This leaves a small area in the centre of the two laser spots which continues to excite the sample. This effective excitation area has a size which is smaller than a typical diffraction-limited excitation spot, meaning that fewer molecules in the sample are excited. Previous investigations involving STED have seen spatial resolutions down to 5.8 nm for non-biological samples [33]. However the increased resolution with both non-linear SIM and STED come at a cost; for non-linear SIM, a high light intensity is required [32] and with STED, the highest resolutions are achieved when the power of the depletion beam is greatest [34]. High laser powers accelerate photobleaching of samples [30] and in some cases can damage fixed samples [32], so these techniques have limited use for biological applications, with typical resolutions of 50 nm to 70 nm being achieved by STED at more modest laser powers [35, 36].

The tip-enhanced fluorescence technique falls into the near-field category of super-resolution microscopy. Whereas the previous methods illuminate or collect emission from comparatively large-scale areas of the sample, near-field techniques rely on additional interactions with fluorescing molecules at short scale distances. Along with tip-enhanced fluorescence microscopy (which will be discussed further in Section 2.2) another key near-field technique is total internal reflection

fluorescence (TIRF). In TIRF, the illumination angle is chosen such that the excitation light is totally internally reflected off the fluorescent sample. The result of this is that strong evanescent components of light propagate into the sample; the evanescent nature of the excitation light means that the intensity reduces quickly as a function of distance travelled, causing only a very small subset of molecules that are only extremely close to the sample surface to be excited. TIRF uses low excitation depths to reduce background light [37] and autofluorescence from the sample [38], allowing a higher signal to noise ratio to be achieved. TIRF microscopy has previously been used to image fluorescent molecules with an axial resolution of around 20 nm, and a lateral resolution of <100 nm [39]. One of the benefits of TIRF is that the set-up is relatively simple and is possible to combine with other super-resolution techniques to further increase resolution or to obtain additional information, for example AFM [40] and STORM [41].

It has been shown in this section that it is not trivial to directly compare different forms of microscopy. It is certainly true that electron microscopy is capable of achieving spatial resolutions currently unrivalled by any other microscopy technique, but whether this should be the method of choice depends entirely upon the application; the strict conditions required for electron microscopy are not always suitable for the sample under test, particularly in the case of biological samples which will be damaged under vacuum. For biological samples, usually AFM or fluorescence microscopy are the preferred methods of imaging. Whilst AFM is readily capable of spatial resolutions down to less than a nanometre, it can be difficult to perform live-cell imaging with AFM because it relies upon the cell's position not being affected by the scanning probe. Fluorescence microscopy methods are suitable for both live and fixed-sample imaging as long as a fluorescent label can be found which is suitable for attachment to the particular sample. It is hoped that the technique of tip-enhanced fluorescence microscopy will 'fill the void', having the advantages of using fluorescence microscopy for specificity with biological samples, but at resolutions which stretch towards that of SPM and beyond.

## 2.2 THEORY: HOW DOES THE TECHNIQUE WORK?

Although the enhancement effect has been known about for several decades, relatively little is known about the exact mechanisms behind it. It is known that a sharp tip has the ability to modify the optical properties of a fluorescing molecule when the separation between the two becomes less than 10 nm [42–46]. However, the phenomenon

is difficult to evaluate experimentally since there are many factors which influence enhancement [44] including probe material [42], probe size [43], probe geometry [47], excitation polarization [48], tip-to-sample separation [42, 43], and the emitter itself [49–51]; these factors will be discussed in Section 2.3. Meanwhile, possible causes of the enhancement effect will be discussed in this section.

Fluorescence is a spontaneous emission process [52]: an excited molecule decays to a lower-energy state via the emission of a photon. The time that a fluorescent molecule spends in its excited state before relaxing to its ground state is known as the fluorescence lifetime [53]. It has long been known that the lifetime of an excited atomic state can be affected by its environment [54–57]. The lifetime is dictated by two competing effects: the radiative decay resulting in the emission of a photon, and non-radiative decay leading to energy being dissipated to the molecule’s surroundings [51]. In the presence of a metal surface, both of these decay rates can be modified [58, 59], potentially leading to an observed enhanced emission from fluorescent molecules, or alternatively a fluorescence quenching.

It is thought that a crucial component in tip-enhanced microscopy is the production of highly confined electromagnetic fields at the apex of a sharp probe: these confined fields can be thought of as nano-scale light sources with which to excite a highly localised area of the sample [60]. Confined fields can be generated at the tip-apex by illuminating the tip with light. The incident excitation light drives free electrons in a metallic probe along the direction of polarisation, causing charges to accumulate on the surface of the metal. The surface charges form an oscillating standing wave, known as a *surface plasmon*. In general, plasmons are oscillations occurring in a plasma: a gas of charged particles in constant motion. In the case of plasma, the charged particles are constantly moving, causing local charge fluctuations to occur. This can cause areas within the plasma with excess charge. Excess charges are repelled by their surroundings, and the velocity obtained with this repulsive force can cause the charges to overshoot their original position, which means that the charges can begin to oscillate around a fixed position. These are effectively harmonic oscillators with a quantised energy: treating these oscillations as quasi-particles leads to the concept of a *plasmon* [61, 62]. Plasmons do not only occur in plasma: free electrons can also experience a restoring force from a fixed lattice of positive ions, so plasmons can also occur in both metals and doped semiconductors [63]. The aforementioned surface plasmons are electron oscillations which exist on the interface

between a metal and a dielectric. These oscillations result in highly localised fluctuations in the electromagnetic field [48, 64].

Following simulations by various groups [48, 64, 65], tip-enhancement has been shown to depend greatly on the direction of excitation polarisation in experimental data [66]. If there is a strong component of polarisation which is perpendicular to the tip axis, there is a build up of free electrons on one side of the tip, leaving holes on the opposite side; this gives zero net charge at the tip-apex. In contrast, when there is a strong component of polarisation which is parallel to the tip axis, the surface charge density is rotationally symmetric with a net charge at the end of the tip. It is in this case that the resulting electric field is confined to a volume which is dependent upon the diameter of the tip-apex [60] thus producing a highly localised nanoscale light source which, when brought close to a fluorescing molecule, can increase the fluorescence intensity [67]. It is probable that this dipole-dipole effect is the main mechanism behind fluorescence enhancement.

Previously however, when the enhancement effect has been modelled by a dipole-dipole interaction only, theoretical measurements of the quantum yield have been vastly overestimated at very short separations between the tip and the sample [68]. The true variation of the enhancement factor with tip-sample separation has been shown to follow a trend similar to that shown in Figure 2.1 [42, 68]. It can be seen that, as the separation between the tip and the sample is reduced, the enhancement factor increases. The enhancement factor begins to reduce however, when the tip is moved to within very short range distances of the sample. It was these studies into the variation of enhancement with tip-sample separations which resulted in the discovery of a quenching effect [42], acting to reduce fluorescence at very short-range distances ( $< 2$  nm) [68, 69] between metallic tips and a fluorescent molecule. It is thought that this fluorescence quenching could be due to the dissipation of energy through non-radiative interactions, such as Förster coupling between the tip and the fluorophore [70, 71].

Taking a quantum mechanical approach, other possible mechanisms for the quenching effect include electron scattering, electron-hole excitation [72], and the production of *surface plasmon polaritons* [51]. Surface plasmon polaritons are electromagnetic excitations which arise because the incident light source may couple with surface plasmons. These propagate along the interface between the metallic tip and its surrounding medium [73]. The polaritons become more localised as the incident frequency approaches the plasmon frequency of the probing material [62]. Therefore, one would expect that the highest enhancements would occur at wavelengths closest to plasmon resonance.

## BACKGROUND

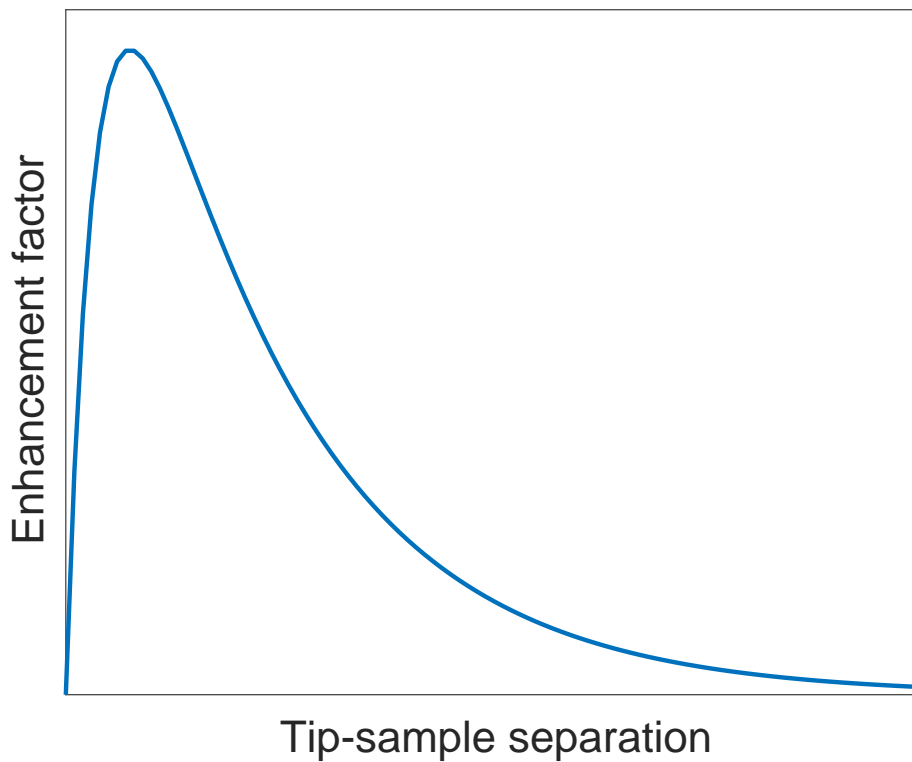


Figure 2.1.: Qualitative variation of enhancement factor with tip-sample separation [42, 68]. Enhancement factor has been shown to increase as the distance between the tip and the sample reduces, reaching a maximum at separations around 5 nm. However, when the tip is moved closer to the sample, the enhancement factor does not increase further. Instead, fluorescence quenching effects dominate, leading to a sharp reduction in overall enhancement for very small tip-sample separations ( $<2$  nm)

Curiously however, the enhancement effect has been observed for excitation wavelengths which are far away from plasmon resonance [74]. It is therefore likely that plasmonic effects are not the sole mechanism for field-enhancement.

In some studies [42, 60], a "lightning-rod" effect has been cited as the cause of enhancement, whereby a sharp tip may change the shape and strength of the electric field in its vicinity. It is suggested that the fluorescence enhancement effect is actually a combination of the two phenomena [75–78] and that plasmonic effects have the ability to further enhance the field already modified by a "lightning-rod" effect from the shape of the probe<sup>1</sup>. This is in agreement with observations of fluorescence enhancement, given that the effect has also been seen for doped-semiconductor tips which contain fewer free electrons with which to induce plasmonic effects.

### 2.3 PREVIOUS WORK: A REVIEW

This section outlines in more detail some of the factors which can affect the degree of enhancement, with the results of some key papers being discussed. Tip-enhanced fluorescence microscopy is a subset of a near-field technique called ANSOM, but is specifically applied to the enhancement of fluorescence processes. The key works in the fields of ANSOM, and of near-field scanning optical microscopy (NSOM) - from which ANSOM was developed - will be discussed in the sections to follow. Other approaches related to optimising the scanning probe in near-field investigations are also discussed in Section 2.3.3.

#### 2.3.1 *Near-Field Scanning Optical Microscopy*

NSOM is a near-field technique making use of an apertured probe with which a localised light source is delivered to the sample for fluorescence excitation. Since the size of the aperture is usually smaller than a diffraction-limited spot, images can be obtained which are better than the diffraction limit.

The basic concept of NSOM was first suggested by Synge in the 1930s [79]. Synge proposed creating an aperture with a diameter below the optical wavelength in an opaque screen, which could be illuminated from behind. This aperture could be passed over a sample at

---

<sup>1</sup> or conversely, that the plasmonic effects can also be detrimental to the field, causing fluorescence quenching

a set distance, selectively illuminating a smaller portion of the sample than would otherwise be possible through direct illumination.

Nowadays, a probe is used for delivering light. The probes used in NSOM usually take the form of an aluminium-coated dielectric tip with a transparent spot at the apex, creating an aperture [80]. Light is forced through the small metal aperture, exciting a small selection of the molecules in the sample, with their optical response being recorded to create an image. Rather than being limited by the wavelength of light, this technique has a resolution limited by the size of the sample illumination area i.e., the size of the tip-aperture [81], of which diameters of 30 nm could be achieved [82]. The technique has since successfully reported resolutions of down to  $\lambda/20$  [83–86], where  $\lambda$  is the wavelength of incident light.

Betzig et al. have investigated optimising the probes used in NSOM in several investigations [87][88]. Initial probes used in these investigations were an optical fibre which was simultaneously pulled and heated with a CO<sub>2</sub> laser, forming a uniform tapered end [87]. The sides of the fibre were then coated with aluminium, leaving the end uncoated to form an aperture. Producing the fibre in this way created a flat end face, reducing the amount of through-light that was lost due to reflection.

It is generally agreed that the resolution of NSOM is limited to 30 nm to 50 nm because of the trade-off between resolution and light throughput [89] as the aperture decreases in size, and also the finite skin depth in the metal coating setting a lower bound to resolution [42]. Moreover there are additional problems associated with NSOM [90], including the absorption of light in the aluminium coating, which causes the temperature of the tip to increase significantly [91]. This is unfavourable for biological applications as heat can be transferred to the sample, causing damage.

### 2.3.2 *Apertureless Near-Field Scanning Optical Microscopy*

ANSOM is a development which can be thought of as an extension from NSOM, although in actual fact the theoretical mechanisms of the two techniques are not at all related. Instead of being transmitted through an apertured probe, light interacts with a sharp (apertureless) tip producing an enhanced field confined to the tip apex. The amplified field conceived in ANSOM has been used to enhance various optical processes, including elastic scattering [92, 93], Raman scattering [94–96] and fluorescence excitation signals.

In 1997, Novotny et al. [48] calculated the field enhancement around gold apertureless tips (diameter = 10 nm) when illuminated by light sources ( $\lambda = 800$  nm) of both parallel and perpendicular polarisation with respect to the tip axis. It was found that when the light has a polarisation direction perpendicular to the tip, there is no field enhancement surrounding the probe. However, when illuminated with light polarised parallel to the tip axis, there is field enhancement by a factor of approximately 3000 in the vicinity of the tip. The enhanced field was found to consist of mainly evanescent components confined strongly to the end of the tip. It was also found that the enhancement factor increases with tip sharpness and laser wavelength. Novotny also found that the field was much greater for the metal gold tips than for dielectric tips.

Later however, Azoulay et al. [42] found that field enhancement was reduced from the expected value for the tungsten tips being used in their investigation. It was determined that this was because of a competition between the field enhancement and the aforementioned fluorescence quenching. Because the non-radiative decay processes are mainly associated with free electrons [72], non-radiative energy transfer occurs at a higher rate for their tungsten (or other metal) tips. Years later, in an investigation by Hamann et al. [43], it was shown that silicon probes are actually capable of achieving significant field enhancements (up to approximately 30-fold). Although this is a lower enhancement factor than is achievable with metallic probes, many groups have since opted for dielectric tips rather than metallic tips; not only does this reduce the fluorescence quenching effect, but silicon tips are generally more readily available because of their widespread use in atomic force microscopy.

More recent studies have investigated the viability of implementing the enhanced field into a fluorescence microscope capable of super-resolution. The main problem associated with tip-enhanced fluorescence for biological applications is that most samples are made up of densely-packed molecules. Once the sample is fluorescently-tagged, it is likely that multiple fluorescent molecules will be located in the excitation laser focus, causing an increase in the far-field background signal. Furthermore, because the enhancement effect is confined to a very small area (the size of the tip-apex), the fluorescence enhancement is comparable to the fluctuation of the far-field background signal. This makes the two signals difficult to separate.

To increase the signal-to-noise ratio (SNR), some groups [90, 97] have suggested using two-photon fluorescence (as opposed to one-photon fluorescence). Two-photon fluorescence is a non-linear pro-

cess, and more sensitive to the excitation laser intensity than the linear background signal. When this technique was performed by Sánchez et al., [90] a resolution of 20 nm to 30 nm was achieved. Moreover, Denk et al. [97] determined that two-photon fluorescence could be advantageous for 3D reconstruction imaging. The quadratic dependence of two-photon fluorescence on the excitation intensity means that photobleaching falls off rapidly above and below the focal plane, confining photodamage to a small layer of the sample. One layer of the specimen can therefore be imaged without causing photodamage to molecules in the other layers, enabling a 3D image to be reconstructed.

On the other hand, because two-photon fluorescence requires that two photons strike a fluorophore simultaneously, the power of the laser needs to be high to increase the chances of this occurring. With single-photon fluorescence, the peak power on the sample is lower because fewer photons need to be incident on the source [45], reducing photobleaching in the imaging plane. This means that for 2D imaging applications, using two-photon fluorescence could be detrimental. Gerton et al. [89] have shown that demodulation can successfully separate the near-field (signal) and far-field (noise) without the need for two-photon fluorescence. In their investigation, an AFM silicon probe was set to oscillate and make contact with the sample upon its closest approach; this is different to previous experiments which used very small oscillations to maintain a sample-probe gap of several nanometres. The sample used by Gerton [89] was a dried solution of CdSe-ZnS quantum dots. Using the oscillating probe, quantum dots were imaged with a lateral resolution of approximately 10 nm. Although these results are over 3 times better than other single-photon fluorescence techniques [47, 49] and approximately 2 times better than previous two-photon fluorescence techniques [90], the method can only image a sample with a high photon intensity such as a quantum dot. This renders the technique unsuitable for use with biological samples, where fluorescence molecules have a lower quantum efficiency.

To date, the most successful ANSOM development that can also be applied to biological samples is that achieved by Ma et al. [98]. Their technique has been used to obtain images of single Cy3 molecules with a sub-10 nm resolution. An oscillating silicon AFM-tip was used to probe the samples, defining a phase of oscillation  $\phi_0$  as the phase at which maximum fluorescence occurs. A filter was used to only pass photons when the phase of tip oscillation is within  $60^\circ$  of  $\phi_0$ . This means that photons are only counted when the highest signal enhancement is achieved, suppressing the noise of the background and providing an approximate six-fold improvement in the SNR [98]. 211

isolated Cy3 molecules were imaged with an average full width at half maximum (FWHM) of 8.2 nm, before two Cy3 molecules attached to either end of a strand of DNA containing 60 base pairs (approximately 15 nm in length) were successfully resolved.

### 2.3.3 *Other Approaches in Near-Field Scanning Optical Microscopy*

The main difference between the techniques of ANSOM and NSOM is that they utilise probes of different types. For NSOM, an apertured probe is used for the transmission and collection of light, whereas for ANSOM a solid tip is used to modify the electric field in the vicinity of the sample. Alternative approaches to these methods have been trialled, with the differing methods mainly consisting of changing the shape of the probe.

One example is the "tip-on-aperture" probe introduced by Frey et al. [99, 100]. The aim in producing this probe was to combine the advantages of aperture with apertureless NSOM. Light from a polarised krypton laser ( $\lambda = 568$  nm) was transmitted through a non-symmetrical aperture (70 nm in length and 30 nm in width) to illuminate a small area of a sample of DNA labelled with Cy3 fluorophores. The near field signal was enhanced by an aluminium metal tip, which is 150 nm in length and located at the aperture rim. The Cy3 dye molecules were imaged as two peaks in fluorescence intensity a distance of 30 nm apart, indicating that the resolution of the system is  $<30$  nm with many of the individual peaks displaying a FWHM as low as 10 nm [100].

Another alternative to aperture and apertureless probes are "bowtie" antennas, made up of two metallic triangles facing tip-to-tip and separated by a small gap. Schuck et al. [101] used bowtie antennas to enhance Raman scattering. It was found that intensity enhancement factors were in excess of 1000 in between the metallic triangles with the largest enhancement factors being achieved for the bowtie antennas with the smallest gap sizes ( $<30$  nm), hinting their potential to also become effective probes for fluorescence NSOM applications.

Newer investigations test the suitability of carbon nanotube (CNT)s as probes in ANSOM applications. It is thought that CNTs could provide an interesting alternative to tip-on-aperture probes because of their unique electronic properties, high axial stiffness and small diameters (1 nm to 10 nm). Following manufacture, CNTs are opened and are therefore very pliable along the radial direction. This means that the nanotube has the ability to deform, narrowing its profile as it scans over an object, potentially leading to an image with

## BACKGROUND

a finer resolution [102]. Although a spatial resolution of 20 nm was achieved using CNTs [102], there are problems associated with this type of probe. Firstly, it has been shown that fluorescence quenching occurs between quantum dots and CNTs due to energy transfer between them [103]. Secondly, the water layer that usually forms on biological samples acts as a penetration barrier for CNTs because of the hydrophobic nature of the nanotubes. This can cause the scanning probe to follow the surface of the water layer above the sample rather than the sample itself, leading to a reduction in resolution.

Many groups, including Höppener [104], have investigated the effect of attaching spherical nanoparticles to tips. Bharadwaj et al. [69] showed that spherical gold and silver nanoparticles provide sufficient field enhancement to detect the fluorescence from a single molecule. It was found that the fluorescence rate from a single Nile blue molecule could be enhanced by a factor of between 7 and 8 for both gold and silver nanoparticles when light with a wavelength of 637 nm is used. However at nanoparticle-sample separations of less than 2 nm, non-radiative decay dominates causing a reduction in fluorescence enhancement. These results support the findings of a previous experiment by Anger et al. [68], where only gold nanoparticles were used. Härtling et al. [105] examined how the diameter of the attached gold nanoparticles affected the fluorescence yield, finding that smaller diameters (down to 30 nm) did not provide sufficient enhancement to overcome the fluorescence quenching observed at small nanoparticle-sample separations. They concluded that a diameter of 80 nm achieved the best fluorescence yield. Overall, copper [67, 106–108], silver [109, 110] and gold [111] nanoparticles have all been used to enhance fluorescence. It is thought that these noble metals are particularly good at enhancing fields for fluorescence microscopy applications because the frequency of surface plasmon oscillation for these materials is in the visible region.

## 2.4 SUMMARY

The three sections in this chapter have introduced the concept of tip-enhanced fluorescence microscopy, discussing how the technique compares to other forms of microscopy and possible mechanisms behind the enhancement effect.

It is thought that the enhancement effect occurs due to a combination of phenomena. The first is a "lightning-rod" effect, brought about by a sharp tip being able to modify the shape of the surrounding electric field. The second is a plasmonic effect, due to the oscillation of

electrons in the tip-material when the tip is illuminated with light of a particular polarisation. These two effects modify the optical properties of any fluorescing molecule in the vicinity of the tip-apex, acting to alter its radiative and non-radiative decay rates, causing an increase (or in some cases, a reduction) in the number of photons being emitted by the fluorescing molecule. If the change in emission properties can be detected, higher signal-to-noise ratios can be achieved with this technique, which has led to images of <10 nm resolution [98]. It is hoped that this technique will continue to push the resolution limit down to that achieved by electron microscopy, whilst providing all of the advantages of fluorescence microscopy; chiefly, that fluorescence microscopy allows the characterisation of sample-structures due to the specificity of the fluorescent molecules and their ability to bind to particular structures, whilst being safe for use on biological samples. Previous groups have shown how the technique can be modified by changing the shape, size and material of the probe, as well as changing the method with which the probe interacts with the sample.

The work presented in this thesis will use ANSOM to enhance fluorescence processes, but it has been shown that other processes have the potential to be enhanced by the technique. Because this thesis focuses upon fluorescence, the technique will be referred to as tip-enhanced fluorescence microscopy for the remainder of this work.

#### REFERENCES

- <sup>11</sup>K. D. Vernon-Parry, 'Scanning electron microscopy: an introduction', *III-Vs Review* **13**, 40–44 (2000).
- <sup>12</sup>J. C. Meyer, C. O. Girit, M. F. Crommie and A. Zettl, 'Imaging and dynamics of light atoms and molecules on graphene', *Nature* **454**, 319 (2008).
- <sup>13</sup>Now Nanotechnology, 'Hitachi Launches World's Highest Resolution FE-SEM', [http://www.nanotech-now.com/news.cgi?story\\_id=4261](http://www.nanotech-now.com/news.cgi?story_id=4261) (2011).
- <sup>14</sup>P. D. Nellist, M. F. Chisholm, N. Dellby, O. L. Krivanek, M. F. Murfitt, Z. S. Szilagy, A. R. Lupini, A. Y. Borisevich, J. Sides William H. and S. J. Pennycook, 'Direct Sub-Angstrom Imaging of a Crystal Lattice', *Science* **305** (2004) 10.1126/science.1100965.
- <sup>15</sup>John Innes, 'Electron microscopy', [https://www.jic.ac.uk/microscopy/intro\\_EM.html](https://www.jic.ac.uk/microscopy/intro_EM.html) (2016).

## BACKGROUND

- <sup>16</sup>L. E. C. Van De Leemput and H. Van Kempen, 'Scanning tunnelling microscopy', *Reports on Progress in Physics* **55**, 1165–1240 (1992).
- <sup>17</sup>G. Binnig and F. Quate, 'Atomic Force Microscope', *Physical Review Letters* **56**, 930 (1986).
- <sup>18</sup>G. Schmalz, 'Über Glatte und Ebenheit als physikalisches und physiologisches Problem', *Verein Deutscher Ingenieure*, 1461–1467 (1929).
- <sup>19</sup>T. O. Stadelmann, *Antidot superlattices in InAs-GaSb double heterostructures: transport studies* (University of Oxford, 2006).
- <sup>20</sup>J. Mou, J. Yang and Z. Shao, 'Atomic Force Microscopy of Cholera Toxin B-oligomers Bound to Bilayers of Biologically Relevant Lipids', *Journal of Molecular Biology* **248**, 507–512 (1995).
- <sup>21</sup>D. J. Müller, F. A. Schabert, G. Büldt and A. Engel, 'Imaging purple membranes in aqueous solutions at sub-nanometer resolution by atomic force microscopy.', *Biophysical journal* **68**, 1681–6 (1995).
- <sup>22</sup>T. Walz, P. Tittmann, K. H. Fuchs, D. J. Müller, B. L. Smith, P. Agre, H. Gross and A. Engel, 'Surface Topographies at Subnanometer-resolution Reveal Asymmetry and Sidedness of Aquaporin-1', *Journal of Molecular Biology* **264**, 907–918 (1996).
- <sup>23</sup>D. Fotiadis, L. Hasler, D. J. Müller, H. Stahlberg, J. Kistler and A. Engel, 'Surface Tongue-and-groove Contours on Lens MIP Facilitate Cell-to-cell Adherence', *Journal of Molecular Biology* **300**, 779–789 (2000).
- <sup>24</sup>D. J. Müller and A. Engel, 'Voltage and pH-induced channel closure of porin OmpF visualized by atomic force microscopy', *Journal of molecular biology* **285**, 1347–1351 (1999).
- <sup>25</sup>D. J. Müller, H.-J. Sass, S. A. Müller, G. Büldt and A. Engel, 'Surface structures of native bacteriorhodopsin depend on the molecular packing arrangement in the membrane', *Journal of Molecular Biology* **285**, 1903–1909 (1999).
- <sup>26</sup>F. J. Giessibl, 'Advances in atomic force microscopy', *Reviews of modern physics* **75**, 949 (2003).
- <sup>27</sup>M. J. Rust, X. Zhuang and M. Bates, 'Sub-diffraction-limit imaging by stochastic optical reconstruction microscopy (STORM)', *Nature Methods* **3**, 793–795 (2006).
- <sup>28</sup>M. Heilemann, S. Van De Linde, M. Schüttpelz, R. Kasper, B. Seefeldt, A. Mukherjee, P. Tinnefeld and M. Sauer, 'Subdiffraction-Resolution Fluorescence Imaging with Conventional Fluorescent Probes', *Angewandte Chemie International Edition* **47**, 6172–6176 (2008).

- <sup>29</sup>M. G. L. Gustafsson, 'Surpassing the lateral resolution limit by a factor of two using structured illumination microscopy', *Journal of Microscopy* **198**, 82–87 (2000).
- <sup>30</sup>S. W. Hell et al., *The 2015 super-resolution microscopy roadmap*, 2015.
- <sup>31</sup>M. G. L. Gustafsson, 'Nonlinear structured-illumination microscopy: wide-field fluorescence imaging with theoretically unlimited resolution.', *Proceedings of the National Academy of Sciences of the United States of America* **102**, 13081–13086 (2005).
- <sup>32</sup>E. H. Rego, L. Shao, J. J. Macklin, L. Winoto, G. A. Johansson, N. Kamps-Hughes, M. W. Davidson and M. G. L. Gustafsson, 'Nonlinear structured-illumination microscopy with a photoswitchable protein reveals cellular structures at 50-nm resolution.', *Proceedings of the National Academy of Sciences of the United States of America* **109**, E135–43 (2012).
- <sup>33</sup>E. Rittweger, K. Y. Han, S. E. Irvine, C. Eggeling and S. W. Hell, 'STED microscopy reveals crystal colour centres with nanometric resolution', *Nature Photonics* **3**, 144–147 (2009).
- <sup>34</sup>B. Harke, J. Keller, C. K. Ullal, V. Westphal, A. Schönle and S. W. Hell, 'Resolution scaling in STED microscopy', *Optics express* **16**, 4154 (2008).
- <sup>35</sup>K. I. Willig, R. R. Kellner, R. Medda, B. Hein, S. Jakobs and S. W. Hell, 'Nanoscale resolution in GFP-based microscopy', *Nature Methods* **3**, 721–723 (2006).
- <sup>36</sup>B. Hein, K. I. Willig and S. W. Hell, 'Stimulated emission depletion (STED) nanoscopy of a fluorescent protein-labeled organelle inside a living cell', *Proceedings of the National Academy of Sciences of the United States of America* **105**, 14271 (2008).
- <sup>37</sup>Y. Sako, S. Minoghchi and T. Yanagida, 'Single-molecule imaging of EGFR signalling on the surface of living cells', *Nature Cell Biology* **2**, 168 (2000).
- <sup>38</sup>D. Axelrod, 'Cell-substrate contacts illuminated by total internal reflection fluorescence', *The Journal of cell biology* **89**, 141 (1981).
- <sup>39</sup>Y. Fu, P. W. Winter, R. Rojas, V. Wang, M. McAuliffe and G. H. Patterson, 'Axial superresolution via multiangle TIRF microscopy with sequential imaging and photobleaching', *Proceedings of the National Academy of Sciences* **113**, 4368–4373 (2016).

- <sup>40</sup>A. E. X. Brown, A. Hategan, D. Safer, Y. E. Goldman and D. E. Discher, 'Cross-correlated TIRF/AFM reveals asymmetric distribution of force-generating heads along self-assembled, "synthetic" myosin filaments', *Biophysical Journal* **96**, 1952–1960 (2009).
- <sup>41</sup>K. Kwakwa, A. Savell, T. Davies, I. Munro, S. Parrinello, M. A. Purbhoo, C. Dunsby, M. A. A. Neil and P. M. W. French, 'easySTORM: a robust, lower-cost approach to localisation and TIRF microscopy', *Journal of Biophotonics* **9**, 948–957 (2016).
- <sup>42</sup>J. Azoulay, A. Débarre, A. Richard and P. Tchério, 'Quenching and enhancement of single-molecule fluorescence under metallic and dielectric tips', *Europhysics Letters (EPL)* **51**, 374–380 (2007).
- <sup>43</sup>H. F. Hamann, A. Gallagher and D. J. Nesbitt, 'Near-field fluorescence imaging by localized field enhancement near a sharp probe tip', *Applied Physics Letters* **76**, 1953–1955 (2000).
- <sup>44</sup>S. Kühn, U. Håkanson, L. Rogobete and V. Sandoghdar, 'Enhancement of single-molecule fluorescence using a gold nanoparticle as an optical nanoantenna', *Physical Review Letters* **97**, 1–4 (2006).
- <sup>45</sup>T. J. Yang, G. Lessard and S. R. Quake, 'An apertureless near-field microscope for fluorescence imaging', *Appl. Phys. Lett.* **76**, 378–380 (2000).
- <sup>46</sup>W. Trabesinger, A. Kramer, M. Kreiter, B. Hecht and U. P. Wild, 'Single-molecule near-field optical energy transfer microscopy', *Applied Physics Letters* **81**, 2118–2120 (2002).
- <sup>47</sup>V. V. Protasenko, M. Kuno, A. Gallagher and D. J. Nesbitt, 'Fluorescence of single ZnS overcoated CdSe quantum dots studied by apertureless near-field scanning optical microscopy', *Optics Communications* **210**, 11–23 (2002).
- <sup>48</sup>L. Novotny, R. Bian and X. Xie, 'Theory of Nanometric Optical Tweezers', *Physical Review Letters* **79**, 645–648 (1997).
- <sup>49</sup>V. V. Protasenko, A. Gallagher and D. J. Nesbitt, 'Factors that influence confocal apertureless near-field scanning optical microscopy', *Optics Communications* **233**, 45–56 (2004).
- <sup>50</sup>N. Hayazawa, K. Furusawa, A. Taguchi, S. Kawata and H. Abe, 'Tip-enhanced two-photon excited fluorescence microscopy with a silicon tip', *Applied Physics Letters* **94**, 2–4 (2009).
- <sup>51</sup>L. Novotny, 'Single molecule fluorescence in inhomogeneous environments', *Applied Physics Letters* **69**, 3806–3808 (1996).
- <sup>52</sup>W. L. Barnes, 'Fluorescence near interfaces: the role of photonic mode density', *Journal of Modern Optics* **45**, 661–699 (1998).

- <sup>53</sup>D. M. Hercules, 'Fluorescence and phosphorescence analysis: principles and applications', *Fluorescence and Phosphorescence Analysis: Principles and Applications*/Ed. David M. Hercules. New York, NY: Interscience Publishers, c1966. (1966).
- <sup>54</sup>R. R. Chance, A. Prock and R. Silbey, 'Molecular fluorescence and energy transfer near interfaces', *Adv. Chem. Phys.* **37**, 65 (1978).
- <sup>55</sup>R. X. Bian, R. C. Dunn, S. Xie and P. T. Leung, 'Single molecule emission characteristics in near-field microscopy', *Physical Review Letters* **75**, 4772–4775 (1995).
- <sup>56</sup>W. P. Ambrose, P. M. Goodwin, J. C. Martin and R. A. Keller, 'Alterations of single molecule fluorescence lifetimes in near-field optical microscopy.', *Science (New York)* **265**, 364–7 (1994).
- <sup>57</sup>C. Girard, O. J. F. Martin and A. Dereux, 'Molecular life time changes induced by nanometer scale optical fields', *Physical Review Letters* **75** (1995).
- <sup>58</sup>M. Thomas, J. J. Greffet, R. Carminati and J. R. Arias-Gonzalez, 'Single-molecule spontaneous emission close to absorbing nanostructures', *Applied Physics Letters* **85**, 3863–3865 (2004).
- <sup>59</sup>J. N. Farahani, D. W. Pohl, H. J. Eisler and B. Hecht, 'Single quantum dot coupled to a scanning optical antenna: A tunable superemitter', *Physical Review Letters* **95** (2005) 10.1103/PhysRevLett.95.017402.
- <sup>60</sup>N. Anderson, A. Bouhelier and L. Novotny, 'Near-field photonics: tip-enhanced microscopy and spectroscopy on the nanoscale', *Journal of Optics A: Pure and Applied Optics* **8**, S227–S233 (2006).
- <sup>61</sup>N. J. D. Mol, M. J. E. Fischer and J. M. Walker, *Surface Plasmon Resonance Methods and Protocols* (Humana Press, 2010).
- <sup>62</sup>M. Fox, *Optical properties of solids* (Oxford, Oxford, 2010).
- <sup>63</sup>A. Eguiluz and J. J. Quinn, 'Hydrodynamic model for surface plasmons in metals and degenerate semiconductors', *Physical Review B* **14**, 1347–1361 (1976).
- <sup>64</sup>L. Novotny, E. J. Sánchez and X. Sunney Xie, 'Near-field optical imaging using metal tips illuminated by higher-order Hermite–Gaussian beams', *Ultramicroscopy* **71**, 21–29 (1998).
- <sup>65</sup>O. J. F. Martin and C. Girard, 'Controlling and tuning strong optical field gradients at a local probe microscope tip apex', *Appl. Phys. Lett.* **70**, 705–707 (1997).

- <sup>66</sup>L. Aigouy, A. Lahrech, S. Grāsillon, H. Cory, A. C. Boccara and J. C. Rivoal, 'Polarization effects in apertureless scanning near-field optical microscopy: an experimental study', *Optics Letters* **24**, 187–189 (1999).
- <sup>67</sup>R. Reisfeld and V. Levchenko, 'The influence of surface plasmons on fluorescence of the dye Lumogen F red 300 in condensed phase', *Optical Materials* **63**, 88–94 (2017).
- <sup>68</sup>P. Anger, P. Bharadwaj and L. Novotny, 'Enhancement and quenching of single-molecule fluorescence', *Physical Review Letters* **96**, 3–6 (2006).
- <sup>69</sup>B. Palash, A. Pascal and N. Lukas, 'Nanoplasmonic enhancement of single-molecule fluorescence', *Nanotechnology* **18**, 44017 (2007).
- <sup>70</sup>N. S. Abadeer, M. R. Brennan, W. L. Wilson and C. J. Murphy, 'Distance and plasmon wavelength dependent fluorescence of molecules bound to silica-coated gold nanorods', *ACS Nano* **8**, 8392–8406 (2014).
- <sup>71</sup>O. Kulakovich, N. Strelak, A. Yaroshevich, S. Maskevich, S. Gaponenko, I. Nabiev, U. Woggon and M. Artemyev, 'Enhanced Luminescence of CdSe Quantum Dots on Gold Colloids', *Nano Letters* **2**, 1449–1452 (2002).
- <sup>72</sup>G. W. Ford and A. Arbor, 'Electromagnetic Interactions of Molecules With Metal Surfaces With Metal Surfaces', *Physics Reports* **113**, 195–287 (1984).
- <sup>73</sup>S. A. Maier, *Plasmonics: fundamentals and applications* (Springer Science & Business Media, 2007).
- <sup>74</sup>J. Azoulay, A. Débarre, A. Richard and P. Tchénio, 'Field enhancement and apertureless near-field optical spectroscopy of single molecules', *Journal of Microscopy* **194**, 486–490 (1999).
- <sup>75</sup>A. Bouhelier, M. Beversluis, A. Hartschuh and L. Novotny, 'Near-Field Second-Harmonic Generation Induced by Local Field Enhancement', *Physical Review Letters* **90**, 8–11 (2003).
- <sup>76</sup>A. L. Demming, F. Festy and D. Richards, 'Plasmon resonances on metal tips: Understanding tip-enhanced Raman scattering', *Journal of Chemical Physics* **122**, 1–7 (2005).
- <sup>77</sup>N. I Cade, T. Ritman-Meer, K. A Kwaka and D. Richards, 'The plasmonic engineering of metal nanoparticles for enhanced fluorescence and Raman scattering.', *Nanotechnology* **20**, 285201 (2009).

- <sup>78</sup>A. Hartschuh, M. Beversluis, A. Bouhelier and L. Novotny, 'Tip-enhanced optical spectroscopy', *Philosophical Transactions of the Royal Society A* **362**, 807–819 (2004).
- <sup>79</sup>E. H. Synge, 'III. A microscopic method', *The London, Edinburgh, and Dublin Philosophical Magazine and Journal of Science* **11**, 65–80 (1931).
- <sup>80</sup>L. Novotny, *Principles of nano-optics*, edited by B. Hecht (Cambridge : Cambridge University Press, 2006, Cambridge, 2006).
- <sup>81</sup>T. Plakhotnik, E. A. Donley and U. P. Wild, 'Single-Molecule Spectroscopy and Dynamics at Room Temperature', *Annual Review of Physical Chemistry* **48**, 181–212 (1997).
- <sup>82</sup>A. Lewis, M. Isaacson, A. Harootunian and A. Muray, 'Development of a 500 Å spatial resolution light microscope. I. light is efficiently transmitted through  $\lambda/16$  diameter apertures', *Ultramicroscopy* **13**, 227–231 (1984).
- <sup>83</sup>D. W. Pohl, W. Denk and M. Lanz, 'Optical stethoscopy: Image recording with resolution  $\lambda/20$ ', *Applied Physics Letters* **44**, 651–653 (1984).
- <sup>84</sup>T. Enderle, T. Ha, D. F. Ogletree, D. S. Chemla, C. Magowan and S. Weiss, 'Membrane specific mapping and colocalization of malarial and host skeletal proteins in the *Plasmodium falciparum* infected erythrocyte by dual-color near-field scanning optical microscopy', *Proceedings of the National Academy of Sciences* **94**, 520–525 (1997).
- <sup>85</sup>H. Heinzelmann, T. Lacoste, T. Huser, H. J. Güntherodt, B. Hecht and D. W. Pohl, 'Instrumental developments and recent experiments in near-field optical microscopy', *Thin Solid Films* **273**, 149–153 (1996).
- <sup>86</sup>M. F. Garcia-Parajo, J. A. Veerman, A. G. T. Ruiter and N. F. Van Hulst, 'Near-field optical and shear-force microscopy of single fluorophores and DNA molecules', *Ultramicroscopy* **71**, 311–319 (1998).
- <sup>87</sup>E. Betzig, J. K. Trautman, T. D. Harris, J. S. Weiner and R. L. Kostelak, 'Breaking the Diffraction Barrier: Optical Microscopy of a Nanometric Scale', *Science* **251**, 1468–1470 (1991).
- <sup>88</sup>E. Betzig and R. Chichester, 'Single molecules observed by near-field scanning optical microscopy', *Science* **262**, 1422–1425 (1993).
- <sup>89</sup>J. M. Gerton, L. A. Wade, G. A. Lessard, Z. Ma and S. R. Quake, 'Tip-enhanced fluorescence microscopy at 10 nanometer resolution', *Physical Review Letters* **93**, 5–8 (2004).

## BACKGROUND

- <sup>90</sup>E. Sánchez, L. Novotny and X. Xie, 'Near-Field Fluorescence Microscopy Based on Two-Photon Excitation with Metal Tips', *Physical Review Letters* **82**, 4014–4017 (1999).
- <sup>91</sup>B. I. Yakobson, A. Larosa, H. D. Hallen and M. A. Paesler, 'Thermal/optical effects in NSOM probes', *Ultramicroscopy* **61**, 179–185 (1995).
- <sup>92</sup>F. Zenhausern, Y. Martin and H. K. Wickramasinghe, 'Scanning interferometric apertureless microscopy: optical imaging at 10 angstrom resolution.', *Science (New York, N.Y.)* **269**, 1083–5 (1995).
- <sup>93</sup>R. Hillenbrand and F. Keilmann, 'Material-specific mapping of metal/semiconductor/dielectric nanosystems at 10 nm resolution by backscattering near-field optical microscopy', *Applied Physics Letters* **80**, 25–27 (2002).
- <sup>94</sup>A. Hartschuh, E. J. Sánchez, X. S. Xie and L. Novotny, 'High-Resolution Near-Field Raman Microscopy of Single-Walled Carbon Nanotubes', *Physical Review Letters* **90**, 095503 (2003).
- <sup>95</sup>N. Hayazawa, Y. Saito and S. Kawata, 'Detection and characterization of longitudinal field for tip-enhanced Raman spectroscopy', *Applied Physics Letters* **85**, 6239–6241 (2004).
- <sup>96</sup>J. S. Lloyd, A. Williams, R. H. Rickman, A. McCowen and P. R. Dunstan, 'Reproducible electrochemical etching of silver probes with a radius of curvature of 20 nm for tip-enhanced Raman applications', *Applied Physics Letters* **99**, 1–4 (2011).
- <sup>97</sup>W. Denk, J. H. Strickler and W. W. Webb, 'Two-photon laser scanning fluorescence microscopy.', *Science (New York, N.Y.)* **248**, 73–6 (1990).
- <sup>98</sup>Z. Ma, J. M. Gerton, L. A. Wade and S. R. Quake, 'Fluorescence near-field microscopy of DNA at Sub-10A nm resolution', *Physical Review Letters* **97**, 1–4 (2006).
- <sup>99</sup>H. G. Frey, F. Keilmann, A. Kriele and R. Guckenberger, 'Enhancing the resolution of scanning near-field optical microscopy by a metal tip grown on an aperture probe', *Applied Physics Letters* **81**, 5030–5032 (2002).
- <sup>100</sup>H. G. Frey, S. Witt, K. Felderer and R. Guckenberger, 'High-resolution imaging of single fluorescent molecules with the optical near-field of a metal tip', *Physical Review Letters* **93**, 1–4 (2004).
- <sup>101</sup>P. J. Schuck, D. P. Fromm, A. Sundaramurthy, G. S. Kino and W. E. Moerner, 'Improving the mismatch between light and nanoscale objects with gold bowtie nanoantennas', *Physical Review Letters* **94**, 14–17 (2005).

- <sup>102</sup>C. Mu, B. D. Mangum, C. Xie and J. M. Gerton, 'Nanoscale Fluorescence Microscopy Using Carbon Nanotubes', *IEEE Journal of Selected Topics in Quantum Electronics* **14**, 206–216 (2008).
- <sup>103</sup>E. Shafran, B. D. Mangum and J. M. Gerton, 'Energy transfer from an individual quantum dot to a carbon nanotube', *Nano Letters* **10**, 4049–4054 (2010).
- <sup>104</sup>C. Höppener and L. Novotny, 'Antenna-based optical imaging of single Ca<sup>2+</sup> transmembrane proteins in liquids.', *Nano Letters* **8**, 642–646 (2008).
- <sup>105</sup>T. Härtling, P. Reichenbach and L. M. Eng, 'Near-field coupling of a single fluorescent molecule and a spherical gold nanoparticle', *Optics Express* **15**, 12806–12817 (2007).
- <sup>106</sup>R. Reisfeld, M. Grinberg, V. Levchenko, B. Kukliński, S. Mahlik, S. Magdassi and M. Grouchko, 'Sol-gel glasses with enhanced luminescence of laser dye Rhodamine B due to plasmonic coupling by copper nanoparticles', *Optical Materials* (2013) **10**. 1016/j.optmat.2013.11.011.
- <sup>107</sup>R. Reisfeld, V. Levchenko, F. Piccinelli and M. Bettinelli, 'Amplification of light emission of chiral pyridine Eu(III) complex by copper nanoparticles', *Journal of Luminescence* **170**, 820–824 (2016).
- <sup>108</sup>R. Reisfeld, V. Levchenko, A. Lazarowska, S. Mahlik and M. Grinberg, 'Intensification of luminescence of Europium-EDTA complex in polyvinyl pyrrolidone films by copper nanoparticles', *Optical Materials* **59**, 3–7 (2016).
- <sup>109</sup>R. Reisfeld, T. Saraidarov, G. Panzer, V. Levchenko and M. Gaft, 'New optical material europium EDTA complex in polyvinyl pyrrolidone films with fluorescence enhanced by silver plasmons', *Optical Materials* **34**, 351–354 (2011).
- <sup>110</sup>R. Reisfeld, M. Pietraszkiewicz, T. Saraidarov and V. Levchenko, 'Luminescence intensification of lanthanide complexes by silver nanoparticles incorporated in sol-gel matrix', *Journal of Rare Earths* **27**, 544–549 (2009).
- <sup>111</sup>V. Levchenko, M. Grouchko, S. Magdassi, T. Saraidarov and R. Reisfeld, 'Enhancement of luminescence of Rhodamine B by gold nanoparticles in thin films on glass for active optical materials applications', *Optical Materials* **34**, 360–364 (2011).



---

## METHODS AND MATERIALS

---

The method of tip-enhanced fluorescence microscopy adopted in this thesis can be loosely thought of as an amalgamation between atomic force microscopy (AFM) and fluorescence microscopy, whereby the tip of a scanning probe forms the enhancement tool. The methods of both AFM and fluorescence microscopy will therefore be discussed in detail in the sections to follow. The technique in this thesis also utilises a single photon counting module (SPCM) to count the number of photons from the sample, and the measurements are recorded using a field programmable gate array (FPGA). The workings of these two components are important for justifying why they were chosen and also for later explaining how the enhancement effect can be detected, so they will also be discussed at this stage.

### 3.1 ATOMIC FORCE MICROSCOPY

Atomic force microscopy (AFM) is a scanning probe technique whereby a small probe (usually made from silicon, or metal-coated silicon) is scanned over the surface of a sample. A schematic of basic AFM components can be seen in Figure 3.1.

An AFM itself consists of a probe holder, onto which a changeable probe (a tip attached to a cantilever) can be mounted. As the tip scans over the surface, the cantilever that it is attached to deflects upwards or downwards as it reaches objects of different heights within the sample. Measuring this deflection allows a topographic image of the sample to be created. Cantilevers/tips of different sizes, materials and stiffness can be chosen depending upon the imaging application. To detect the movement of the cantilever, an infrared (IR) laser beam is reflected off the top-side of the cantilever. Following reflection, the IR laser beam is incident on a photodetector also contained within the AFM. For the work performed in this thesis, a *sample-scanning* AFM is used. With this AFM, a three-dimensional motorised sample stage is used to scan the sample position relative to the stationary AFM probe (as in Fig-

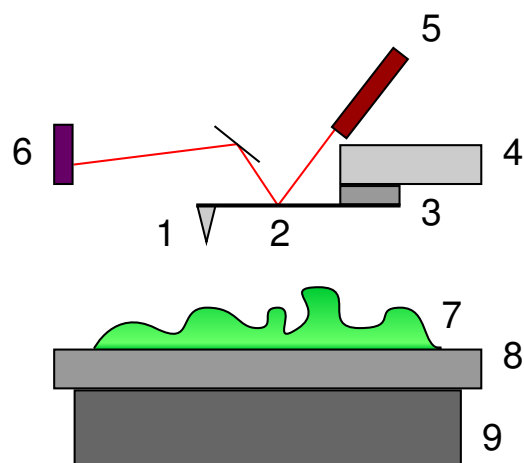


Figure 3.1.: Schematic of basic AFM components. The AFM-tip (1) attached to a cantilever (2) is inserted into a probe holder (4). The probe can be made to oscillate at resonance by a piezoelectric element (3). An infrared diode laser (5) is reflected off the top-side of the cantilever and is incident on a photodetector (6). A sample (7) is mounted onto the sample stage (8), whose position is controlled by piezomotors (9), allowing the sample/stage to move in the x, y and z direction relative to the probe.

ure 3.1). However, many AFMs have this three-dimensional driver at the probe, scanning the probe position relative to a stationary sample; these are known as probe-scanning AFMs [112].

Most AFMs (including the one used in this thesis) utilise a beam-deflection measurement, developed in 1988 [113], in order to determine the deflection of the cantilever. The photodetector of the AFM is made up of four closely-spaced quadrant photodiodes. As the cantilever deflects, the reflected laser beam will undergo an angular displacement at the cantilever, causing a displacement in beam position at the photodetector, which will cause one of the photodiodes to collect more light than the other three. By analysing the relative detection intensity for each of the four quadrants, the exact position that the IR laser falls onto the photodetector can be determined. The voltage output by the photodetector can either be used to directly obtain the height of the sample feature, or more commonly used to feedback into the tip z-position to maintain a fixed separation between the tip and the sample. Alternative deflection-measurement techniques have been previously used, including methods based upon creating a capacitor with a metallic cantilever and an additional metal contact [114], inter-

ferometry between light reflected from the cantilever and a reference signal [115], and using a cantilever made of a quartz tuning fork to directly output a voltage dependent upon deflection [116].

An AFM can be operated in several different modes. A common operation mode is contact mode, in which the AFM probe is in constant contact with the sample surface. The sample is scanned in the  $x$ - and  $y$ -directions underneath the probe, and the cantilever bends in response to the varying height of sample features. For contact mode, the AFM is operated at very short tip-sample separations, where interatomic forces will affect cantilever deflection. However, by increasing the tip-sample separation to the 10 nm to 100 nm range [117], the AFM can alternatively be operated in one of the non-contact modes. For these modes, the tip is made to oscillate using a piezoelectric element in the probe holder, allowing the tip to approach and retract from the sample at high frequencies.

For conventional tapping mode AFM, the probe is driven at its resonance frequency which is typically in the range of 100 kHz to 300 kHz. As the probe comes close to the surface, the longer-range interaction forces between the probe and the sample (such as van der Waals forces, capillary forces, and adhesive forces [112]) cause the oscillation frequency to change. The AFM acts to maintain a particular oscillation amplitude by changing the offset in the  $z$ -position of the probe relative to the sample: this change in offset will be indicative of the height of the sample feature. Tapping mode is useful for delicate samples which would otherwise be damaged by the high lateral forces occurring from the scanning motion in contact mode microscopy, and is also a more favourable mode for imaging in liquids[118]. Along with this, the phase of the cantilever oscillation with respect to the drive signal can be monitored to provide additional information about the mechanical properties of the sample [119].

A second non-contact mode (and the mode primarily used in this thesis) is PeakForce quantitative nanomechanical mapping (QNM). For this, the probe is oscillated at a frequency much lower than its resonance ( $\approx 1$  kHz) and the deflection of the cantilever during each cycle is analysed. Knowing the spring constant of the cantilever allows the force experienced by the cantilever to be calculated using Hooke's law: this force as a function of tip-sample separation can be depicted as a force-curve, an example of which can be seen in Figure 3.2. As the probe is moved towards or away from the sample surface, the attractive force which exists between the two causes deflection of the cantilever: by measuring the deflection of the cantilever at the point of probe release (point D on Figure 3.2), the adhesion between the probe

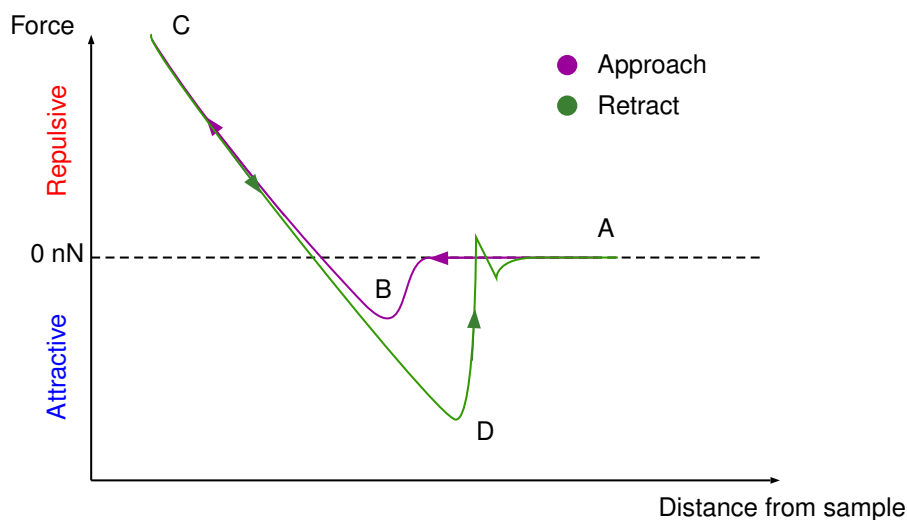


Figure 3.2.: Force experienced by the probe as a function of distance from a typical sample during probe approach (purple) and probe retraction (green). At point A, the tip is far from the sample surface and experiences approximately zero force. As the probe moves towards the sample, attractive forces from the surface cause the tip to "snap-in" (B) and as the tip moves closer to the surface, the force becomes repulsive. At C, the tip starts to be retracted. Once the probe is sufficiently far away, the tip experiences an attractive force as it is pulled away from the surface until D, where the force applied to the cantilever is greater than the tip-sample adhesion and the tip snaps away. A restoring force may occur as the probe is released.

and the sample can be determined [112]. During each cycle, the maximum force is carefully controlled to limit damage to both the sample and the probe [120]. Other properties which can be obtained directly from a typical force-curve include dissipation energy and sample deformation [121]. Using adhesion and deformation measurements, a Derjaguin-Muller-Toporov (DMT) model [122] can be fitted to the data in real time to also obtain the reduced Young's Modulus of the sample (known as the DMT modulus in PeakForce QNM operation). A variety of mechanical properties and force measurements can therefore be obtained in real-time, alongside conventional topographic information, when using this mode of operation.

For the work performed in this thesis, the AFM used was a Bruker BioScope Catalyst. The AFM-tip's z-position is measured via an ana-

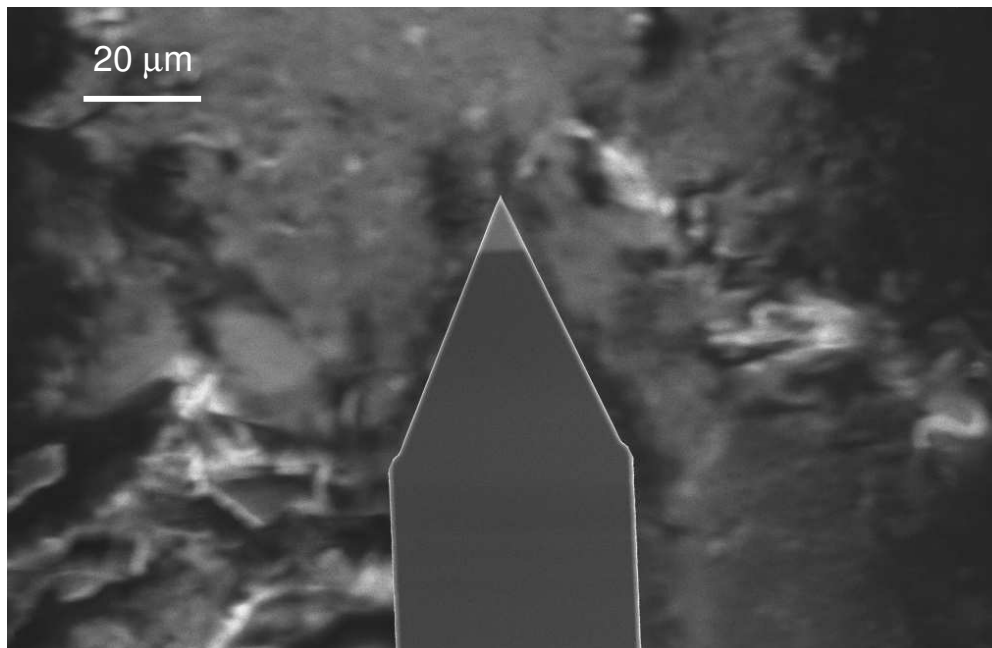
logue output from a SAM-V (signal access module - version 5) box. The AFM probes used in this investigation are Bruker OLTESPA tips, which have a visible tip apex due to their location at the end of the cantilever (see Figure 3.3). Using these probes allowed better estimation of tip location along the cantilever compared to other probes.

### 3.2 FLUORESCENCE MICROSCOPY

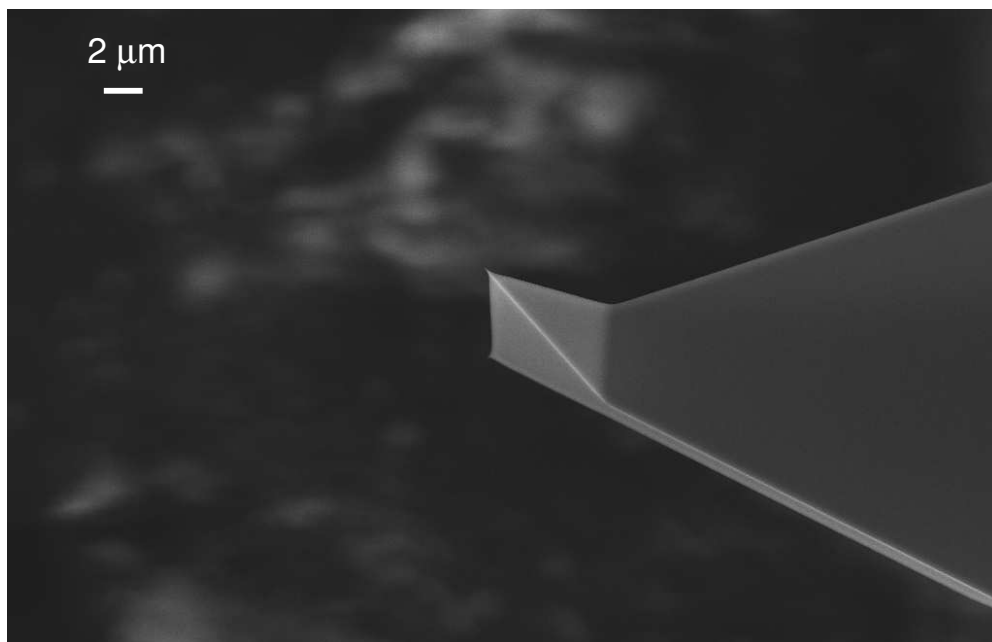
Fluorescence is the emission of photons by atoms or molecules whose electrons have been stimulated to a higher excitation state via illumination from an external source. Different types of fluorescent molecules emit light of different wavelengths. Therefore, by attaching different types of fluorescent molecules to particular structures in a sample (for example, a cell nucleus or a cell membrane), the locations of the different components of the sample can be determined - this microscopic technique therefore also serves as a method of obtaining spectroscopic information about a sample.

The fluorescence process itself requires the external illumination source to be of a specific wavelength. When a fluorescent molecule absorbs a photon with an energy equal to the difference between its energy states, an electron is promoted to a higher energy state. The energy states of the molecule, along with the possible energy changes that an electron can undergo, can be depicted as a *Jablonski diagram* (see Figure 3.4). After a particular period of time (nanoseconds), the electron relaxes back to the ground state, emitting a photon, shown in red in Figure 3.4. During the finite period of time that the electron occupies the excited state, it will be dissipating its energy non-radiatively in the form of vibrational energy (heat). As some of the energy is dissipated non-radiatively, the emitted photon will have a lower energy than the absorbed photon. Fluorescent molecules therefore characteristically emit light at a longer wavelength than that at which they are excited. Sometimes the electron can relax to the ground state entirely through non-radiative processes without emitting a photon (all purple transitions in Figure 3.4).

When the molecule is excited above the ground state, there is also a small probability that an electron can transition to an excited triplet state from an excited singlet state. Molecules which are in their triplet state can undergo complex chemical reactions with other molecules; any reaction with molecular oxygen causes permanent damage to the fluorescent molecule in a process known as *photobleaching*. In this particular reaction, a free radical (singlet oxygen molecule) is also produced which can chemically modify other molecules in the cell



(a)



(b)

Figure 3.3.: Scanning electron microscope images of Bruker OLTESPA AFM-tips. (a) Cantilever from directly underneath. (b) Under-side view of probe. Tip protrudes from the end of the cantilever, allowing an estimation of tip location.

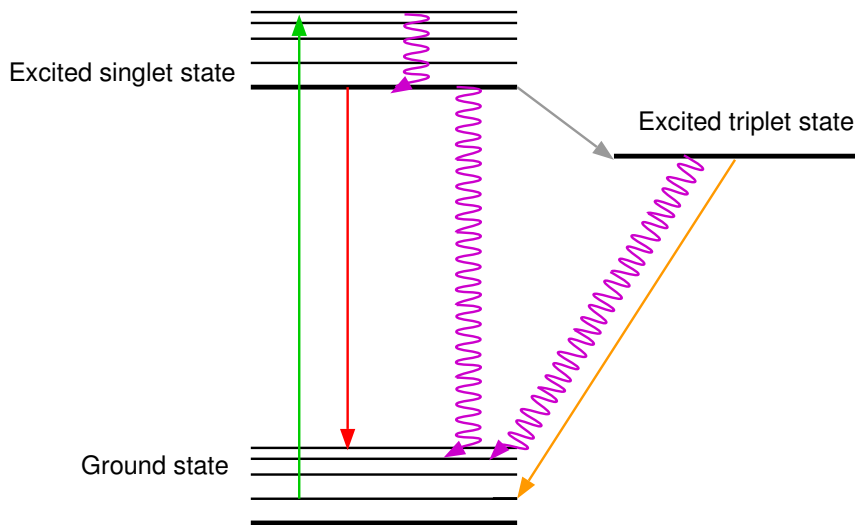


Figure 3.4.: Jablonski diagram for a typical fluorescent molecule. Upon absorption of a photon of the correct wavelength, an electron can be promoted to an excited state from the ground state (green). Most commonly, an electron in the excited singlet state will dissipate its energy radiatively as fluorescence emission (red). However, non-radiative dissipation of energy can also occur and the electron relaxes to the ground state without emission of a photon (purple). An electron may alternatively be excited to a triplet state, again where non-radiative or radiative emission (called phosphorescence) can also occur.

sample [123]. From the triplet state, electrons can also relax to the ground state either radiatively or non-radiatively. If the electron decays radiatively the emission process is known as phosphorescence: this can be distinguished from fluorescence because the triplet state transition is less likely, resulting in a long excited state lifetime. The lifetime of the excited singlet state is typically around nanoseconds, whereas the lifetime of the excited triplet state could be on the order of minutes [123].

In order for a sample to be imaged using fluorescence microscopy, it needs to be fluorescently labelled. In some cases, the structure of interest may be autofluorescent, containing a protein which naturally fluoresces: one such example of this is chlorophyll in plants. However in general, the structure is either non-fluorescent or its autofluorescence is not sufficiently bright for use in experiments, and needs to be labelled with an extrinsic protein [124]. One method is to use fluorescent stains or dyes - usually small molecules which bind to other biological molecules of interest. Examples of this include DAPI which binds to DNA [125] or fluorescent derivatives of phalloidin which attach to actin fibres [126]. Alternatively, fluorescent molecules can be bound to antibodies which will attach to specific antigens in biological samples, in a technique known as immunofluorescence. Fluorescein-labelled and rhodamine-labelled immunoglobulins are widely used as extrinsic labels for this purpose [124]. Being able to label different structures of interest with fluorescent molecules emitting different wavelengths allows an entire image of a sample to be obtained, or different processes to be tracked over time. This specificity is what makes fluorescence microscopy particularly advantageous for imaging biological samples.

### 3.3 SINGLE PHOTON COUNTING MODULE

A single photon counting module (SPCM) is a device used to detect single photons of light. A SPCM uses a single photon avalanche diode (SPAD) to generate an electrical pulse for each photon detected.

A SPAD is a semiconductor device based upon a reverse-biased p-n junction [127], a schematic of which is shown in Figure 3.5. A p-n junction is made up of two layers of semiconductor material: one which has been doped to give an excess number of electrons (n-type material) and another which has been doped to give an excess number of holes (p-type material). When these two layers are brought together, there is diffusion of electrons and holes along concentration gradients to the opposing regions. In this process, part of the n-region closest

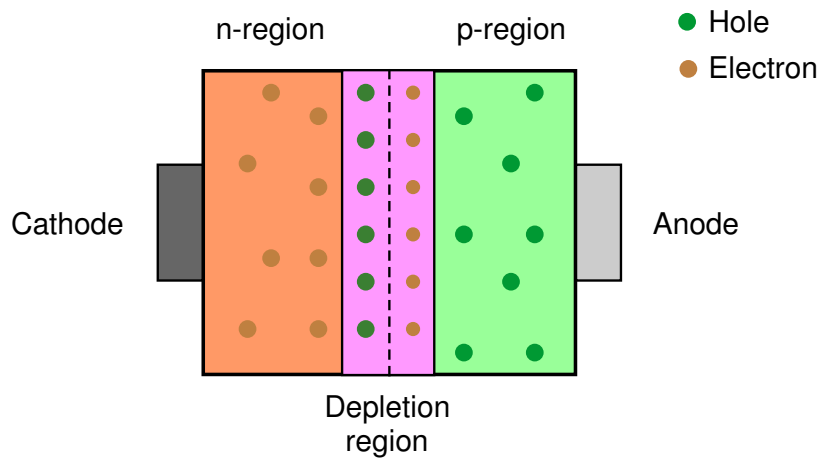


Figure 3.5.: Schematic of a p-n junction. Junction is made up of an n-type region, and a p-type region. Where they meet, a depletion region is formed due to migration of electrons and holes along concentration gradients.

to the p-region becomes positive, having lost electrons, whereas part of the p-region becomes negative having gained electrons from the n-region. This difference in charge establishes an electric field across the device. The region in the centre of the device at this point is called the depletion region.

When a photon is absorbed in the depletion region of the p-n junction, an electron-hole pair is generated; the separation of this electron-hole pair with the electric field manifests as current flowing through the device, indicating that a photon has been detected. To ensure that a detectable current is produced, the device is operated in the reverse-bias regime at a bias-voltage above the breakdown voltage. In terms of the p-n junction, this means that a higher potential is applied to the cathode relative to the anode, acting to increase the electric field already present in the device. The electric field across the p-n junction is high enough (greater than  $10^5 \text{ V cm}^{-1}$ ) [128] such that introducing a single charge carrier into the depletion layer can trigger an avalanche current. The avalanche occurs because an injected charge carrier will gain enough kinetic energy (due to being accelerated by the electric field) to promote an electron in the depletion layer from the valence band to the conduction band, creating a new electron-hole pair: this is called impact ionisation. These new charge carriers in the depletion

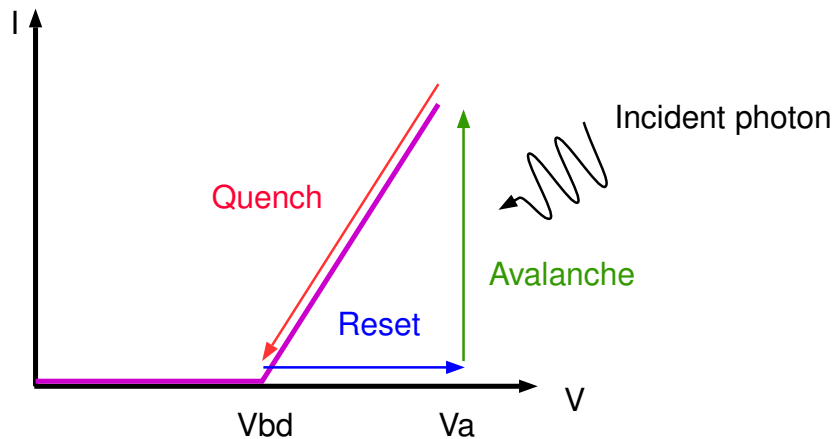


Figure 3.6.: Current-voltage graph near the operation voltage for a SPAD, indicating how the applied voltage and induced current change through different stages of operation. The operation voltage  $V_a$  is applied across the p-n junction: when a photon is incident on the depletion layer, an avalanche current occurs, acting to increase the current whilst maintaining the same potential across the device. To stop the avalanche current so that more photons can be detected, the voltage across the device needs to first be lowered from  $V_a$  down to the breakdown voltage  $V_{bd}$ , causing a corresponding reduction in current-flow through the device (quenching). When zero current is achieved, the potential across the device is then raised back up to  $V_a$  ready for the detection of another photon (resetting).

layer are again accelerated, creating a chain of ionisation processes to produce an amplified current. The process is instantaneous and produces a current with a magnitude on the order of milliamps, ensuring that single photons are always detected.

The leading edge of the avalanche pulse signifies the arrival time of the photon. This avalanche current will continue until the bias voltage is quenched; the bias-voltage is reduced back down to the breakdown voltage via a separate circuit within the single photon counting module, decreasing the electric field and stopping charge carriers being accelerated across the depletion layer. Before another photon can be detected, the bias voltage needs to be reset; this lowering and restoring of the bias-voltage takes a finite period of time known as the dead-time, in which no other photons can be detected. The changes in

the voltage and current through the diode during the detection (avalanche), quenching and resetting process is shown in Figure 3.6. For the SPCM in this thesis, the typical dead-time is 50 ns [129].

The SPCM used for the work performed in this thesis was a PerkinElmer<sup>®</sup> single photon counting module (version number: SPCM-AQRH-16-FC), able to detect photons with a wavelength from 400 nm to 1060 nm.

### 3.4 FIELD PROGRAMMABLE GATE ARRAY

A field programmable gate array (FPGA) is a device which allows reconfigurable computing. This means that the hardware can be re-programmed an unlimited number of times to suit a particular algorithm [130–132]: it is this customisation of the hardware which results in FPGAs being able to perform high-speed programming applications more efficiently than traditional microprocessors.

A simple example demonstrating the advantage of FPGA over a traditional microprocessor would be a calculation whereby thousands of integers are added together. Using a microprocessor, the computation is restricted to the number of integer arithmetic adders which were made available on the unit at manufacture. Other hardware functions will remain idle during operation. However, if an FPGA is programmed to perform this calculation, all logic gates could theoretically be reconfigured to be integer arithmetic adders such that all of the hardware resources will be busy, speeding up the calculation.

The basic architecture of an FPGA can be seen in Figure 3.7. An FPGA is essentially a semiconductor device comprised of a grid of configurable *logic blocks* which can be connected together via *programmable interconnect* [130, 132, 133]. Logic blocks consist of *look-up tables* which compute logic truth functions (for example, AND/OR), carry and control logic which implement fast arithmetic operations (for example, adders or multipliers), and memory elements. The programmable interconnect is a horizontal and vertical mesh of wire segments interconnected by programmable switches known as programmable interconnect points. The logic blocks can communicate with external hardware through *programmable I/O blocks*.

FPGA programming offers many advantages compared to processor-only approaches, particularly when it comes to very specific tasks which require high performance or reliability. Because different processing operations do not need to compete for the same resources, FPGA is truly parallel in nature. This means that many different tasks can be performed by an FPGA, all at different rates, making it a useful tool for data acquisition and real-time analysis.

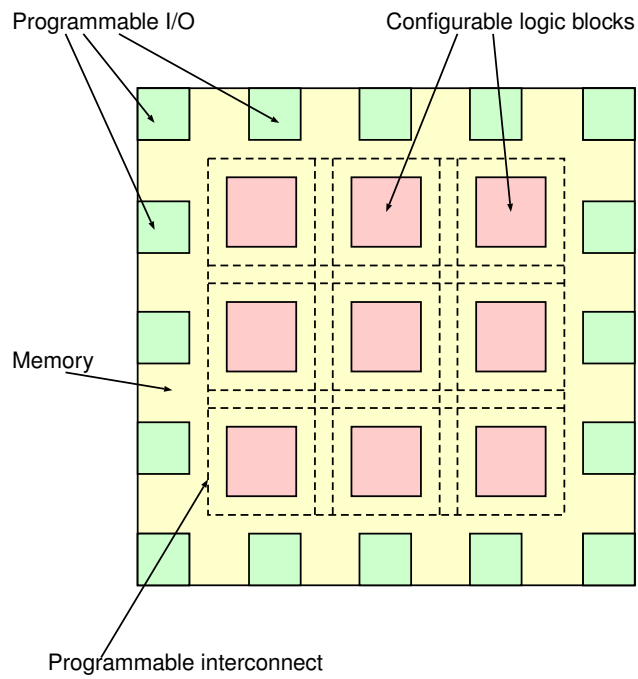


Figure 3.7.: Schematic of FPGA architecture. FPGA is based on a grid of logic blocks which can be configured to implement different functions. Logic blocks are linked to each other, and to programmable inputs and outputs, and memory blocks by programmable interconnect - a wire mesh with programmable switches distributed throughout.

The FPGA used for this project is a National Instruments<sup>TM</sup> LabVIEW flexRIO, and is a device consisting of a processor and an FPGA. An NI5761 is inserted into the flexRIO, which offers both analogue and digital input channels to the FPGA for data acquisition.

## REFERENCES

- <sup>112</sup>P. Eaton and P. West, *Atomic Force Microscopy*: (Oxford University Press, Mar. 2010).
- <sup>113</sup>G. Meyer and N. M. Amer, 'Novel optical approach to atomic force microscopy', *Applied Physics Letters* **53**, 1045–1047 (1988).
- <sup>114</sup>T. Göddenhenrich, 'Force microscope with capacitive displacement detection', *Journal of Vacuum Science & Technology A: Vacuum, Surfaces, and Films* **8**, 383 (1990).
- <sup>115</sup>D. Rugar, H. J. Mamin and P. Guethner, 'Improved fiber-optic interferometer for atomic force microscopy', *Applied Physics Letters* **55**, 2588–2590 (1989).
- <sup>116</sup>F. J. Giessibl, 'High-speed force sensor for force microscopy and profilometry utilizing a quartz tuning fork', *Applied Physics Letters* **73**, 3956–3958 (1998).
- <sup>117</sup>R. Wiesendanger, 'Scanning force microscopy (SFM)', in *Scanning probe microscopy and spectroscopy: methods and applications* (Cambridge University Press, Cambridge, 1994), pp. 210–264.
- <sup>118</sup>P. K. Hansma et al., 'Tapping mode atomic force microscopy in liquids', *Applied Physics Letters* **64**, 1738–1740 (1994).
- <sup>119</sup>J. P. Cleveland, B. Anczykowski, A. E. Schmid and V. B. Elings, 'Energy dissipation in tapping-mode atomic force microscopy', *Applied Physics Letters* **72**, 2613–2615 (1998).
- <sup>120</sup>G. Oncins and J. Díaz-Marcos, 'Atomic Force Microscopy : probing the Nanoworld', *Handbook of instrumental techniques from CCI TUB* (2012).
- <sup>121</sup>B. Pittenger, N. Erina and C. Su, 'Quantitative Mechanical Property Mapping at the Nanoscale with PeakForce QNM', *Burker Application Note* **128**, 1–12 (2009).
- <sup>122</sup>B. V. Derjaguin, V. M. Muller and Y. U. P. Toporov, 'Effect of contact deformation on the adhesion of particles.', *Journal of colloid and interface science* **52**, 105–108 (1975).
- <sup>123</sup>D. B. Murphy, *Fundamentals of light microscopy and electronic imaging* (New York : Wiley, 2001, New York, 2001).

- <sup>124</sup>J. R. Lakowicz, *Principles of Fluorescence Spectroscopy* (Springer US, 2007).
- <sup>125</sup>J. Kapuscinski, 'DAPI: a DNA-Specific Fluorescent Probe', *Biotechnic & Histochemistry* **70**, 220–233 (1995).
- <sup>126</sup>J. A. Cooper, 'Effects of cytochalasin and phalloidin on actin.', *The Journal of Cell Biology* **105**, 1473 LP –1478 (1987).
- <sup>127</sup>M. W. Fishburn, 'Fundamentals of CMOS single-photon avalanche diodes', Massachusetts Institute of Technology **Thesis** (2012).
- <sup>128</sup>F. Zappa, S. Tisa, A. Tosi and S. Cova, 'Principles and features of single-photon avalanche diode arrays', *Sensors and Actuators, A: Physical* **140**, 103–112 (2007).
- <sup>129</sup>Spcm-Aqr Series, 'Single Photon Counting Module', Biomedical Solutions Datasheet, [http://sites.fas.harvard.edu/phys191r/Bench\\_Notes](http://sites.fas.harvard.edu/phys191r/Bench_Notes) (2007).
- <sup>130</sup>M. Lanzagorta, *Introduction to reconfigurable supercomputing [electronic resource]*, edited by S. Bique and R. Rosenberg (San Rafael, Calif. 1537 Fourth Street, San Rafael, CA 94901 USA : Morgan & Claypool Publishers, c2009, San Rafael, Calif. (1537 Fourth Street, San Rafael, CA 94901 USA), 2010).
- <sup>131</sup>M. Gokhale, *Reconfigurable computing : accelerating computation with field-programmable gate arrays*, edited by P. S. Graham (New York : Springer-Verlag, 2005, New York, 2005).
- <sup>132</sup>S. Hauck and A. DeHon, *Reconfigurable Computing: The Theory and Practice of FPGA-Based Computation*, Systems on Silicon (Elsevier Science, 2010).
- <sup>133</sup>E. Tlelo-Cuautle, J. d. J. Rangel-Magdaleno and L. G. la Fraga, 'Introduction to Field-Programmable Gate Arrays', in *Engineering applications of fpgas: chaotic systems, artificial neural networks, random number generators, and secure communication systems* (Springer International Publishing, Cham, 2016), pp. 1–32.

# 4

---

## BUILDING A FLUORESCENCE MICROSCOPE

---

### 4.1 INTRODUCTION

The previous chapters have outlined the theoretical mechanisms behind the technique of tip-enhanced fluorescence microscopy. When light of a particular polarisation is incident on a sharp tip, the electric field at the apex of the tip is amplified, giving the ability to modify the optical properties of any fluorescing molecule which is in its vicinity. The effect of this is to achieve a highly localised area whereby fluorescence is either being reduced (known as fluorescence quenching), or enhanced as required in this case.

The approach taken to build the tip-enhanced fluorescence microscope in this thesis was to use the tip of a commercially-available atomic force microscope (AFM) as the sharp-tipped enhancement tool. Instead of using multiple light sources for separate fluorescence excitation of the sample and induction of the enhancement effect, it is beneficial to have both of these functions being performed by the same light source. This serves to limit the amount of background light falling on the sample, helping to retain a high signal-to-noise ratio.

The set-up (which will be discussed in further detail later in this chapter) consists of an AFM mounted atop an inverted optical microscope, which delivers a focussed excitation laser beam to the sample. This is used to both induce fluorescence, and also to initiate the enhancement effect when the AFM-tip is positioned in the pathway of this beam. The inverted optical microscope is also used to collect the light emitted from the sample which is detected with a single photon counting module (SPCM), allowing an image to be formed. Because of the sample-scanning nature of the AFM used in this investigation, a fluorescence image can be obtained by translating the sample through the incident excitation beam using the AFM stage. The addition of the AFM-tip into this set-up results in a tip-enhanced fluorescence microscope. Therefore, in order to realise a tip-enhanced fluorescence

microscope, the optical pathways allowing fluorescence images to be achieved first needed to be built, aligned and tested.

This chapter outlines the steps taken to build a fluorescence microscope, including the hardware which formed the microscope, along with the software systems which were developed to align the two light pathways. To test the performance of the microscope, various samples were used, including a fluorescent polymer and a fluorescently-labelled biological sample. Fluorescent beads of a known size were also imaged to test that the resolution of the microscope was diffraction-limited.

## 4.2 METHOD

This section first outlines the hardware which forms the fluorescence microscope, becoming the basis of the tip-enhanced fluorescence microscope should the AFM-tip also be aligned with the two light pathways. The experimental set-up will be discussed in Section 4.2.1. A procedure for aligning the excitation and collection light pathways, for which a LabVIEW program was developed, will be outlined in Section 4.2.3.

### 4.2.1 *Experimental Arrangement*

A schematic of the microscope can be seen in Figure 4.1. It should be noted that this same set-up also forms the basis of a tip-enhanced fluorescence microscope, but crucially only when the AFM-tip is aligned with the excitation beam. This set-up will therefore also be referred to in subsequent chapters of this thesis.

The fluorescence microscope is comprised of two main optical pathways; an excitation pathway, and a collection pathway. The excitation pathway (shown in green in Figure 4.1) delivers the excitation laser beam ( $\lambda = 532 \text{ nm}$ ) to the sample to induce fluorescence. This is done with use of a longpass dichroic mirror with a cut-off wavelength of  $561 \text{ nm}$ , allowing the excitation beam to be directed into an inverted optical microscope (Olympus IX71). For the results obtained in this chapter, an objective lens with 50x magnification and a numerical aperture (NA) of 0.5 (Olympus LMPLAN FL) was used to focus the excitation beam onto the sample in question. The sample is held in place on the stage of an AFM (Bruker BioScope Catalyst) which is mounted on top of the inverted optical microscope. Also in the excitation pathway are several components to condition and control the focussed excitation beam at the sample. A radial polarisation converter (AR-

Coptix) is used to ensure that the correct polarisation is achieved for maximum enhancement by the AFM-tip. The position of the incident spot at the sample is controlled by a 2D galvanometer (Thorlabs): this is operated via a LabVIEW program and is used for aligning the two light pathways, as will be described in Section 4.2.3.

The AFM used for the work performed in this thesis is a sample-scanning AFM; this means that, unlike the majority of AFMs, the tip remains stationary whilst the AFM stage moves the sample in the  $x$ - and  $y$ -directions underneath the tip to form an image. Therefore the excitation beam needs only to be focussed onto one area of the sample, and then the sample itself is moved through the focussed beam by the AFM ( $x,y$ ) stage, enabling different areas of the sample to be fluorescently excited and an image of the whole sample to be built up.

The fluorescence emission from the sample is collected by the same objective lens, and is transmitted along the same pathway as the excitation beam, through the inverted optical microscope. Any emission at a wavelength longer than 561 nm is transmitted by the dichroic mirror, sending the light along a different pathway from the incoming excitation beam. A 50/50 reflectance/transmittance beamsplitter<sup>1</sup> is used to direct 50 % of emission photons to a USB camera (Allied Vision technologies Guppy F-033) enabling the user to view the sample in real-time, and 50 % of emission photons to a SPCM (PerkinElmer) which is used to produce all fluorescent images seen in this thesis. Various filters are used within the collection pathway, including a 775 nm short-pass in order to filter out the infrared light inherent to the AFM. A second removable filter is also used, and can be switched to suit the emission of the particular sample; unless stated otherwise this was a 570 nm long-pass filter to suit the fluorescence samples used in this thesis. This filter also acts to remove any of the excitation laser light which has leaked through the dichroic mirror to maximise signal-to-noise ratio (SNR) and improve image quality. The emission is focussed onto the face of a single-mode optical fibre with a core diameter of approximately 4  $\mu\text{m}$  which is connected to the SPCM. It should be noted that, because the aperture of the optical fibre is essentially a confocal pin-hole, this set-up is effectively a confocal fluorescence microscope. For some of the work performed in this thesis, the single-mode optical fibre was exchanged for a multi-mode optical fibre with a 400  $\mu\text{m}$  core diameter, providing a larger collection area. The utility of the alternative fibre will be described in Chapters 5 and 6, and unless stated

---

<sup>1</sup> For future work, it might be preferable to use a 10/90 reflectance/transmittance beamsplitter in place of the 50/50 beamsplitter, ensuring that as much of the fluorescence signal as possible reaches the SPCM.

## BUILDING A FLUORESCENCE MICROSCOPE

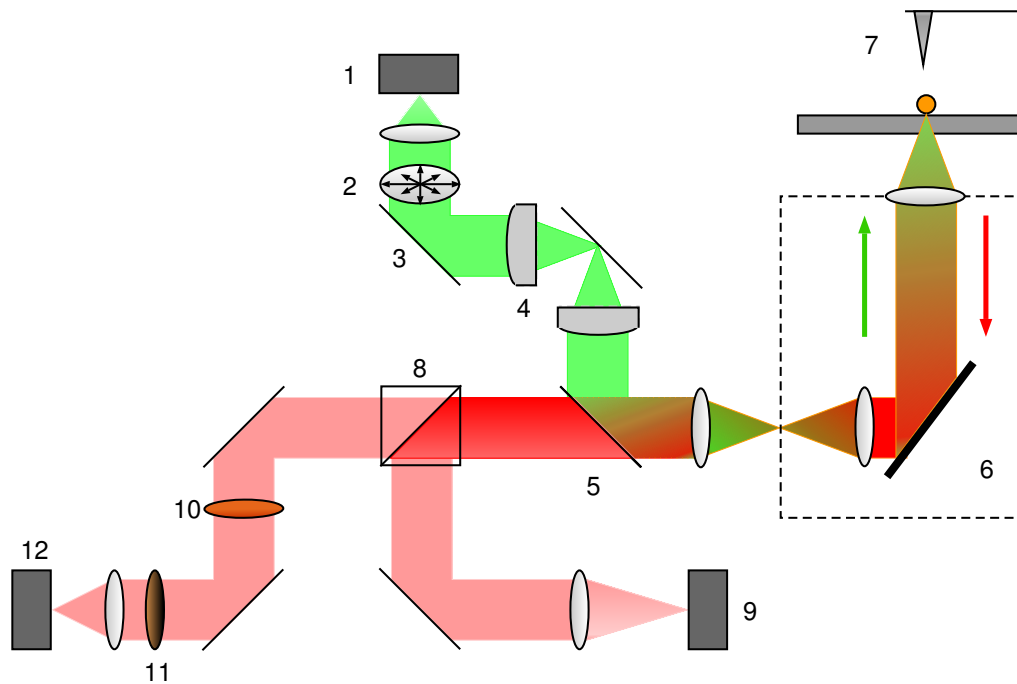


Figure 4.1.: Schematic showing optical set-up. (1) Excitation laser ( $\lambda = 532 \text{ nm}$ ) is delivered to the left-side port of an inverted optical microscope (6) via a 2D galvanometer mirror (3), 4f relay lens system (4), and a longpass dichroic mirror (5) with a cut-off wavelength of  $561 \text{ nm}$ . Polarisation of the excitation light is modified via a radial polarisation converter (2). A 50x air objective lens ( $\text{NA} = 0.5$ ) focusses excitation light onto a fluorescent sample, positioned on an AFM (x,y) stage (7) which has been mounted atop of the inverted optical microscope. The same objective collects fluorescence emission. The emission is transmitted by the dichroic mirror and is directed to a 50/50 beamsplitter (8). Half of the emission is focussed onto a USB camera (9), while the other half is focussed onto the aperture of an optical fiber leading to a SPCM (12). Two filters are present in the SPCM pathway: a  $775 \text{ nm}$  short-pass (11), and a removable filter (10) to suit the fluorescence emission.



Figure 4.2.: Customised sample holder. A magnetic strip provides additional structural support for the thin coverglass samples, whilst the aperture allows light throughput between the sample and the objective lens underneath. Two smaller magnets are used to hold the coverglass in place on the magnetic strip.

otherwise, it should be assumed that the single-mode optical fibre has been used for data collection.

#### 4.2.2 *A Customised Sample Holder*

For all of the samples used in this thesis, they need to be exposed, allowing the AFM-tip to come close enough to modify the fluorescence emission. For this reason, all samples are prepared onto glass coverslips which are subsequently not mounted onto microscope glass slides (as would usually be the case with a conventional light microscope). Not mounting the coverslip presents problems however. Coverslips are extremely thin pieces of glass, which are very easily cracked when the AFM-tip makes contact with the sample. A customised holder is needed to provide structural support to the thin glass, allowing it to be probed by the AFM.

To solve this problem, a magnetic strip is attached to the bottom of all of the samples developed for this thesis<sup>2</sup>. The magnetic strip has a large aperture in its centre, allowing light throughput between the sample and the objective lens. The strip is attached through use of two smaller magnets, placed on top of the coverslip. An image of the customised sample holder can be seen in Figure 4.2.

The presence of the two magnets however means that the sample clamp which was purchased with the AFM no longer fits into place over the sample. A sample clamp is usually required to ensure that the

<sup>2</sup> Apart from the FluoCell sample used later in this chapter

sample does not move around as imaging takes place. Potential effects of not having a sample clamp could include distortion of the image, because the sample will not be moved back to its original position in the x-direction during scanning. Alternatively, a widening of the point spread functions could also occur if the sample is moving during the entire scan and not just where the scan changes direction. This chapter will therefore also aim to determine whether or not the lack of a clamp has any serious detrimental effects to image formation.

#### 4.2.3 *Aligning the Optical Pathways*

Because the AFM is a sample-scanning AFM, the alignment process is simplified: the excitation and collection spots do not need to scan over the sample to create an image. Instead, their position can remain fixed whilst the sample is scanned. In order to maximise SNR, a collection fibre with a small core size ( $\approx 4\ \mu\text{m}$ ) is used, acting as a confocal pinhole to minimise stray light.

To align the excitation and collection spots, laser light with a wavelength longer than 561 nm is sent back through the system via the optical fiber of the SPCM, whilst the 532 nm excitation laser is delivered through the system in the usual way. An autofluorescent plastic slide (Chroma) is placed on the sample stage, allowing both beams to be focussed to diffraction-limited spots. The resulting fluorescence spot along with the collection spot are both visible through the USB camera. The mirrors in the collection pathway are adjusted until the two spots overlap in space. For finer adjustment, a second stage of alignment was developed. For this second component, the collection laser is removed and the optical fiber is reconnected to the SPCM. Using the galvanometer, the position of the excitation laser spot on the sample can be controlled. A LabVIEW field programmable gate array (FPGA) program was created to deliver a variable voltage to the galvanometer, snaking the focussed laser spot across the surface of the autofluorescent slide, whilst simultaneously counting photons using the SPCM output. The program creates a text file of output voltages (analogous to the laser spot's position) and the corresponding number of photons counted at that particular position. These can be plotted to create a photon map: a convolution of the excitation spot and the collection spot. An example of an obtained photon map is shown in Figure 4.3. The position at which the highest photon count occurs corresponds to where the excitation laser should be placed in order to maximise collection efficiency. Therefore the voltages at which the highest count

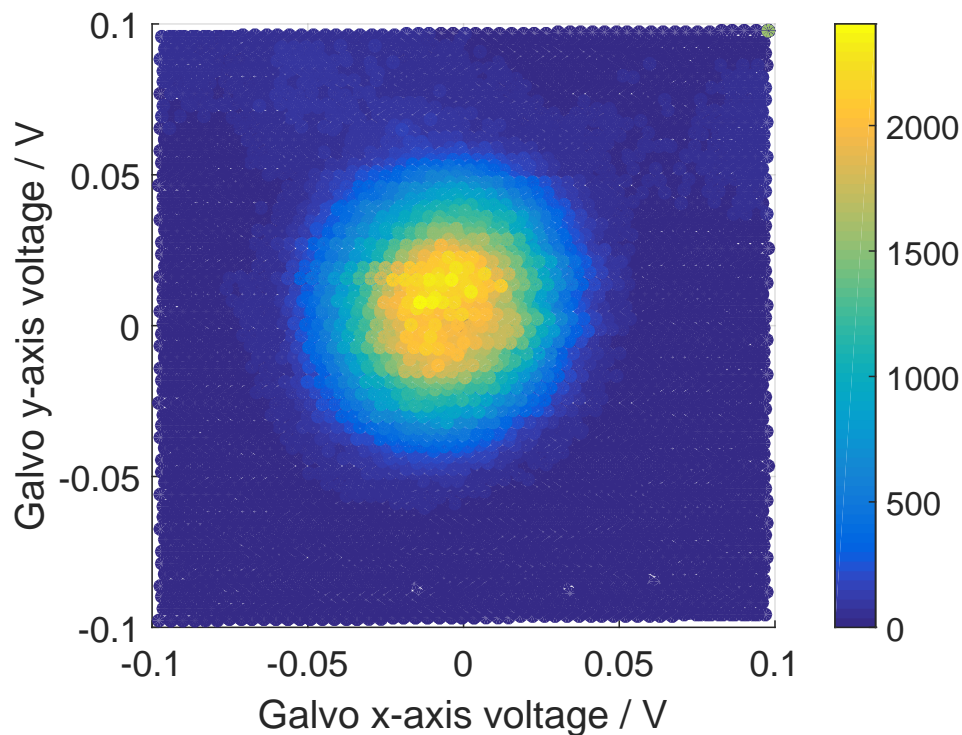


Figure 4.3.: Example of a photon map used to align the two light pathways in the system. The map is a convolution of the excitation and collection spots, with the position of maximum photon counts corresponding to the point where they align. Galvanometer x- and y-axis voltages are shown along the two axes of the image, whilst the colour in z corresponds to the number of photons detected at that position.

occurs are delivered to the galvanometer one final time before the final fluorescence imaging takes place.

In this section the set-up of the fluorescence microscope has been presented, alongside an outline of the method used for aligning the microscope. It has been shown that the microscope consists of two main optical pathways which need to be aligned, such that light is collected from the same area of the sample that is being excited. The sample-scanning nature of the AFM in use allows the sample to be moved through the focussed excitation laser spot, enabling a fluorescence image of a large area of the sample (up to  $170\ \mu\text{m}$  in each axial direction) to be produced.

### 4.3 RESULTS

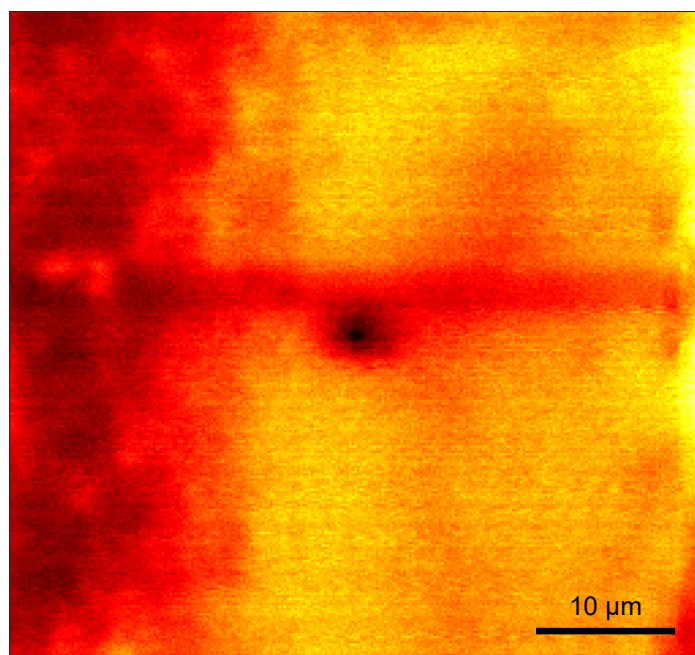
A range of samples were fabricated in order to test various aspects of the microscope. The main objective of this chapter is determining the resolution of the current microscope. Determining the resolution is important because the microscope should be working as close to the diffraction limit as possible: a resolution larger than the diffraction limit would indicate errors in the optical set-up. For example, one obvious cause distortion or blurring in the images could be the lack of a sample clamp, so it is important to rule out this as a problem at this stage. More fundamentally however, a resolution value is needed before tip-enhancement abilities are added to the microscope in order to provide a means of comparison between the conventional fluorescence microscope and the super-resolution microscope that is being developed.

There are two conventional methods for estimating the resolution of an optical system. Many groups opt for measuring the full width at half maximum (FWHM) of individual beads of a sub-diffraction limited size, and then adopting the Rayleigh criterion (Equation 1.2) to calculate the theoretical diffraction limit. However, others argue that this is not a true estimation of microscope performance, and that other factors (such as the SNR) are important for establishing the minimum separation between individual molecules before they will be resolved. For a true estimation, samples with densely-packed fluorescent molecules (such as biological samples) are required. This work will explore both methods for determining the resolution limit.

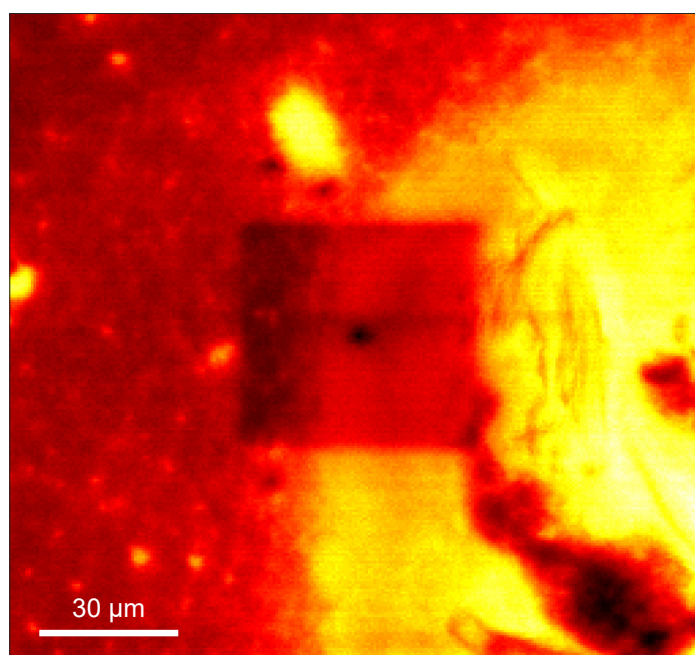
The first sample that was used with the microscope was a thin-film fluorescent polymer called poly(3-hexylthiophene-2,5-diyl) (P3HT). Images of P3HT will be presented in Section 4.3.1. This was succeeded by pre-prepared fluorescently labelled biological samples, and also fluorescent microspheres. Further information relating to the samples, along with their fabrication methods, are found in the relevant sections below.

#### 4.3.1 *Fluorescence Microscopy of Thin-Film Fluorescent Polymer*

Initial testing of the fluorescence microscope was performed on P3HT which is a semiconducting polymer extensively used in organic photovoltaics research. The reason for choosing to image P3HT was its fluorescence spectrum. P3HT has an absorption peak at  $\lambda=443$  nm and an emission peak at  $\lambda=568$  nm. Although peak excitation would not be obtained using the excitation wavelength of 532 nm, the P3HT emis-



(a)  $(50\ \mu\text{m})^2$  scan area



(b)  $(150\ \mu\text{m})^2$  scan area

Figure 4.4.: Images of thin-film P3HT sample. The sample was imaged using a high excitation laser power for  $>30$  minutes (top), before increasing the scan area at the same sample position (bottom). Photobleaching can be seen on the bottom image indicating the original scan area.

sion peak is at a wavelength long enough that it suits the dichroic mirror which is in place to separate the two optical pathways. This, along with the fact that P<sub>3</sub>HT is easily available, made P<sub>3</sub>HT an appropriate choice for initial testing of this particular fluorescence microscope.

To fabricate the sample, 20 mg of P<sub>3</sub>HT was dissolved into 1.5 ml of toluene. This solution was then spin-coated onto a glass coverslip, which was then mounted onto the sample stage of the AFM.

The P<sub>3</sub>HT sample was imaged using a high laser power (60  $\mu$ W to 100  $\mu$ W) for upwards of 30 minutes. Following this, the same sample position was imaged, but a larger imaging area was chosen. The resulting images from this scan can be seen in Figure 4.4.

Figure 4.4b displays a clear central area of reduced photon counts compared to the rest of the image. This second image was obtained by increasing the scan area to 150 microns in each direction, following prolonged exposure to high excitation laser power of a scan area of approximately 50 microns in each direction. This area of reduced counts corresponds to the first imaging area (Figure 4.4a): it is approximately the same size, and some of the features from the first image are still visible in the dimmer central square of the second image. It is highly likely that this area of reduced photon counts is due to photobleaching of the small area of P<sub>3</sub>HT, incurred during the first imaging period at high excitation power. If the microscope is able to detect areas of photobleaching (a reduction in fluorescence), the conclusion can be made that the microscope is able to successfully detect fluorescence emission.

Finding a sample such as P<sub>3</sub>HT and confirming that its excitation and emission wavelengths are suited to this set-up is useful for subsequent investigations. Being able to image a bulk area of fluorescence will be useful for testing the enhancement effect of the microscope later on, because it will consequently be easy to centre the AFM-tip and excitation laser onto an area of fluorescent material for repeated measurements in which to quantify enhancement.

#### 4.3.2 *Fluorescence Microscopy of Bovine Endothelial Cells*

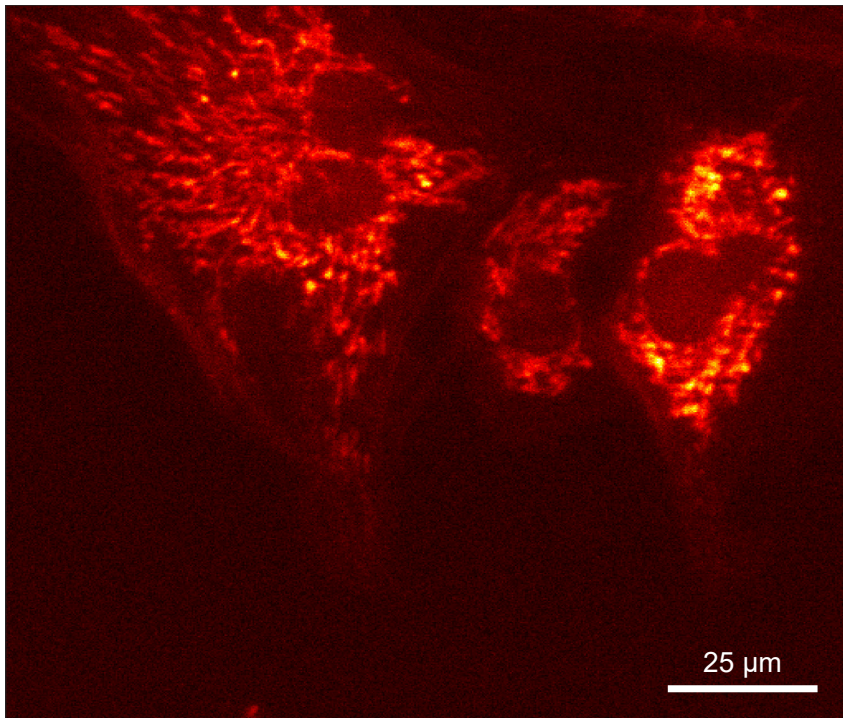
Although the microscope has been shown to be capable of forming fluorescence images of a thin-film fluorescent polymer, the resolution of this non-enhanced optical system has not yet been determined. This section focuses upon determining the resolution of the microscope by imaging a biological sample containing densely-packed fluorophores.

Pre-fabricated fluorescently labelled biological samples, called Fluor-Cells, can be purchased from Thermo Fisher. The fluorescent molecule

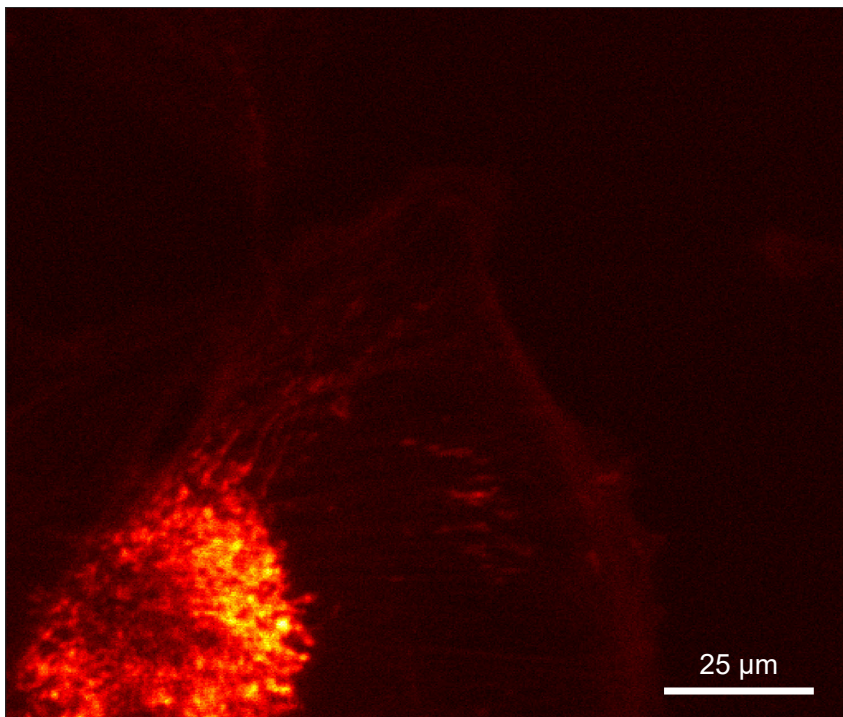
needs to be considered when choosing which sample is optimal for the optical set-up. Pre-fabricated samples usually contain three different fluorescent dyes each labelling a different protein within the biological cells. The absorption and emission spectra of the three dyes are usually spaced far apart so that the labelled areas can easily be distinguished within the final image. For this system, the chosen fluorescent molecule must not only be labelling a cell feature that is densely-packed, but should also have sufficient emission intensity above 561 nm in order to be detected by the optical system. A pre-fabricated sample of bovine endothelial cells from a pulmonary artery meets these requirements, with Mitotracker Red labelling the mitochondria of the cells. Mitotracker Red has an absorption peak at 581 nm and an emission peak at 644 nm. When excited at 532 nm, Mitotracker Red outputs at around 30 % of its relative intensity (i.e., compared with being excited at peak absorption).

Figure 4.5 shows the images obtained of the FluoCell sample. The sample was moved using the AFM stage between image captures in order to obtain images of different areas of the sample. A laser power of approximately 10  $\mu$ W was used for imaging this sample. Mitochondria form a highly dynamic network inside a cell: some of the fibres of this 3D network can be seen most prominently in Figure 4.5a. Within the network of mitochondria, one or several holes are visible, indicating the location of the cell nuclei. The nucleus of the cells are labelled with a blue-fluorescent DAPI molecule (excitation/emission wavelengths of 358/461 nm), which has an absorption peak at a much shorter wavelength than the excitation laser and therefore is not being excited. The F-actin (filamentous actin) in the sample is stained with green-fluorescent Alexa Fluor 488 phalloidin (excitation/emission wavelengths = 490/525 nm); the 532 nm wavelength of the excitation laser is short enough to reach the longest wavelengths of the excitation spectrum of the Alexa Fluor molecule, generating some fluorescence emission at around a 5 % relative intensity. Although the peak emission wavelength occurs at 512 nm and is cut off by the 561 nm dichroic, the tail reaches a wavelength of 675 nm and therefore some of the emission can still be transmitted by the dichroic, and will subsequently be detected by the SPCM. On all three images in Figure 4.5, the actin fibres are visible but at an intensity much lower than the mitochondria as expected. If this microscope was detecting something other than fluorescence (for example, light scatter) all components of these images would show up at similar intensity on the images; their relative intensities however do follow exactly what is expected given the excitation wavelength.

BUILDING A FLUORESCENCE MICROSCOPE

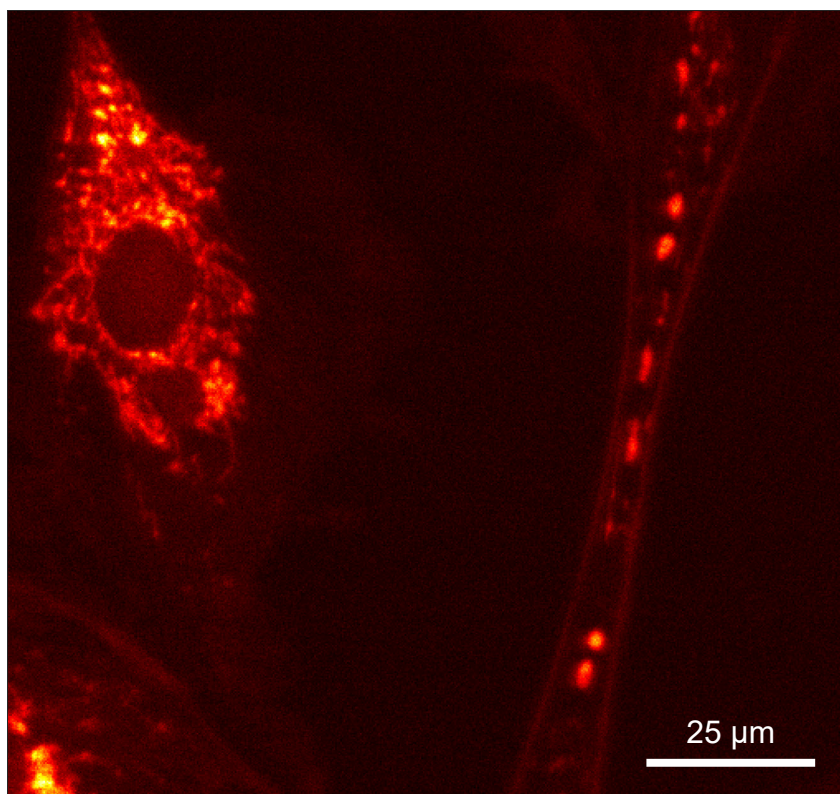


(a)



(b)

Figure 4.5.: Images of different areas of a ThermoFisher FluoCells sample, taken with the current fluorescence system. Sample is a collection of bovine pulmonary artery endothelial cells. Scan areas are all  $(125 \mu\text{m})^2$ .



(c)

Figure 4.5.: (continued) Images of different areas of a ThermoFisher FluoCells sample, taken with the current fluorescence system. Sample is a collection of bovine pulmonary artery endothelial cells. Scan areas are all  $(125\ \mu\text{m})^2$ .

In order to estimate the resolution of the current system, a line profile was taken through the fibrous network of the mitochondria from the image in Figure 4.5a. The location of the intensity profile can be seen in Figure 4.6b, an expanded view of the region highlighted in Figure 4.6a. The profile can be seen in Figure 4.6c. The location of this profile was chosen because the two features which it covers were deemed to have one of the smallest separations compared with other features within the whole image. According to the intensity profile, this distance is  $(1.46 \pm 0.12) \mu\text{m}$ , with the uncertainty value resulting from the fact that the position of features can be determined to an accuracy of  $\pm 0.5$  pixels. It can therefore be said that the resolution of the current system must be at least  $(1.46 \pm 0.12) \mu\text{m}$ .

### 4.3.3 *Fluorescence Microscopy of ThermoFisher Fluospheres*

As was stated earlier, there are multiple methods for estimating the resolution of an optical system. The previous section obtained a value based upon the ability to resolve individual features within a sample of densely-packed fluorescent molecules. To satisfy all approaches, a sample needs to be imaged which contains well-separated objects having a known sub-diffraction limit size. By measuring the FWHM of these objects, an estimation of the resolution can be obtained using the Rayleigh criterion. For this, a solution of microspheres was chosen - spherical latex beads which are filled with fluorescent dyes. The microspheres used in this investigation are FluoSpheres from ThermoFisher. Beads with a fluorescence excitation peak at 540 nm and emission peak at 560 nm were used as these have the highest quantum yield for the 532 nm excitation laser out of all available microspheres. The microspheres have a diameter of 100 nm, a size smaller than the diffraction-limit.

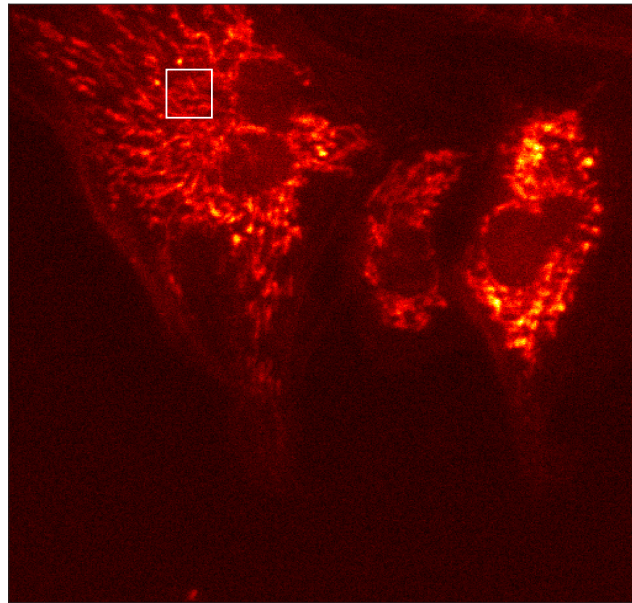
The particular beads used are purchased as microspheres (2%) suspended in an aqueous solution (98%). For sample preparation, the FluoSpheres needed to be diluted in order to reduce the density of beads and ensure that they are well-separated across the glass slide. Firstly, 1  $\mu\text{l}$  of the purchased solution was diluted to 1 part in 1000. This diluted solution was then diluted further in ethanol: the introduction of ethanol means that, when the final solution is pipetted onto a glass slide, the ethanol quickly evaporates to leave a layer of beads dried on the surface of the glass. 1  $\mu\text{l}$  of the previously diluted aqueous solution was diluted with ethanol, again at 1 part to 1000. For the samples developed in this section, 6  $\mu\text{l}$  of the final ethanol solution was pipetted onto a glass slide. The dilution of the microsphere solu-

Table 4.1.: Measured intensity maximum (max) to first minima (min) distances for FluoSpheres. Values all presented in  $\mu\text{m}$  to two significant figures.

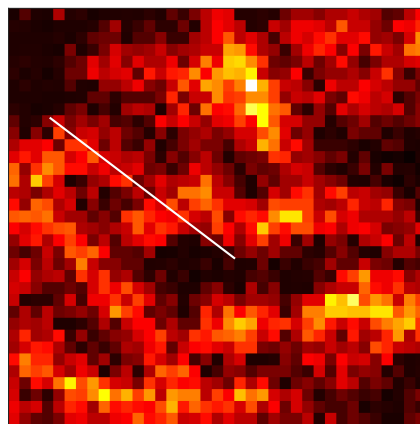
Figure	Max-to-min 1	Max-to-min 2	Average	Standard error
4.7h	2.8	2.1	2.5	0.35
4.7i	2.7	2.0	2.4	0.35
4.7j	2.5	1.6	2.1	0.45
4.7k	1.6	1.5	1.6	0.050
4.7l	2.3	1.6	2.0	0.35
4.7m	2.1	2.0	2.1	0.050
4.7n	2.2	2.9	2.6	0.35

tion was performed by Samuel Barnett. The beads were imaged using a laser power of approximately  $1 \mu\text{W}$ .

Fluorescence images were acquired of one bead within the sample, with the z-position of the objective lens moved between each data acquisition. The aim of this was to measure how the width of the bead in the image changes when moving through the focal point, with the shortest distance indicating that the bead is in focus: the corresponding image can be used to estimate the theoretical resolution of the microscope using the Rayleigh criterion. The images of the FluoSpheres, along with intensity profiles through each image of the bead, are shown in Figure 4.7. It should be noted that there is a reduction in the maximum number of photons detected from the FluoSphere (seen in subfigures h-n), due to photobleaching of the FluoSphere over time. For each profile in 4.7h-n, the distances from the maximum point of intensity (green dashed line) to the first minima (red dashed lines) were measured, providing two maximum-to-minima distances for each image: these distances were averaged to achieve a single maximum-to-minima distance. Full measurements can be seen in Table 4.1. The shortest average maximum-to-minima distance was that calculated from the intensity profile in Figure 4.7k (corresponding image found in Figure 4.7d), with a measured distance of  $(1.6 \pm 0.050) \mu\text{m}$ , suggesting that this is when the bead is in focus. The Rayleigh criterion states that the minimum resolvable distance between objects for an optical system is when the maxima of one point spread function overlaps with the first minima of another. Therefore in order to be resolvable with this optical system, it follows that a spacing of at least  $(1.6 \pm 0.050) \mu\text{m}$  is required.

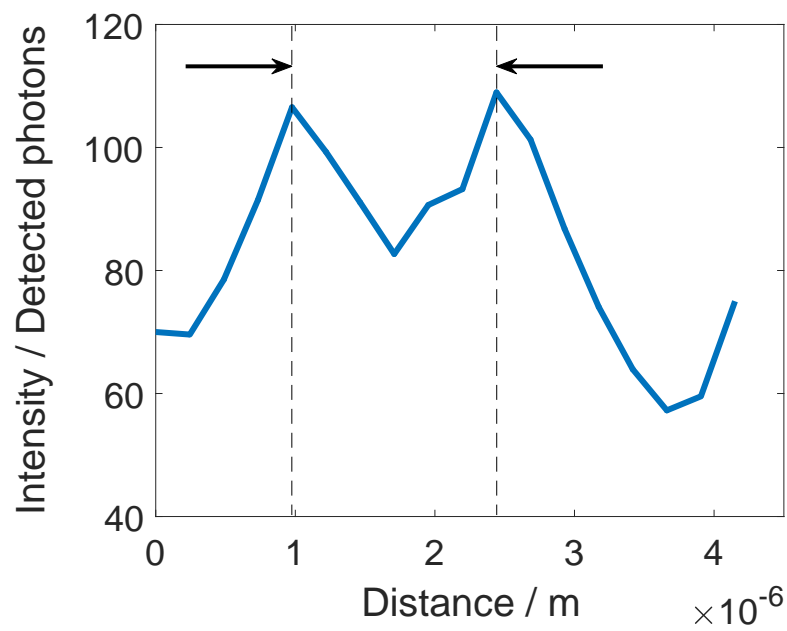


(a)



(b)

Figure 4.6.: Intensity profile through the mitochondrial network in the FluoCell image. Entire FluoCell image is shown in (a), whilst an expanded view of the white-boxed region is shown in (b), with the white line indicating the pixels along which the intensity profile was taken. The resulting profile is shown in (c), where black arrows indicate a separation between features of  $(1.46 \pm 0.12) \mu\text{m}$ .



(c)

Figure 4.6.: (continued) Intensity profile through the mitochondrial network in the FluoCell image. Entire FluoCell image is shown in (a), whilst an expanded view of the white-boxed region is shown in (b), with the white line indicating the pixels along which the intensity profile was taken. The resulting profile is shown in (c), where black arrows indicate a separation between features of  $(1.46 \pm 0.12) \mu\text{m}$ .

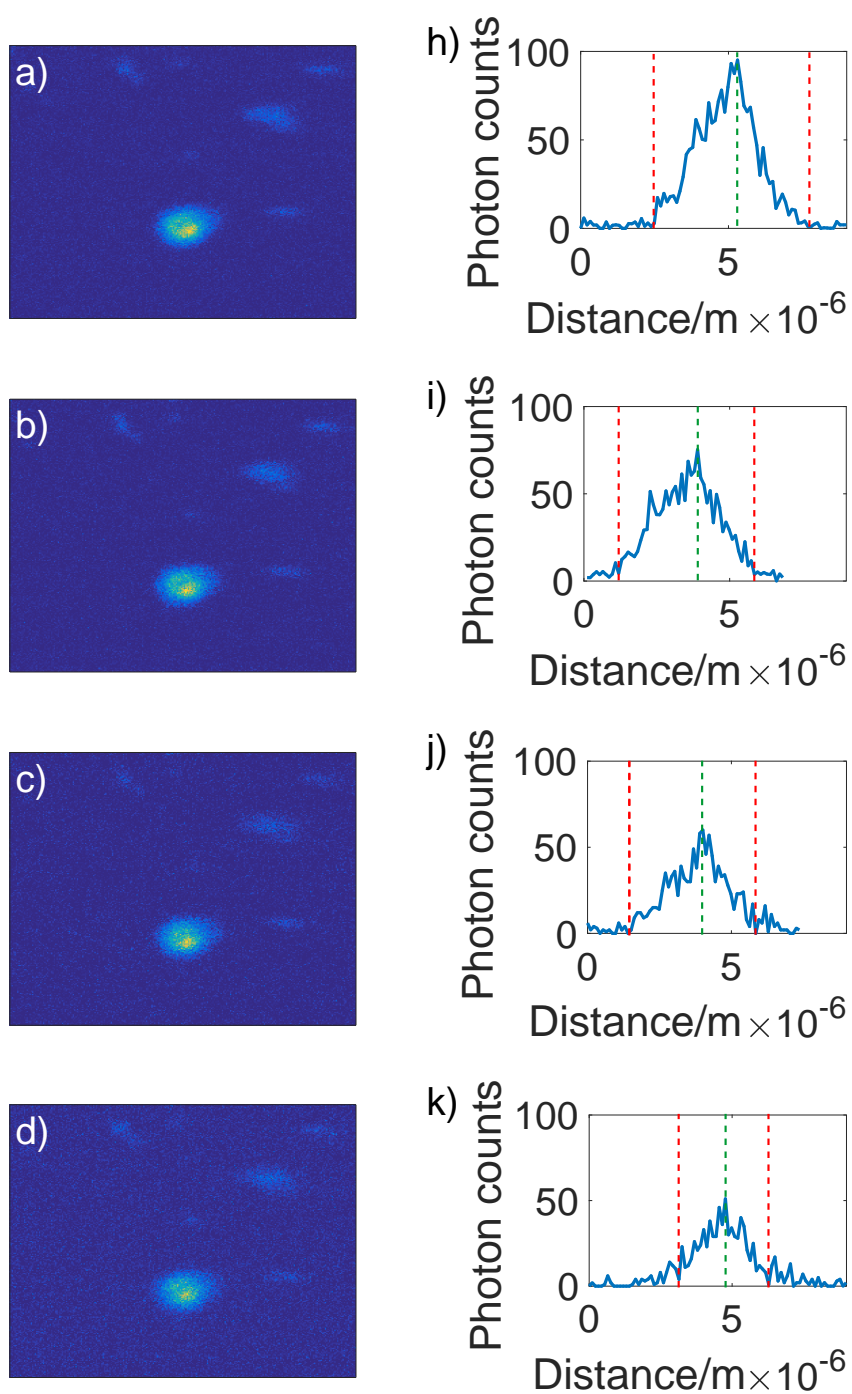


Figure 4.7.: Images and corresponding intensity profiles of one FluoSphere acquired with the fluorescence microscope, with each data set taken at a different focal position. (a)-(g) Fluorescence images of the FluoSphere, with images from top to bottom corresponding to moving from above focus to below focus with respect to the FluoSphere. (h)-(n) Corresponding intensity profiles taken horizontally through the centre of each FluoSphere image, from which the bead-width was determined. Green dashed line indicates intensity maximum, and red dashed lines indicate first minima.

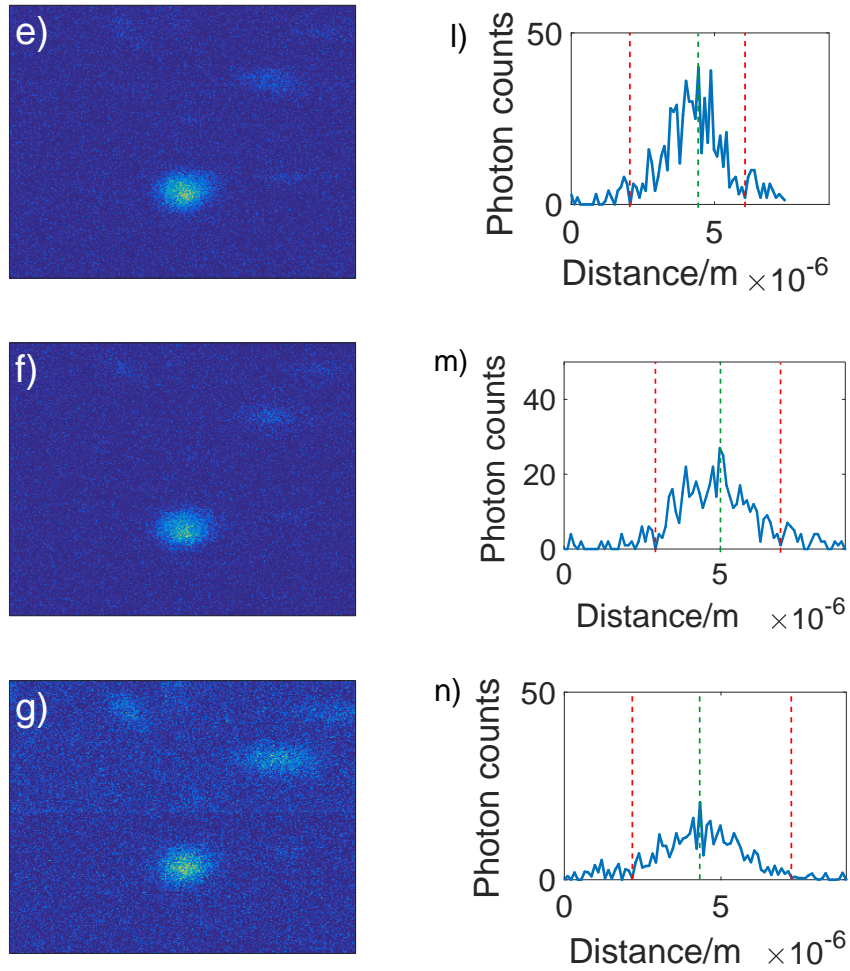


Figure 4.7.: (continued) Images and corresponding intensity profiles of one FluoSphere acquired with the fluorescence microscope, with each data set taken at a different focal position. (a)-(g) Fluorescence images of the FluoSphere, with images from top to bottom corresponding to moving from above focus to below focus with respect to the FluoSphere. (h)-(n) Corresponding intensity profiles taken horizontally through the centre of each FluoSphere image, from which the bead-width was determined. Green dashed line indicates intensity maximum, and red dashed lines indicate first minima.

This value agrees well with theory since, using Equation 1.2 (the theoretical resolution limit for a microscope), the expected resolution limit is  $1.4\ \mu\text{m}$ . This calculation assumes  $\lambda = 560\ \text{nm}$  (the peak emission wavelength of the bead) and an NA of 0.5. While this is out of the range of the measured value, it should be considered that there is a long-pass filter in place in front of the SPCM. This means that only light with a wavelength longer than  $570\ \text{nm}$  is being detected by the system. Along with this, the emission of the bead is a broad spectrum which extends to  $650\ \text{nm}$ . When this wavelength is instead used in Equation 1.2,  $1.6\ \mu\text{m}$  is obtained for the theoretical resolution-limit of the microscope. It can therefore be expected that the resolution-limit of the microscope is a distance up to  $1.6\ \mu\text{m}$ , which is in agreement with the measured result. The microscope is therefore truly diffraction-limited.

#### 4.4 DISCUSSION AND CONCLUSION

This chapter has described the development of a fluorescence microscope which, rather than using a conventional CCD (charge coupled device) camera, uses a SPCM to obtain fluorescence images from a commercially-available AFM. The fluorescence microscope in its current form is comprised of an excitation pathway (for delivering light to the fluorescent sample) and a collection pathway (for collecting the emitted light from the sample and transmitting it to a SPCM). An AFM stage is used to hold the sample in place, and to move the sample in the x- and y-direction such that an image of the whole sample can be formed. Results have been presented which show that the microscope is able to detect fluorescence from a variety of samples, including a thin-film P3HT sample, a biological sample of bovine endothelial cells, and fluorescent microspheres.

Through analysis of intensity profiles of the fluorescent microspheres in this chapter, the fluorescence microscope was determined to be diffraction-limited with a theoretical resolution of  $(1.6 \pm 0.050)\ \mu\text{m}$ . This value assumes that objects can be resolved when they are separated by their maximum-to-minima distance (the Rayleigh criterion). By measuring the distances between fibres of the mitochondrial network, the resolution of the microscope in practice has been determined to be at least  $(1.46 \pm 0.12)\ \mu\text{m}$ , and possibly better, given that these fibres may be separated by distances larger than the diffraction limit. Measuring the resolution of the microscope at this stage is important, because not only does it confirm that the optical system is correctly set-up, but it also provides a quantity on the performance of the microscope be-

fore the tip-enhancement capabilities are added by subsequently aligning the AFM-tip into the excitation pathway. Along with this, it also proves that the lack of a sample clamp in the hardware is not having any adverse effects on the formation of images (e.g., no distortion or blurring due to movement of the sample).

The subsequent step in developing a tip-enhanced fluorescence microscope is to align the AFM-tip with the focussed excitation laser beam. In doing so, the light from the excitation laser can induce the enhancement effect at the tip apex, as well as causing fluorescence emission at the sample. It has been shown in this chapter that the addition of a 2D galvanometer in the excitation pathway allows the position of the incident laser at the sample to be controlled - this is the method used for finely-adjusting the alignment between the two light pathways in this chapter. It will be shown in subsequent chapters that the introduction of this galvanometer is pivotal to also aligning the AFM-tip with the excitation beam.

A SPCM is being used here to enable the detection of individual photons and the correlation of this data to the position of the AFM-tip, ultimately allowing the observation of the enhancement effect once this capability is introduced into the microscope. Although the work performed in this thesis does not investigate other uses for the SPCM, using a single photon detection system could have other potential benefits over the use of CCD devices. Because the aperture of the optical fiber in front of the SPCM acts as a pinhole, the microscope functions as a confocal microscope, rejecting out of focus light and further increasing the signal-to-noise ratio.

Another potential application that the SPCM could be used for is fluorescence lifetime imaging. This could be done by creating an additional pathway for a pulsed laser, and measuring the time between the emission of a photon by the laser and the detection of a fluorescent photon from the sample. Modifying a commercially-available atomic force microscope to obtain information about fluorescence lifetimes as well as topographical measurements could be beneficial, particularly for research in photovoltaic devices. Fluorescence lifetime measurements are often taken of the Perovskite layer in solar cells to indicate the efficiency of the device; long lifetimes signify that an electron and hole (created when a photon is incident on the layer) can survive as individual particles for long periods without recombining into an exciton, which means that more of the liberated electrons and holes can be swept away to produce a current. The AFM in this scenario could be used to investigate how defects in the layer (for example, grain size) effect the efficiency of the devices. Alongside this potential applica-

tion, adapting this instrument to measure fluorescence lifetimes could provide an alternative method for detecting fluorescence enhancement to that presented in this thesis, since the AFM-tip modifies the fluorescence lifetime of molecules within its immediate vicinity to increase the number of photons coming from a highly localised area.

# 5

---

## USING CORRELATIVE MICROSCOPY TO ALIGN THE TIP-ENHANCED FLUORESCENCE MICROSCOPE

---

### 5.1 INTRODUCTION

It was shown in the previous chapter that hardware had been developed to adapt a commercially-available atomic force microscope (AFM) such that it can also obtain fluorescence images through use of a single photon counting module (SPCM). The next step towards realising a tip-enhanced fluorescence microscope is to align the probe of the AFM with the excitation beam used for inducing fluorescence in the sample. By having light of a particular polarisation incident on the sharp tip, the electric field in the vicinity of the tip can be modified, thereby affecting the fluorescence lifetime of any fluorescing molecule in the surrounding area.

Several methods have been trialled in an attempt to align the AFM-tip with the excitation laser. The method outlined in this chapter exploits the fact that AFM measurements are unaffected by the presence of the focussed excitation spot underneath the AFM-tip, enabling fluorescence data to be obtained simultaneously alongside AFM measurements. A MATLAB program was developed which compares the sample areas of these two images, and induces a corresponding response in the hardware to move the excitation laser into alignment with the AFM-tip. The result of this is that data is always being acquired from exactly the same area of sample for both techniques. An additional advantage of the alignment method developed here is that the program can operate continuously alongside data acquisition, in order to first obtain and then maintain alignment for long timescale imaging sessions, correcting for any drift in the microscope.

Aside from tip-enhanced fluorescence microscopy, this program has other immediate applications in correlative microscopy. It is usually the case that such correlative microscopy techniques are performed sequentially by imaging large areas with both techniques, and then performing post-processing methods to overlay the data following ac-

quisition [40, 134, 135]. Simultaneously acquiring data paves the way for applications where the mechanical properties of a structure of interest can be tracked over time, because the fluorescence image can be used to determine areas of interest within the sample, which can immediately be probed by the AFM-tip. It also eliminates the need to obtain data over large fields-of-view, because the structure of interest will always be present in both images.

## 5.2 THEORY

Using the experimental set-up outlined in Figure 4.1, simultaneous measurements of height<sup>1</sup> and fluorescence can be obtained for the sample positioned at the AFM stage. Figure 5.1 demonstrates how both of these images are formed. The AFM used in this thesis is a sample-scanning AFM, where the AFM-height image is formed by scanning the sample in the x- and y-direction underneath a stationary AFM-tip. At the same time, a focussed excitation spot is also incident on the sample, at a particular distance  $(x,y)$  from the location of the AFM-tip. Since the sample will also be scanned through the incident laser beam, a fluorescence image will also be formed of the sample area located  $(x,y)$  from the AFM-tip. The most likely  $(x,y)$  offset between these two images (i.e., how far away these images are from acquiring data of exactly the same area of sample) should be indicative of the  $(x,y)$  distance between the AFM-tip and the incident focussed excitation beam on the sample. Therefore, translating the incident beam until zero offset is achieved between the fields-of-view will result in the incident beam becoming aligned with the AFM-tip.

Zero offset between the two images can be achieved by repositioning the focussed excitation beam to bring it into alignment with the AFM-probe<sup>2</sup>; in the optical set-up used here, this is done by applying voltages to a 2D galvanometer positioned in the excitation beam path. The challenging part of this technique is determining the voltages required to correct for a particular  $(x,y)$  offset between the two images. In the case of this system, there are two independent sets of axes: there are the axes of the AFM stage, from which the  $(x,y)$  offset between the two images is measured, and there are the axes of the 2D galvano-

---

<sup>1</sup> or of any other measurement the AFM is capable of (for example, adhesion, DMT modulus etc.)

<sup>2</sup> For the work performed in this chapter, the single-mode optical fibre (used for collection) was replaced with the multi-mode optical fibre, such that fluorescence can be collected from a larger area of sample, and that realignment of the excitation and collection pathways was not required after every movement of the excitation beam

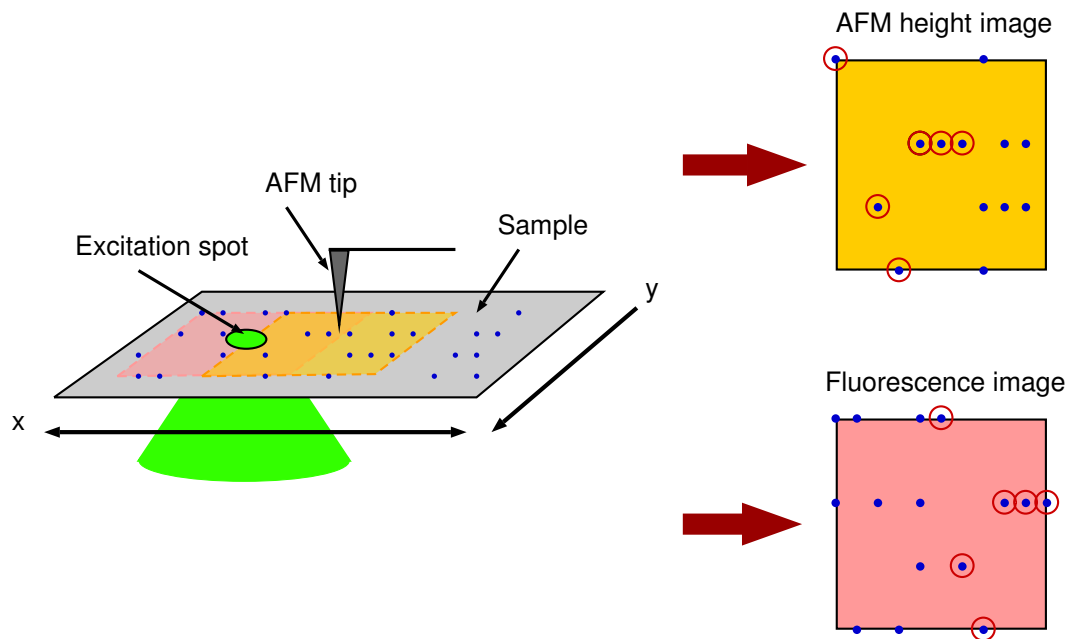


Figure 5.1.: Formation of AFM-height image and fluorescence image. The AFM-height image (yellow) is created by scanning the sample in the x- and y-direction underneath the stationary AFM-tip. Likewise, a fluorescence image (pink) is obtained by scanning the sample the same x- and y-distance through an incident excitation beam, with the fluorescence emission from this particular location being detected by a SPCM. The difference in position of the same features within each image (shown circled in red) indicates the offset between the two fields-of-view, i.e., the distance between the AFM-tip and the incident laser beam.

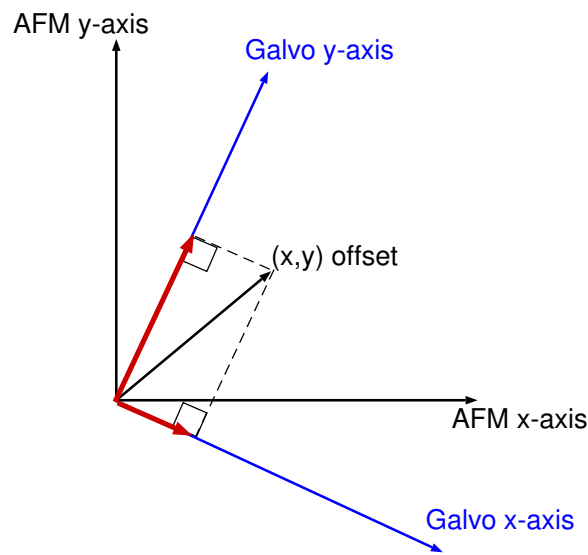


Figure 5.2.: Galvanometer (galvo) and AFM axes representation. The optical set-up is comprised of two independent sets of axes. The  $(x,y)$  offset between the two images is calculated with respect to the AFM axes. In order to calculate the required movement along the galvanometer axis (shown in red), the system needs to be thought of as a series of vectors and a subsequent scalar product calculation needs to be performed.

meter along which the incident excitation spot moves. Because the AFM system is independent of the galvanometer system, it can be expected that these two sets of axes will be offset from each other, so movement of the beam through just one axis of the galvanometer will induce a change in the field-of-view of the fluorescence image in both the  $x$ - and  $y$ -directions. A diagram of this is shown in Figure 5.2. If the system is thought of as a series of vectors, the movement required along the galvanometer axis in order to go from an  $(x,y)$  offset to a  $(0,0)$  offset can be determined by an inner product calculation. If the vector representations of the galvanometer axes can be found in terms of the AFM axes, taking the inner product of the offset vector with the unit vectors of both the galvanometer  $x$ - and  $y$ -axis allows the components highlighted in red on Figure 5.2 to be found: these are the components of the offset vector which are along the directions of the galvanometer axes.

### 5.3 METHOD

#### 5.3.1 *The MATLAB Alignment Program*

A MATLAB program has been developed which correlates sample features across two images that have been acquired simultaneously: an AFM image and a fluorescence image. By correlating features, the offset between the fields-of-view can be calculated, indicating the distance that the incident beam needs to be translated in order to become aligned with the AFM-tip. The program runs continuously, repositioning the galvanometer to correct for drift in the hardware.

To ensure that the program only operates on new data files (and not needlessly running constantly in the background), a data file search function needed to be developed. The AFM writes new data files into a folder chosen by the user, with file extension in the form of a three-digit number (for example `CaptureFile.000` or `CaptureFile.001`). The extension number indicates the order in which the files were captured, whilst the file name `CaptureFile` is the default for Bruker acquisition software. The program therefore starts by looking for the highest extension number attached to a `CaptureFile` within the folder to which the data is being written - for this reason, it is important that the files are not renamed from the default by the user during data acquisition. If a file is found with a higher extension number than that which was previously opened, then this new file is opened by the program. If the highest extension number is equal to that previously opened then the program waits 10 seconds before searching again: this is to save computing resources. When the capture file is opened, data corresponding to all of the images within the file is read and formatted. The AFM images contained within the file are then displayed and the user is prompted to enter the name of the parameter (e.g., height, adhesion) corresponding to the image that they wish to correlate with the fluorescence image. The chosen image and the fluorescence image are then opened in a new user interface.

A manual coordinate selection function has been developed based on a function called `ginputc` produced by Jiro Doke [136], available online. The function prompts the user to select three pixels on the first image in the user interface, corresponding to different prominent features in the image. Following this, the user is prompted to select three pixels corresponding to these same features in the second image. As the pixels are chosen, they are labelled in order of selection 1-3: the points should be selected in the same order for each image. The three (x,y) coordinates of the corresponding pixels between each image are

subtracted from each other to calculate three offset values; these offset values are then averaged to obtain a final estimate of the offset between the two images.

The offset in pixels can be converted to an offset in microns using data extracted from the capture file, i.e. the number of pixels per image and the total AFM scan area. This value is then input to a function containing galvanometer calibration data, which converts the offset to a set of voltages required by the galvanometer to move the excitation laser along the offset. The voltages are applied to the galvanometer using a NI-USB-6351 DAQ card, controlled using LabVIEW. To output the required voltages to LabVIEW, they are written to a .mat file in MATLAB. New voltages are written to this file as they are calculated from succeeding imaging frames, whilst a custom-made LabVIEW program reads values from this file continuously and outputs them to the galvanometer.

### 5.3.2 *Calibrating the Galvanometer*

To calibrate the galvanometer, the magnitude and direction of movement of the incident excitation laser spot - per volt delivered to each axis of the galvanometer - needed to be calculated. This can be determined by measuring the change in calculated offset between the AFM-height image and the fluorescence image with changes in galvanometer voltage, because the position of the AFM-tip remains constant throughout. The galvanometer has two axes of movement, allowing the excitation spot to move in two directions, each of which needs to be calibrated. This was done by changing the voltage along one axis only, whilst keeping the voltage on the other axis constant. The gradients of the galvanometer axes (as described in Figure 5.2) were calculated by measuring the change in offset along both the x- and y-directions between data points. Offset values were calculated for 25 galvanometer voltage positions, allowing 5 estimates each for the galvanometer x- and y-axis gradients (see Figure 5.3).

### 5.3.3 *Sample Preparation*

Three different samples have been used to test the ability of the program to achieve alignment: two fluorescent, and one non-fluorescent. The non-fluorescent sample is a sample of polyhydroxybutyrate-co-valerate (PHB-V) spherulites. Preparation of this sample has been described previously [137]. In brief, PHB-V was melted onto a glass

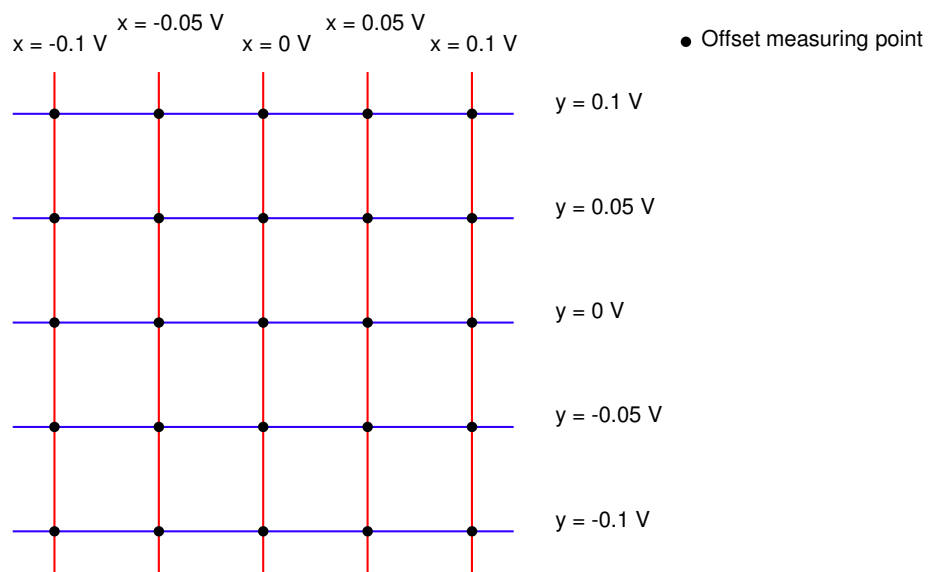


Figure 5.3.: Galvanometer voltage combinations used for calibration. 25 sets of  $(x,y)$  voltages were sent to the galvanometer axes, and the offset in the fields-of-view between the AFM and fluorescence images was measured for each voltage set. By measuring the change in the offset between each measuring point, the vectors of the galvanometer axes could be determined in terms of the AFM axes.

coverslip by heating on a hot plate at 200 °C for 2 minutes. The molten PHB-V was then scraped with a razor blade to obtain a flat surface, and allowed to crystallise at room temperature, forming irregular structures across the slide to aid correlation. Spherulite sample preparation was performed by Dr Nic Mullin.

This work also makes use of a phase-separated fluorescent poly(3-hexylthiophene-2,5-diyl) (P<sub>3</sub>HT) sample. To create this sample, P<sub>3</sub>HT and polystyrene were both dissolved separately in a common solvent (o-Xylene); the P<sub>3</sub>HT solution (2%) was then heated to 70 °C before being mixed with the polystyrene solution (2%) at a ratio of 50:50 and spin-coated onto a glass coverslip. P<sub>3</sub>HT sample preparation was performed by Dr Andrew Parnell.

Another sample used in this work was a sample of fixed HeLa cells. HeLa cells were grown in a (10%) fetal bovine serum (FBS) in Dulbecco's modified eagle medium (DMEM) with penicillin-streptomycin at 37 °C. Cells were then washed with phosphate buffered saline (PBS) three times, with each wash lasting 5 minutes before being fixed with 4% paraformaldehyde for 20-30 minutes. The fix was removed and the cells were washed again three times at five minutes for each wash. After the third wash, a phosphate buffered saline with triton (PBST) was added to the cells for 3-5 minutes to make the cell membrane permeable. The PBST was removed and the cells washed with PBS again, before bovine serum albumin (BSA) was then added for 20-30 minutes as a blocking reagent. The F-actin of the HeLa cells was then stained with AlexaFluor 647 Phalloidin. After adding the stain solution to the cells and leaving for 20-30 minutes, the cells were washed with PBS three times for 5 minutes each in one final cleaning stage. For imaging this sample only, the 570 nm longpass filter in the optical set-up was removed and switched for an alternative longpass filter with a cut-off wavelength of 665 nm. HeLa cell sample preparation was performed by Liyana Peedikakkal.

For all samples, coverslips are used for imaging without mounting onto microscope glass slides to leave the surface of the sample exposed for AFM imaging.

## 5.4 RESULTS

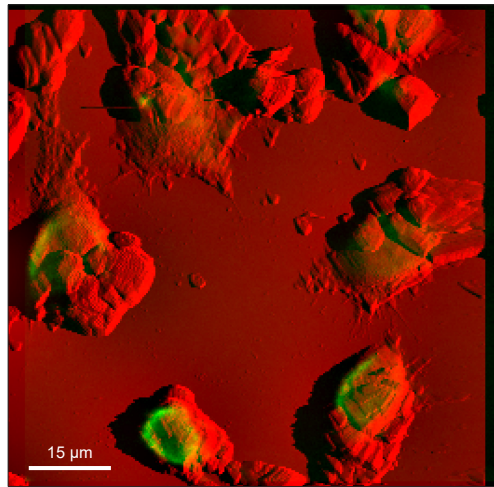
### 5.4.1 *Demonstrating the Ability to Obtain Beam-Tip Alignment*

Two fluorescent samples have been used to test the ability of the program to achieve beam-tip alignment in the instrument. The samples

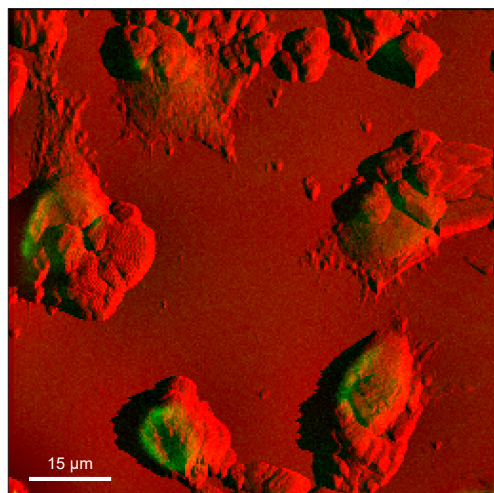
have been chosen because of their non-repetitive structures, allowing easy correlation between features in the two images.

The first sample used to test the program was a sample of HeLa cells fluorescently labelled with AlexaFluor 647 Phalloidin, imaged using a laser power of approximately 1 mW. By selecting pixels in both the AFM image and the fluorescence image which correspond to the same sample features, the offset at the start of the imaging session was determined to be  $(3.2 \pm 0.5)$  microns in magnitude. After three iterations of the MATLAB program, the offset was calculated to be  $(1.1 \pm 0.5)$  microns in magnitude. The images before and after using the program have been overlaid at their calculated offsets in Figure 5.4. The alignment program has managed to reduce the offset between the two different fields-of-view, indicating that the incident beam has moved to within approximately one micron of the AFM-tip position.

The second sample used to test the program was a phase separated polymer blend of poly(3-hexylthiophene-2,5-diyl) (P3HT) and polystyrene, with the P3HT having a fluorescence emission peak at approximately 580 nm [138] [139] [140]. The sample was imaged using a laser power of approximately 60  $\mu$ W. The initial fluorescence and AFM-height images, both with a scan area of  $(164 \times 164)$  microns, can be seen in Figures 5.5a and 5.5b respectively. The starting offset between the two images was determined to be  $(0.0 \pm 0.9)$  microns in the x-direction, and  $(12.6 \pm 0.5)$  microns in the y-direction, corresponding to 0 and 20 pixels in the image respectively - a much larger initial offset than with the previous sample. The images have been overlaid at this position in Figure 5.5c. The offset was tracked for a total of four imaging frames on the same area of sample with use of the MATLAB program to readjust the 2D galvanometer. Because the excitation laser is being translated over a purposely larger distance for this experiment, the collection and excitation pathways needed to be realigned after the first frame, before continuing with the image acquisition for the second frame. The change in offset between the fluorescence and AFM images for the four frames can be seen in Figure 5.6. It can be seen that the program has managed to move the offset between the two images from a value of  $(12.6 \pm 1.0)$  microns to  $(0.6 \pm 0.6)$  microns after just three iterations of the galvanometer's orientation. The separate fluorescence and AFM images obtained in this fourth and final imaging frame, as well as an overlay at the correct offset, can be seen in Figure 5.7. These results show that the program can successfully obtain beam-tip alignment, even from initial offsets which are relatively large (greater than 12 microns). Moreover, results suggest that the calibration of the galvanometer has been accurate enough that alignment



(a)



(b)

Figure 5.4.: Overlaid fluorescence (green) and AFM PeakForce error (red) images taken simultaneously before (a) and after (b) use of the MATLAB program. Images show HeLa cells labelled with AlexaFluor 647. Offset has been reduced from  $(3.2 \pm 0.5)$  microns in (a) to  $(1.1 \pm 0.5)$  microns in (b) after three iterations of the galvanometer orientation.

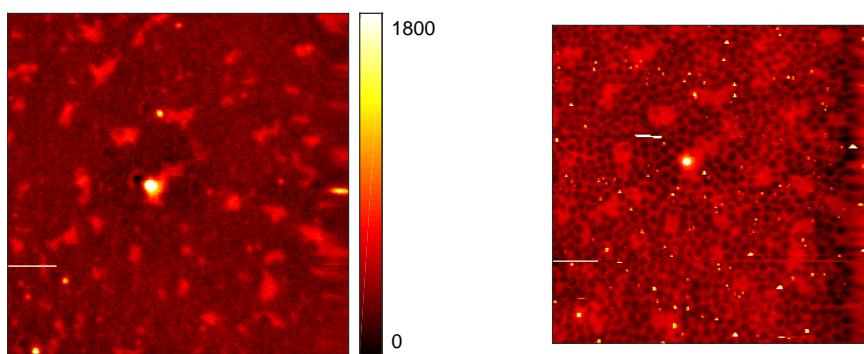
to within one micron can be achieved within just a few iterations of the program, no matter what the magnitude of the initial offset is.

It is evident from Figure 5.7a that photobleaching of the sample has occurred. The maximum number of detected photons has reduced (indicated by the maximum value on the colourbar in Figures 5.5a and 5.7a), the signal-to-noise ratio has reduced, and there are also areas in the image which have started to appear completely dark. As fluorescent samples bleach, they are not useful for testing the long-term stability when using the MATLAB program, i.e. how well an offset within one micron could be maintained over time. For this reason, a non-fluorescent sample was also imaged using the system, as will be shown in the following section.

#### 5.4.2 *Demonstrating the Ability to Maintain Beam-Tip Alignment*

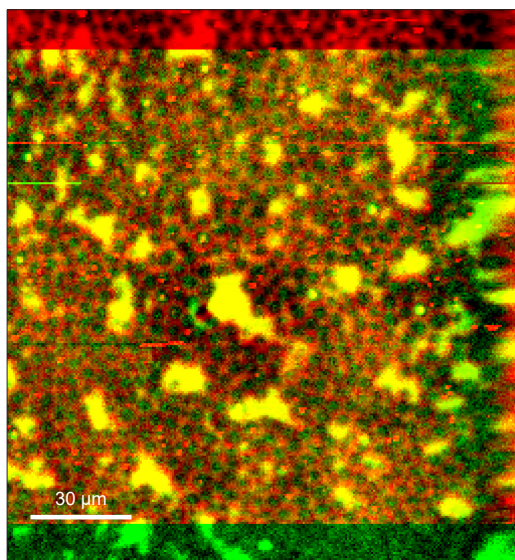
The non-fluorescent sample chosen to test the long-term stability of the program was a sample of poly(hydroxybutyrate-co-valerate) (PHB-V) spherulites. This sample was chosen because it contains large (20  $\mu\text{m}$  to 40  $\mu\text{m}$ ) non-repeating structures, making it easier to identify areas of similarity in both images. The optical image being formed here is due to light-scatter from the underside of the sample. For this, the 570 nm longpass filter was removed from the optical set-up such that all reflected light is detected by the SPCM. It was found that, even with the presence of the longpass dichroic mirror with a cut-off wavelength of 561 nm, enough of the reflected 532 nm laser light was passed through the dichroic to form an adequate optical image. To avoid damage to the SPCM, imaging was performed using a very low laser power (approximately 100 nW).

As before, the MATLAB program was used to determine the offset between the scatter image and the AFM-height image of the same area of sample, and this offset was monitored throughout the imaging session. The scan size for this sample, and therefore the size of these images, was (137  $\times$  137) microns. The results of this can be seen in Figure 5.8. The offset between the two images at the start of the session was determined to be  $(15.9 \pm 0.4)$  microns. After two iterations of the galvanometer, an offset of  $(0.8 \pm 0.5)$  microns was obtained. Again, for this data set, the excitation and collection pathways in the optical set-up needed to be realigned after the first iteration of the galvanometer orientation, because the focussed excitation laser was purposely positioned far from the AFM-tip (and therefore out of the collection area of the optical fibre). It can be seen that, for the remainder of the imaging session, the measured offset fluctuated mostly between



(a)

(b)



(c)

Figure 5.5.: Initial offset as determined by the MATLAB program. Fluorescence image (a) and AFM-height image (b) taken of the same area of the P3HT sample simultaneously. The initial offset between the two images was determined to be  $(12.6 \pm 1.0)$  microns in magnitude. The two images have been overlaid at this position in (c), where the fluorescence image is displayed in green, and the height image is displayed in red. Colourbar in (a) shows number of photons detected per pixel.

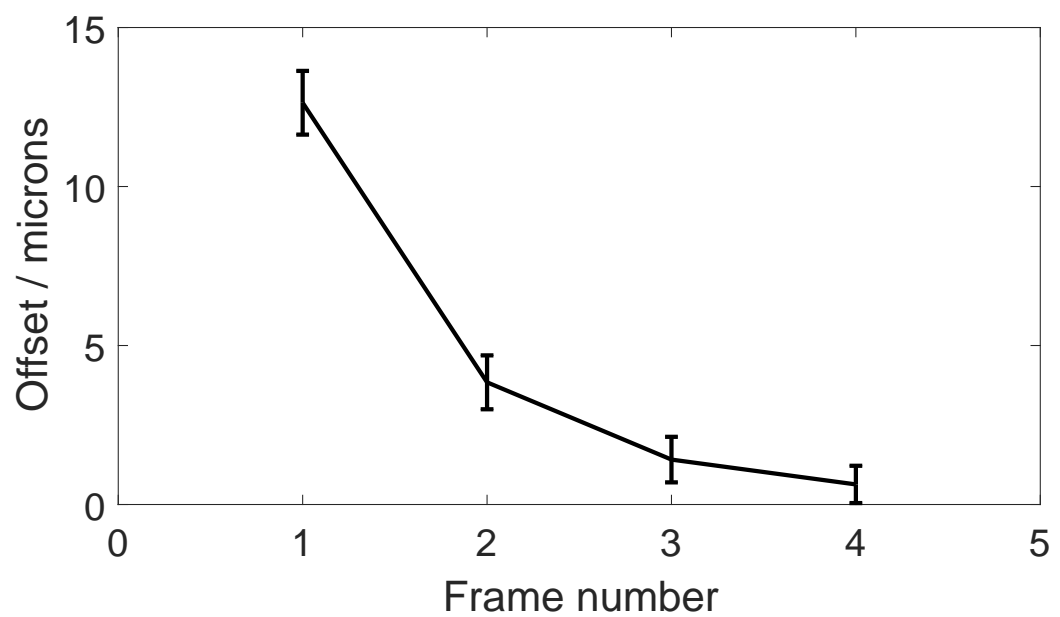
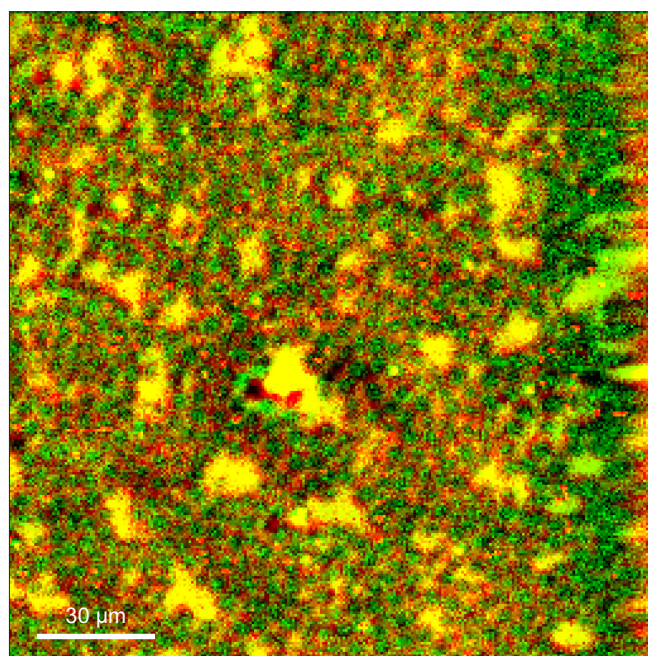
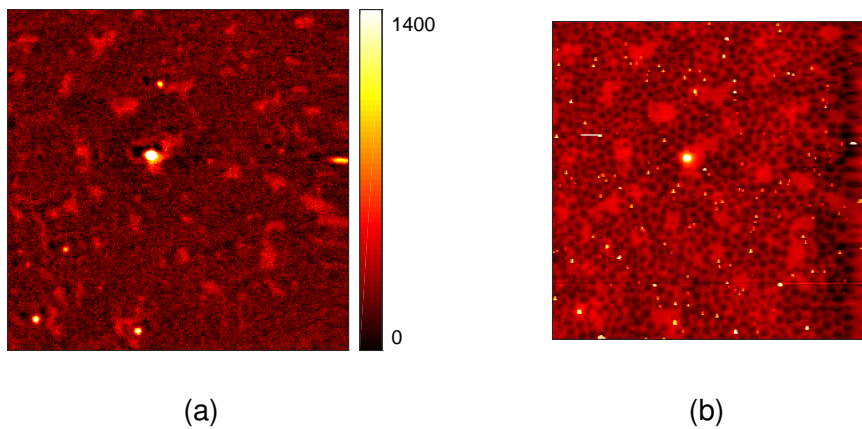


Figure 5.6.: Offset in microns between the fluorescence and AFM-height images for the duration of the imaging session. Initially, the offset is determined to be  $(12.6 \pm 1.0)$  microns in magnitude by correlating pixels of key features in the images. By adjusting the orientation of the galvanometer, an offset of  $(0.6 \pm 0.6)$  microns is achieved after three iterations of the program.



(c)

Figure 5.7.: Determined offset after three iterations of the galvanometer by the MATLAB program. Fluorescence image (a) and AFM-height image (b) of P3HT sample were acquired simultaneously. The offset between the two images has been determined to be  $(0.6 \pm 0.6)$  microns and the two images have been overlaid at this position in (c), where the fluorescence image is displayed in green, and the height image is displayed in red. Colourbar in (a) shows number of photons detected per pixel.

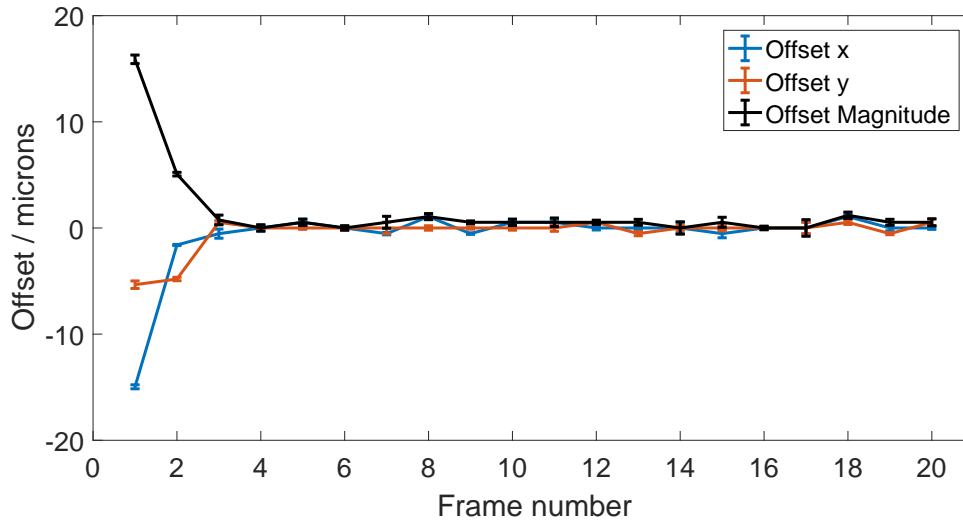


Figure 5.8.: Offset in microns between the fluorescence and AFM-height images of PHB-V spherulites for the duration of the imaging session. Initially, the offset is determined to be  $(15.9 \pm 0.4)$  microns in magnitude by correlating pixels of key features in the images. By adjustment of the galvanometer orientation, an offset of  $(0.8 \pm 0.5)$  microns is achieved after two iterations of the program. An alignment to within  $(1.2 \pm 0.3)$  microns is maintained over the remaining 18 imaging frames.

zero and one micron: the largest offset obtained for the subsequent 18 frames was  $(1.2 \pm 0.3)$  microns, recorded on frame number 18 out of 20. The offset between the two fields-of-view fluctuates over large periods of time, even if alignment has already been achieved, due to drift in the hardware. It can be seen from the results here that this alignment method will correct for this drift. Fundamentally, the ability of the program to maintain alignment over time is reliant on human judgement, and the ease with which the features in both images can be correlated with each other. The results here suggest that, as long as features can be correlated, the program is able to maintain alignment between the AFM-tip and the excitation beam over an unlimited period of time.

## 5.5 DISCUSSION

This chapter has presented a MATLAB program which has been developed to calculate and apply voltages to a 2D galvanometer, based upon correlating features between two different images of the same

sample area. The offset between an optical and AFM-image is calculated, indicating the  $(x,y)$  distance between the incident excitation laser and the AFM-tip. The voltages required to move the incident beam towards the AFM-tip with the aim of achieving zero offset are calculated using calibration data. The objective behind creating this program was to develop software which operates alongside the microscope, continually analysing newly-captured images to determine the offset between the incident beam and the AFM-tip at that time. The program would work to obtain alignment between the two, and then maintain the alignment for the duration of the imaging session.

Three different samples were used to test two aspects of the program: firstly, how quickly a zero offset between the two images can be achieved, and secondly how long this offset can be maintained for. The first was a sample of HeLa cells labelled with AlexaFluor 647 Phalloidin. It was found that the offset between the two images at the start of the imaging session was  $(3.2 \pm 0.5)$  microns in magnitude, whereas after three iterations of the MATLAB program, the offset was reduced to  $(1.1 \pm 0.5)$  microns in magnitude. The second sample was a phase-separated polymer blend of polystyrene and P3HT. It was shown that the offset between the fluorescence image and the AFM-height image went from a larger offset of  $(12.6 \pm 1.0)$  microns to  $(0.6 \pm 0.6)$  microns, again after only three iterations of the galvanometer. Thereafter with both samples, the fluorescence image showed signs of photobleaching, making it more difficult to determine key features for the correlation process. It was evident that this sample would not be useful for testing the long-term stability of the MATLAB program, unless the sample area was changed throughout to prevent photobleaching. Changing the scan area with a sample of this type is not really possible, given that the image area needed to be large in order to view all structures of interest: the maximum scan size possible with the AFM is  $(170 \times 170)$  microns which was already being approached, and to image anything outside of this area the tip needs to be withdrawn from the surface and the sample repositioned, an act which would affect the offset already achieved. For this reason, a non-fluorescent sample was chosen to test how well the offset can be maintained over a long period of time. Imaging a non-fluorescent sample by scattering the incident light off its surface should be a suitable replacement for fluorescent imaging in this demonstration, since light follows the same pathways through this optical system for both modalities and an image is formed in the same way.

The non-fluorescent sample used were PHB-V spherulites on cover-glass, crystallised from a melt at room temperature. It was found that

the MATLAB program changed the offset between the two images from  $(15.9 \pm 0.4)$  microns to  $(0.8 \pm 0.5)$  microns after just two iterations of the galvanometer. The sample was imaged for a further 18 imaging frames to test how well this offset could be maintained. It was found that the offset stayed broadly between zero and one micron for the remainder of the imaging session, with the largest offset achieved in this period being  $(1.2 \pm 0.3)$  microns. In the final frame of this imaging session, the offset was determined to be  $(0.5 \pm 0.4)$  microns. Given that each capture file took approximately seven minutes to acquire, and only alternate files were used for calculations to account for movement of the galvanometer after each capture, this amounts to approximately four hours over which the offset could be maintained. There is no apparent reason why this offset would not be maintained for longer if required. The main limiting factor here is human judgement, which is affected by how alike the structures in the two images look. If the similarities in the two images are not obvious (for instance, if fluorescent structures are housed in a sac, as many biological samples are), it may be more difficult to determine the coordinates in the image which correspond to the same features. As well as this, the height image is fundamentally a map of the top of the sample, whereas the fluorescence image is an image of the bottom of the sample. It is important to remember that these images may not look exactly the same.

There are a number of improvements that could be made to the program to increase its accuracy and usability. The first would be creating a fully-automated program. Currently, alternate data acquisitions are used for determining the offset. This is because the calculation takes around one minute to complete, and a significant portion of the next imaging frame has been captured before the galvanometer readjusts to its updated position, meaning that this frame cannot be used for the subsequent calculation. The program as it stands relies upon the user aborting the saving of new capture files during the offset calculation and then resetting the capture again for the next frame. One improvement could be to use the "end of frame" TTL output from the AFM, alongside the input to the galvanometer, so that the program determines when to open the most recent capture file and perform the measurement. However, the most difficult aspect of creating a fully-automated program will be developing a method for computationally determining the offset rather than relying upon user-input. Chapter 6 will outline the work that has been undertaken towards achieving this goal.

The MATLAB program works well. Achieving an offset to within one micron after just a few iterations of the program - especially from

a relatively large offset (greater than 12 microns) - means that the program is performing its proposed function successfully. This is the first time that a galvanometer has been calibrated and used in such a way. Although it remains to be seen whether this program can achieve the beam-tip alignment accuracy required for tip-enhancement processes, an accuracy to within one micron is precise enough to unlock the ability to achieve simultaneous fluorescence and atomic force microscopy, ensuring that the feature of interest is definitely always in the field-of-view for both techniques.

## 5.6 CONCLUSION

This chapter has reported the development of a manually-operated MATLAB program to align an AFM-tip with an incident excitation laser spot. The program works by correlating sample features between an AFM image and a fluorescence image which have been acquired simultaneously, and determining how far away the two images are from having exactly the same field-of-view. The offset is determined by asking the user to select the pixels on the two images which correspond to the same features within the sample. Because the AFM image is governed by the AFM-tip and the fluorescence image is governed by the position of the incident beam, the distance between the two images is equivalent to the distance between the AFM-tip and focussed excitation spot.

Overall, the MATLAB program performed well, being able to reduce the offset between the two images from a value greater than 12 microns to within one micron after just a few iterations of the galvanometer orientation. The main limiting factor of this alignment program is the ability of the user to determine the same features in both images. Providing that it is not difficult to distinguish features in the images, this offset can also be easily maintained over an imaging period of several hours.

Although the main purpose of the program is to obtain beam-tip alignment for tip-enhanced fluorescence purposes, and then maintain this alignment to correct for any drift in the hardware during the imaging session, the program also has immediate uses in the field of correlative microscopy. Here, it has been shown that a commercially-available AFM can be adapted to also collect fluorescence data, simultaneously, from exactly the same area of sample. This allows the advantages of both techniques to be combined, to potentially track the mechanical properties of a structure whose location is known due to the specificity of fluorescence imaging - an application which cannot be performed

when these techniques are carried out consecutively. More fundamentally however, the requirement to obtain data over a large area with one of the techniques (to always ensure that the feature of interest is within both images) is eradicated by first aligning the AFM-tip with the excitation beam. This saves time and reduces the amount of data required for correlative microscopy.

## 5.7 SUPPLEMENTARY INFORMATION

A version of the manual alignment program, along with instructions for use, can be found online at:

<https://github.com/AMoores/MATLAB-galvanometer>

## REFERENCES

- <sup>40</sup>A. E. X. Brown, A. Hategan, D. Safer, Y. E. Goldman and D. E. Discher, 'Cross-correlated TIRF/AFM reveals asymmetric distribution of force-generating heads along self-assembled, "synthetic" myosin filaments', *Biophysical Journal* **96**, 1952–1960 (2009).
- <sup>134</sup>J. V. Chacko, F. C. Zanicchi and A. Diaspro, 'Probing cytoskeletal structures by coupling optical superresolution and AFM techniques for a correlative approach', *Cytoskeleton* **70**, 729–740 (2013).
- <sup>135</sup>G. Maubach and W. Fritzsche, 'Precise positioning of individual DNA structures in electrode gaps by self-organization onto guiding microstructures', *Nano Letters* **4**, 607–611 (2004).
- <sup>136</sup>J. Doke, 'Ginputc', version 1.0.0.1, <https://uk.mathworks.com/matlabcentral/fileexchange> (2012).
- <sup>137</sup>J. K. Hobbs, T. J. McMaster, M. J. Miles and P. J. Barham, 'Direct observations of the growth of spherulites of poly(hydroxybutyrate-co-valerate) using atomic force microscopy', *Polymer* **39**, 2437–2446 (1998).
- <sup>138</sup>Y. Xie, Y. Li, L. Xiao, Q. Qiao, R. Dhakal, Z. Zhang, Q. Gong, D. Galipeau and X. Yan, 'Femtosecond Time-Resolved Fluorescence Study of P<sub>3</sub>HT / PCBM Blend Films', *Journal of Physical Chemistry*, 14590–14600 (2010).
- <sup>139</sup>M. Li, P. Xu, J. Yang and S. Yang, 'Donor- p -acceptor double-cable polythiophenes bearing fullerene pendant with tunable donor / acceptor ratio : A facile postpolymerization †', *Journal of Materials Chemistry*, 3953–3960 (2010).

<sup>140</sup>M. L. Petrus, R. K. M. Bouwer, U. Lafont and D. H. K. Murthy,  
'Polymer Chemistry optoelectronic properties', Polymer Chemistry,  
4182–4191 (2013).

# 6

---

## A FULLY-AUTOMATED CORRELATION PROGRAM TO FACILITATE MICROSCOPE ALIGNMENT AND CORRECT FOR DRIFT

---

### 6.1 INTRODUCTION

In the previous chapter, the development of an alignment program for the tip-enhanced fluorescence microscope was reported. This program correlates features between two images which have been acquired simultaneously on the same instrument: one fluorescence image and one atomic force microscope (AFM) image. By correlating features, the offset in the fields-of-view of both images is calculated, and this information is used to adjust the position of the incident laser beam by controlling a 2D galvanometer placed in the excitation light pathway. Ideally, this program would be fully-automated, running alongside AFM-data acquisition to continuously measure the offset between the two images and adjust the galvanometer accordingly; the objective of this would be to obtain alignment between the excitation laser and the AFM-tip, and then maintain this alignment for the duration of the imaging session. This eliminates the need for the user to be present during long timescale measurements, correcting for drift in the instrument automatically.

In this chapter, a fully-automated program is produced, in which the offset is determined via a cross-correlation measurement. It will be shown that this measurement is not trivial, because it relies upon the two images having similar features. To overcome this issue, an additional processing step is introduced before cross-correlation which aims to pick out key features within the images ready for the cross-correlation measurement.

## 6.2 THEORY

The automated program makes use of two statistical functions: one function prepares the images for the offset measurement by finding the optimum threshold level, creating two one-bit intensity images to define key features; the second function is the offset measurement itself which is performed using a cross-correlation calculation.

### 6.2.1 Otsu Thresholding

Otsu thresholding, invented by Nobuyuki Otsu [141], is a binarisation algorithm which converts a greyscale image to monochrome. The method assumes that each pixel in the image can be classified into one of two groups: one representing the foreground, and one representing the background. The optimum threshold level is found by iterating through all threshold values and measuring the spread of the foreground pixel group and the background pixel group either side of the threshold. When the intra-class variance is minimal (or equivalently the inter-class variance is maximal), the threshold level is deemed to be optimal.

At each particular threshold level, the weight of the foreground  $W_f$  and the background  $W_b$  is calculated; this is the number of pixels which have been determined to be in the foreground group (and the background group) as a fraction of the total number of pixels in the image. Following this, the mean intensity of the foreground ( $\mu_f$ ) and background ( $\mu_b$ ) are calculated for each threshold level. This is the sum of intensities for every pixel in each group, divided by the number of pixels in each group. The two mean values are then used in a variance calculation, whereby the spread of pixel values for both groups is estimated for the particular threshold. Assuming that the foreground or background group contains pixels with differing intensities  $z_i$ , and the number of pixels in the group with particular intensity  $z_i$  is denoted by  $N_i$ , the variance  $\sigma$  for either the foreground or the background group can be calculated:

$$\sigma_{f/b} = \sum_i N_i (z_i - \mu_{f/b})^2 \quad (6.1)$$

where  $i$  is the number of possible intensity values for each group, and  $\mu_{f/b}$  is the mean of the foreground or background group as previously calculated.

The variance and weight can be used for a final calculation of the intra-class variance, denoted as  $\sigma_{WC}$ :

$$\sigma_{WC} = W_b \sigma_b^2 + W_f \sigma_f^2 \quad (6.2)$$

The optimum threshold value is that which gives the minimum intra-class variance  $\sigma_{WC}$ . To find this minimum, all possible threshold values are iterated over.

### 6.2.2 Cross-Correlation

The alignment program utilises a cross-correlation function to determine the most likely position of overlap for two images from the same sample which have different centre points. By simultaneously measuring the height of a sample with an AFM, as well as fluorescence emission from approximately the same area, a cross-correlation measurement can determine the position at which one of these images is located relative to the other.

This process is used in a well-established technique known as *template matching* [142] [143], whereby the position of a sub-image within a larger image is determined. The smaller image (known as a template) is shifted over the larger image (called the search area) and upon each shift, a measure of similarity between the two images is obtained. The position of highest similarity is the position within the search area at which the template is most likely to be located. There are various statistical tests to measure similarity, including the sum of absolute differences, the sum of squared differences, or (as used in this investigation) the correlation-coefficient.

Cross-correlation is a statistical comparison of two functions which ultimately calculates a correlation coefficient value  $R_{g,t}(x, y)$ , where:

$$-1 \leq R_{g,t}(x, y) \leq 1$$

Here,  $R_{g,t}(x, y)$  is the measure of similarity between two images at an offset position  $(x, y)$  [142]. If the coefficient value is 1, the functions are considered to be perfectly correlated to one another. A coefficient value of  $-1$  on the other hand, means perfect anti-correlation. Mathematically, we can define:

$$R_{g,t}(x, y) = \sum_i \sum_j g(i, j) t(i - x, j - y) \quad (6.3)$$

where  $g(i, j)$  is the larger picture in which the sub-image  $t(i, j)$  is found. It is generally agreed that, although cross-correlation is computationally more complex [144], it is more accurate than a sum of absolute differences calculation [143] [145] in template matching applications.

### 6.3 METHOD

The program described in this section is an extension of the MATLAB program outlined in Chapter 5. However, instead of prompting the user for indication points to calculate the offset between the two selected images, the cross-correlation function is deployed on the two images in order to automatically determine the correct offset.

The cross-correlation function is usually applied to images which are identical, but where a smaller image usually lies somewhere within a larger image. Although the cross-correlation measurement may work on some samples, there are inherent differences between the two images being acquired here. Firstly, the images are determined by different parameters (fluorescence and height, adhesion etc.) so, unlike two identical images, it can be expected that they may display different features and at vastly different intensities. As well as this, the fluorescence image is the view of the sample from underneath whereas the AFM image is topographical, which may also lead to differences in the images. In order to define key features, forcing the images to look as similar as possible for the cross-correlation measurement, they are first converted to monochrome using the Otsu algorithm, via a MATLAB function written to perform the calculations described in Section 6.2.1. The outputted binary images are then passed to a cross-correlation function. This function passes one image over the other pixel-by-pixel, and outputs a value between  $-1$  and  $1$  as a measure of how similar the two images are at that particular overlap. If the cross-correlation value is  $1$ , the images are perfectly correlated, whereas a value of  $-1$  indicates perfect anti-correlation. Correlation means that high-intensity pixels for one image are in the same position as high-intensity pixels for the second image, whereas anti-correlation means that high-intensity pixels for one image overlap with low-intensity pixels of the second image. In this program, it is important to look for both types of correlation because it is not always the case that high areas of sample (in the AFM-height image) correspond to bright areas in the fluorescence image (and vice versa). For this reason, the magnitude of the output of this function is taken and the highest value (closest to  $1$ ) in the cross-correlation matrix is taken as the position of most-likely overlap between the two images. Using data on the scan-size and the number of pixels in each image, a conversion factor between the offset in pixels and an offset in microns is calculated. This value is then input to the same functions as in Chapter 5 in order to calculate the voltages required by the galvanometer to move the im-

ages towards zero offset, achieving alignment between the excitation laser and the AFM-tip.

As before, this automated program is designed to run alongside AFM data-acquisition, calculating the offset whenever new data is captured by the AFM, acting to continually adjust the incident position of the excitation laser throughout the duration of the imaging session.

## 6.4 RESULTS

### 6.4.1 *Initial Testing of the Automated Program*

As in Chapter 5, a sample of poly(hydroxybutyrate-co-valerate) (PHBV) spherulites on a thin piece of cover-glass was used to test the long-term stability of the automated program. This sample is non-fluorescent, but was chosen to test the program's ability to maintain alignment over long durations of time (where photobleaching may otherwise become a problem). The optical set-up remains the same as in Figure 4.1, with the multi-mode optical fibre being utilised for the results seen in this chapter; this allows detection of fluorescence over a larger area, eliminating the requirement to continuously realign the excitation and collection pathways after every iteration of the program. The only change in the set-up was that the 570 nm longpass filter was removed from the front of the single photon counting module (SPCM) and the power of the excitation beam was reduced to 100 nW to prevent damage to the SPCM. Instead of detecting fluorescence, the microscope was detecting scatter of the 532 nm wavelength laser at the sample in order to produce an image. Although the 561 nm longpass dichroic blocks most of the scattered 532 nm light, enough photons are transmitted to the single photon detector, allowing an image to be formed despite the presence of the dichroic.

The program calculated the offset between an AFM-height image and a light-scatter image of the sample for every image frame, whilst continually adjusting the position of the incident laser by applying differing voltages to the galvanometer. The resulting x-offset, y-offset and the offset magnitude between the two images are shown in Figure 6.1. An initial calculated offset of  $(7.2 \pm 1.1)$  microns and  $(10.0 \pm 1.2)$  microns in the x- and y-directions respectively was reduced by the fifth imaging frame to  $(0.5 \pm 1.2)$  microns in magnitude. Because a large initial offset was chosen, the excitation and collection pathways needed to be realigned after acquiring the first frame and readjusting the galvanometer for the first time, before acquiring the second frame. It can be seen that the offset was then maintained at approximately the same

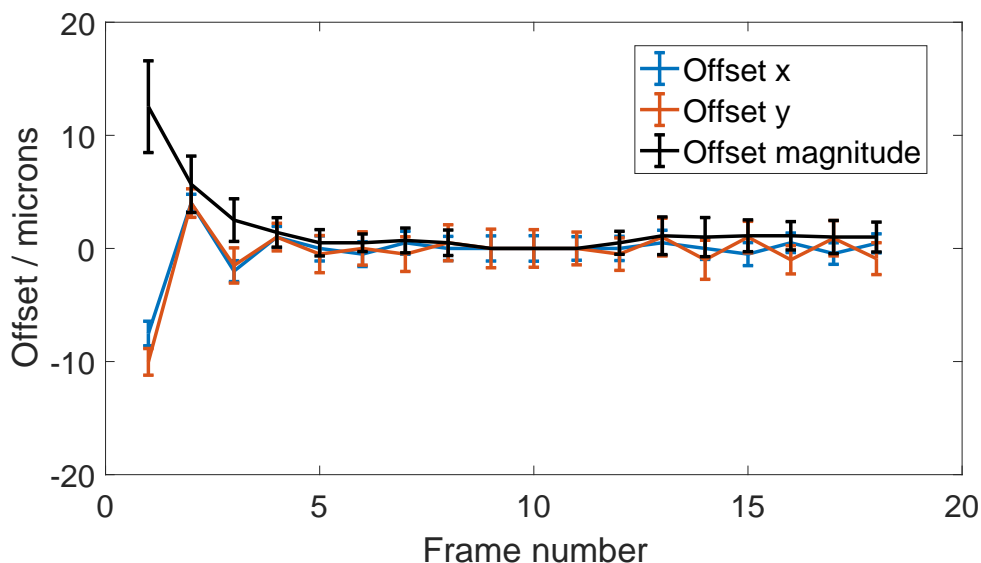


Figure 6.1.: Offset-tracking graph output by the automated MATLAB program. The program has calculated the x-offset (blue), y-offset (red) and the magnitude (black) of the offset between an AFM-height image and a light-scatter image of PHB-V spherulites, and then adjusted the galvanometer accordingly after each imaging frame. An offset to within one micron has been calculated from an initial offset of  $(12.3 \pm 1.6)$  microns in magnitude after just four imaging frames. This offset is maintained for a further 14 imaging frames.

magnitude for the remainder of the imaging session (three hours), meaning that the program can automatically correct for any drift in the offset position. This indicates that the automated version of the program works as efficiently as the manual version outlined in the previous chapter. Having this automated version of the alignment program is more desirable because it eliminates the need for user-input to determine the offset between the two images. This will be particularly useful if this method is to be used for alignment in tip-enhanced fluorescence imaging applications, providing a tool which can correct for drift over long timescale measurements.

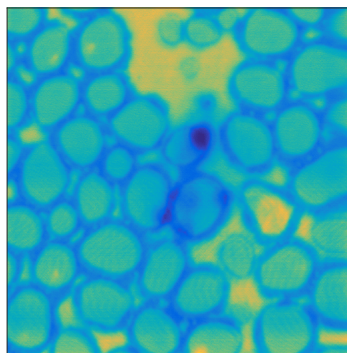
#### 6.4.2 *Reproducing Results for Differing Samples*

To test the magnitude of offset changes which could be achieved by the program, and to confirm that results could be reproduced on a different sample, the Otsu thresholding and cross-correlation functions were trialled on a sample of phase-separated P<sub>3</sub>HT-polystyrene polymer blend. However, it was found that the automated cross-correlation

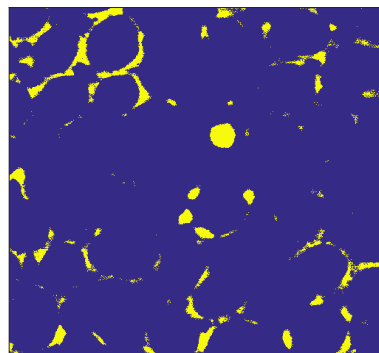
program sporadically fitted the AFM-height image and the fluorescence image at an incorrect offset when the Otsu thresholding method was deployed. One example of this can be seen in Figure 6.2. These images have been incorrectly overlaid due to the thresholded versions looking very different from each other (see Figures 6.2b and 6.2d). It can be seen that, by comparing the raw images in Figures 6.2a and 6.2c, areas of large height do not necessarily correspond to areas of great brightness (or even the opposite) on the fluorescence image. It is therefore very difficult to threshold images of this type into binary images, and probably more than two conditional groups will be required to classify every pixel in these images. The assumptions made in the Otsu function do not apply here, and so, this method cannot be used for this particular sample.

To solve this problem, a different image segmentation technique based upon edge detection was used on the fluorescence and AFM-height images of the P<sub>3</sub>HT sample (Figure 6.3). The chosen method for edge detection was the Canny method. This edge detection algorithm was used on the two raw images, before using a dilation function to remove small gaps in the detected edges. Following this, the edges were filled on both of the edge detection images. Results of this process are shown in Figures 6.3a-d. It can be seen that this processing method has produced binary fluorescence and height images which are much more similar to each other; in general, the same key features in both have been automatically selected. These binary images were passed to the automated cross-correlation program, which subsequently determined the correct offset position for the phase-separated P<sub>3</sub>HT sample. An overlay of the fluorescence and height image at the correct position can be seen in Figure 6.3e.

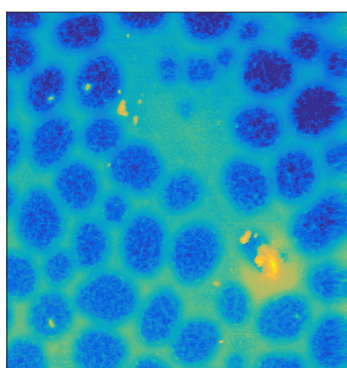
It should be noted that this edge-detection method was subsequently trialled on the images of PHB-V spherulites that were used to obtain the results earlier in this chapter. For these images, where the automated Otsu method proved successful, the edge-detection method failed to produce binary fluorescence and AFM-height images which worked with the automated cross-correlation function. This indicates that there is probably no single imaging-processing solution which optimises images for the cross-correlation measurement that suits all sample-types. However, if the same sample is being investigated every time, there will be an algorithm which suits the particular sample, and which can then be used in conjunction with the automated version of the alignment program.



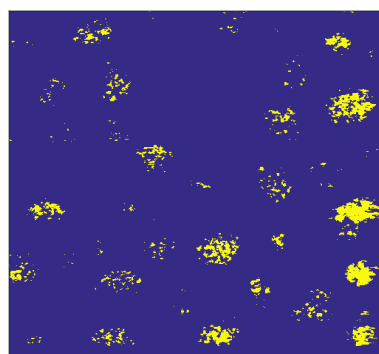
(a)



(b)

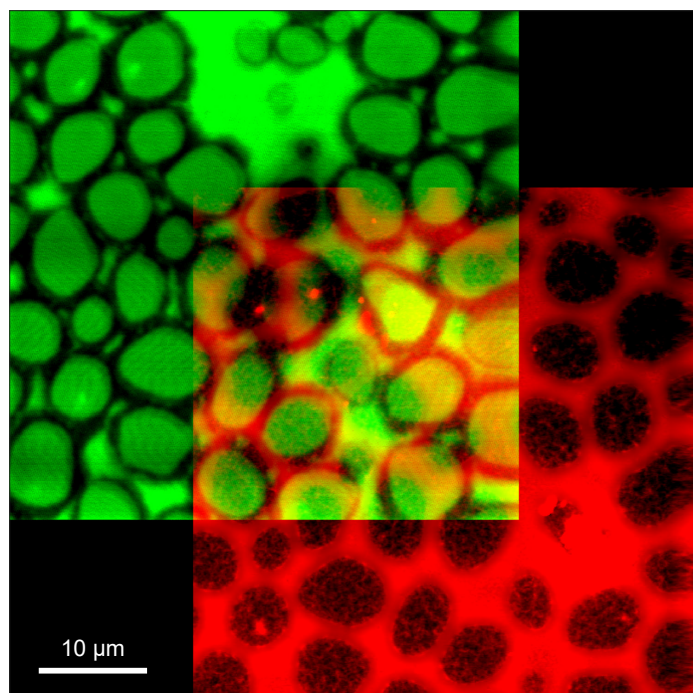


(c)



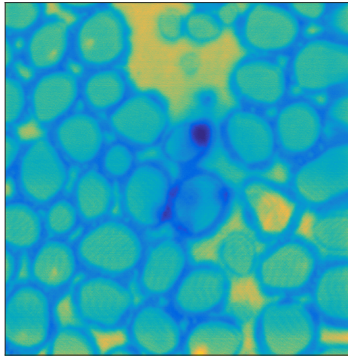
(d)

Figure 6.2.: Images obtained by automated Otsu thresholding and cross-correlation for the phase-separated P3HT sample. Fluorescence image (a) has been passed through Otsu function, which has determined the optimum threshold position to be 20% of the maximum intensity, to achieve binary image (b). Otsu function has determined the optimum threshold position of the AFM-height image (c) to be 8% of the maximum intensity: the corresponding binary image is seen in (d). These thresholded images were passed to the automated cross-correlation program, which has calculated the most likely offset between the two images and produced the corresponding overlay (e). It can be seen that the program has failed to determine the correct position.

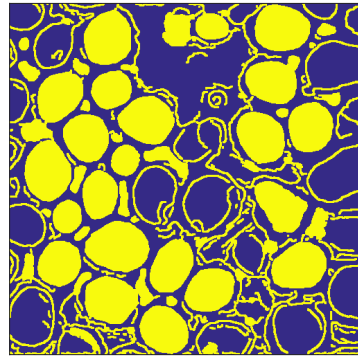


(e)

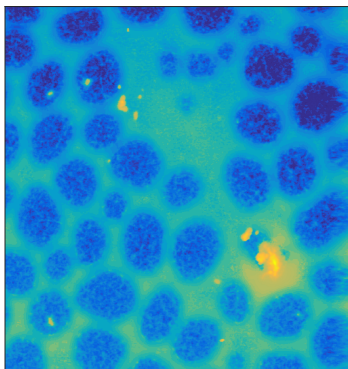
Figure 6.2.: (continued) Images obtained by automated Otsu thresholding and cross-correlation for the phase-separated P3HT sample. Fluorescence image (a) has been passed through Otsu function, which has determined the optimum threshold position to be 20% of the maximum intensity, to achieve binary image (b). Otsu function has determined the optimum threshold position of the AFM-height image (c) to be 8% of the maximum intensity: the corresponding binary image is seen in (d). These thresholded images were passed to the automated cross-correlation program, which has calculated the most likely offset between the two images and produced the corresponding overlay (e), where the fluorescence and AFM-height images are displayed in green and red respectively. It can be seen that the program has failed to determine the correct position.



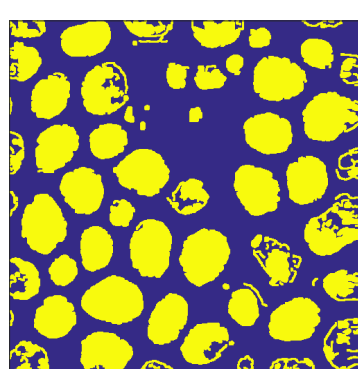
(a)



(b)

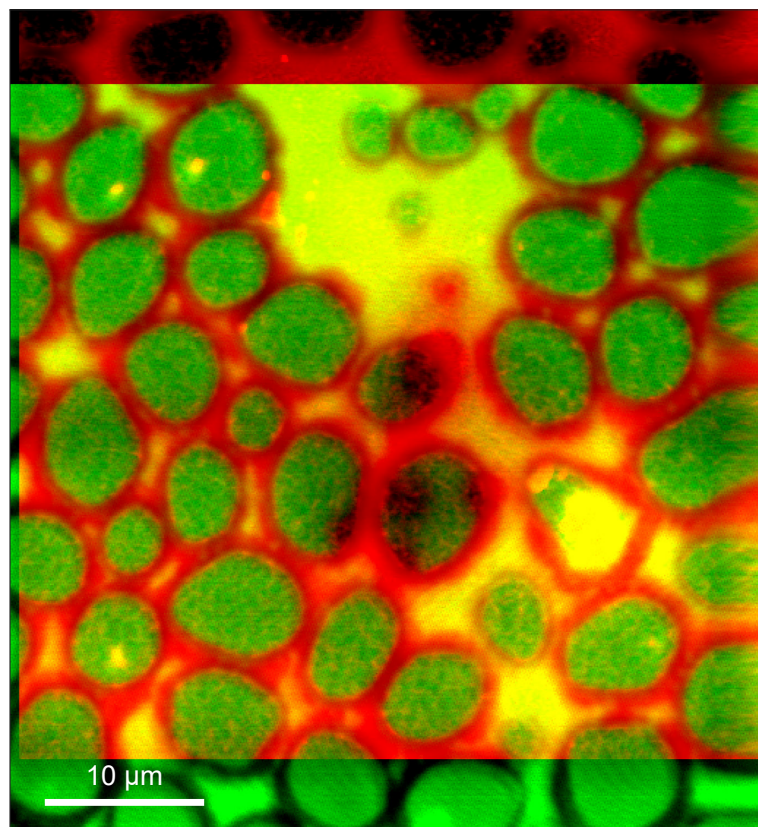


(c)



(d)

Figure 6.3.: Images obtained by edge detection and automated cross-correlation for the phase-separated P3HT sample. A combination of edge detection, dilation and hole-filling algorithms have been used on the fluorescence image (a) to obtain the corresponding binary image (b). The same process has been used on the AFM-height image (c) to obtain (d). These thresholded images were passed to the automated cross-correlation program, which has calculated the most likely offset between the two images and produced the corresponding overlay (e), where the fluorescence and AFM-height images are displayed in green and red respectively. It can be seen that the program has correctly determined the offset position.



(e)

Figure 6.3.: (continued) Images obtained by edge detection and automated cross-correlation for the phase-separated P3HT sample. A combination of edge detection, dilation and hole-filling algorithms have been used on the fluorescence image (a) to obtain the corresponding binary image (b). The same process has been used on the AFM-height image (c) to obtain (d). These thresholded images were passed to the automated cross-correlation program, which has calculated the most likely offset between the two images and produced the corresponding overlay (e), where the fluorescence and AFM-height images are displayed in green and red respectively. It can be seen that the program has correctly determined the offset position.

## 6.5 DISCUSSION

This chapter has outlined the work performed towards an automated program which has the same purpose as that developed in Chapter 5: to obtain and then maintain alignment between the incident laser beam and the AFM-tip by correlating fluorescence and AFM images. The automated program developed here is based upon an image registration technique known as cross-correlation, and has been implemented into a MATLAB function. It has been shown that the program works well on some samples, but fails with others.

The cross-correlation technique is usually performed on images which are identical, but where a small subset within an original image needs to be found. This means that cross-correlation works best on images which are identical: i.e., the key features in the images and intensities of these features are broadly the same. This is practically impossible to achieve using the fluorescence and AFM-height images to which the function is being applied here. Therefore, the program also makes use of image processing techniques to force the two images to look as similar as possible before the cross-correlation measurement is performed. The image processing performed includes applying two filters, one to remove any DC-changes in intensity between rows of the image, and another to remove any slow-changing gradients across the image which are characteristic of many AFM-images. Following this, a threshold is then applied to the normalised images in order to transform them into binary images. This is the most important step in the image-processing because it picks-out key features in the two images.

In order to achieve a fully-automated program as the final result, an Otsu-thresholding algorithm was implemented into MATLAB. This function uses statistics in order to determine where the optimum thresholding position is, based upon the assumption that any image can be split into two sections: a foreground and a background.

The ability of the automated program to obtain and then maintain alignment over a long period of time was tested using a sample of PHB-V spherulites, as in Chapter 5. This sample is non-fluorescent so can be imaged for an extended period of time without the issues caused by photobleaching. It was shown that the automated program can reduce the offset between two simultaneously-acquired images from  $(12.5 \pm 4.1)$  microns to  $(0.5 \pm 1.2)$  microns within four iterations of the galvanometer orientation. Like the manual program, this offset is broadly maintained for the remainder of the imaging session, with the largest offset achieved in subsequent acquisitions being  $(1.1 \pm 1.4)$  microns in frame 15. The uncertainties calculated in the offset val-

ues are large, but they are conservative estimates: the uncertainty is estimated by assuming that the hotspot in the cross-correlation matrix (output by the MATLAB function) is Gaussian in nature, and then calculating the full width at half maximum (FWHM) of this hotspot.

Following the imaging of the spherulites sample, the program was tested on fluorescent samples. A variety of samples were trialled, including the phase-separated poly(3-hexylthiophene-2,5-diyl) (P3HT)-polystyrene polymer blend. The ability of the program to determine the correct offset was variable, with unsuccessful calculations obtained for the P3HT sample in particular. It is proposed that, rather than being a problem with the cross-correlation function, the issue in determining the offset lies within the ability of the Otsu-threshold function to pick out the same key features in both images. The reason for this function not working correctly is that the P3HT samples cannot be differentiated into two distinct areas: one of the main assumptions of Otsu-thresholding. Because the thresholded images do not look similar, the cross-correlation function cannot determine the correct offset.

For these samples however, a different image-processing method did prove successful. For this alternative method, edge detection functions were used on the two images and the spaces contained by the edges were filled. This technique identified more key features than the Otsu function and produced binary fluorescence and AFM images which looked more similar for the P3HT sample. These processed images were input to the automated cross-correlation program, and the correct offset between the fields-of-view of both images was subsequently found. This edge detection method did not work for the PHB-V spherulites, which indicates that optimising images for the cross-correlation measurement is almost certainly not a "one solution fits all" scenario, with an image-processing technique probably needing to be tailor-made to the sample in question. If this instrument is to be used to always image the same type of sample, it could be worth spending additional resources to optimise an image processing algorithm for the cross-correlation measurement which is specific to the sample. Alternatively, a semi-automated version of the alignment program could be developed which first outputs the results of multiple image-processing techniques and asks the user to select the one which has provided the best result. The optimum image processing method could then be used for the remainder of the galvanometer iterations, eliminating the need for user-input during the remaining image frames.

Aside from aligning the instrument here, if the cross-correlation measurement can be optimised for specific samples, it could have ap-

plications in the more general field of correlative microscopy. With correlative microscopy, techniques are usually performed consecutively on multiple instruments, and then the images are overlaid at their correct offsets manually as a post-processing task. Having an algorithm which can perform this function automatically would be highly attractive, particularly for users with large data sets.

Another adaptation of the alignment program developed here could be to have the automated cross-correlation program operate on smaller subsets of the two images, rather than with the two whole images. This option could be particularly useful with samples which already contain fiducial markers (such as fluorescent beads) alongside the fluorescent material of interest. The areas in each image containing the fiducial markers could be selected and cross-correlation could be performed on these sub-sections only. Knowing the location of the subsets within the whole image would then allow the offset for the whole field-of-view to be determined. This would remove the requirement to have both whole images looking as similar as possible before the cross-correlation measurement can take place, and will be a more attractive option for fluorescent labelling of structures which are more sparsely distributed throughout the sample (e.g., the cell nucleus).

## 6.6 CONCLUSION

This chapter has outlined a fully-automated version of the program developed in Chapter 5: a program that will obtain and maintain alignment between an AFM-tip and a fluorescence excitation laser for tip-enhancement purposes or simultaneous correlative imaging.

The method created here utilises a cross-correlation calculation as a measurement of similarity between the two images. To combat the need for the images to look similar for cross-correlation, two image processing solutions have been developed which pick out key features and binarise the images. An automated thresholding program has been developed (based on the Otsu algorithm), which finds the optimum threshold to convert the images to a binary scale. Alongside this, a binarisation algorithm based on edge detection has also been used. It was found that the optimum method for preparing the images for the cross-correlation measurement varied greatly depending on the sample-type.

If the correct image processing method is chosen (such as the Otsu program working on the PHB-V spherulites sample), the automated program has been as successful as the program outlined in Chapter 5, obtaining alignment within just a few iterations of the galvanometer

and maintaining the alignment for several hours. Finding a universal processing method for optimising the images for cross-correlation will not be a trivial task. However, if this instrument is to always be used with the same sample-type, the automated version of the program is a viable option because a sample-specific image segmentation algorithm could be found. There is also scope to use elements of this program as a standalone overlaying algorithm for general correlative microscopy, enabling the correct offset between two different images to automatically be determined: a prospect which is particularly attractive for those with large datasets.

#### 6.7 SUPPLEMENTARY INFORMATION

A version of the automated alignment program, along with instructions for use, can be found online at:

<https://github.com/AMoores/MATLAB-galvanometer>

#### REFERENCES

- <sup>141</sup>N. Otsu, 'A threshold selection method from gray-level histograms', *IEEE Transactions on Systems, Man, and Cybernetics* **9**, 62–66 (1979).
- <sup>142</sup>R. O. Duda, *Pattern classification and scene analysis*, edited by P. E. Hart and P. E. Hart (New York Chichester : Wiley-Interscience, 1973, New York Chichester, 1973).
- <sup>143</sup>A. Goshtasby, S. H. Gage and J. F. Bartholic, 'A Two-Stage Cross Correlation Approach to Template Matching', *IEEE Transactions on Pattern Analysis and Machine Intelligence* **PAMI-6**, 374–378 (1984).
- <sup>144</sup>D. I. Barnea and H. F. Silverman, 'A Class of Algorithms for Fast Digital Image Registration', *IEEE Transactions on Computers* **C-21**, 179–186 (1972).
- <sup>145</sup>S. D. Wei and S. H. Lai, 'Fast Template Matching Based on Normalized Cross Correlation With Adaptive Multilevel Winner Update', *IEEE Transactions on Image Processing* **17**, 2227–2235 (2008).



---

## TIP-ENHANCED FLUORESCENCE: A NOVEL METHOD FOR DETECTING TIP-ENHANCEMENT

---

### 7.1 INTRODUCTION

The previous chapters have outlined the hardware aspects of building a tip-enhanced fluorescence microscope, with a great amount of time being spent on developing a method for repeatedly and reliably aligning the incident excitation beam with an atomic force microscope (AFM)-tip in order to induce the tip-enhancement effect. It is known that the enhancement effect operates over an extremely small area, confined to the apex of the tip. This can make detection of the enhancement effect difficult, particularly for biological samples in which dense numbers of fluorescence molecules are present, leading to a high background signal.

The method proposed in this thesis for the detection of fluorescence enhancement exploits the high-speed programming capabilities of field programmable gate array (FPGA) computing. The theory behind FPGA hardware and its operation was outlined in Chapter 3. The method developed here correlates the phase of tip-oscillation to the number of photons being detected at that particular time, and utilises knowledge that the enhancement effect (and therefore the number of emitted photons) is greatest when the tip is within 10 nm of a fluorophore [42–46].

### 7.2 THEORY

Assuming that the tip-enhanced fluorescence microscope has been aligned correctly, Figure 7.1 shows the theoretical output signal from the single photon counting module (SPCM) in relation to the tip-sample separation at that particular time. It is known that the enhancement effect only occurs when the tip is within approximately 5 nm to 10 nm of the fluorescing molecule [42–44]. Beyond this separation, the fluor-

## TIP-ENHANCED FLUORESCENCE

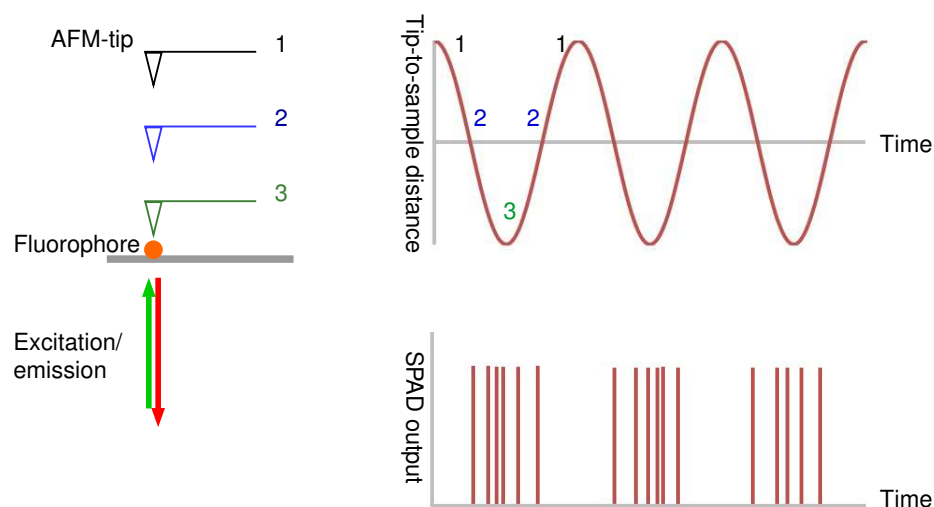


Figure 7.1.: Predicted observations for tip-enhanced fluorescence. AFM is operated in tapping-mode to force the tip to oscillate in the  $z$ -direction, varying the tip-to-sample distance over time. Because the enhancement effect occurs when the tip is within 10 nm of the fluorophore, photons will be detected at an increased rate when tip is on closest approach to sample. Over several tip-oscillations, enhancement will manifest itself as a repeated pattern in the SPCM output as pictured. Should no fluorophore be present within the vicinity of the tip, photons will be detected sporadically at a random rate, producing no visible pattern.

escence lifetimes are unaffected by the presence of the tip. Therefore, as the tip oscillates above the sample, it is expected that the rate of detection of fluorescence photons will increase when the tip approaches the sample and then reduce again as the tip retracts. This effect would manifest as a pattern in the output voltage of the SPCM similar to that shown in Figure 7.1. Should there be no fluorescing molecule within 10 nm of the tip at that time, photons will be detected at a random rate as normal and no particular pattern will emerge in the SPCM output.

By producing a histogram of detected photons as a function of the phase of tip-oscillation (see Figure 7.2), the pattern in the SPCM output should be detectable. By integrating over many oscillation cycles, it should be that the increase in counts should occur only over a particular range of oscillation phases. Finding this pattern in the histogram (or lack of a pattern) indicates whether or not there is a fluorophore present underneath the tip at that particular time. All locations at

which a fluorophore is present can be stored, allowing a fluorescence image to be reconstructed which has atomic force resolution.

Detecting this pattern and correlating it to the AFM-tip z-position in real-time is the difficult aspect of this technique, since the frequency of oscillation for the AFM-tip is high. For the histogram to be created over the length of one oscillation cycle of the tip, the photon count will need to be sampled at a rate of at least ten times that of the tapping-frequency (to obtain a histogram with at least ten bins). For this reason, the mode of operation chosen was PeakForce quantitative nanomechanical mapping (QNM) mode because the tapping frequency is much lower than that of tapping mode (1 kHz compared with >100 kHz).

### 7.3 METHOD

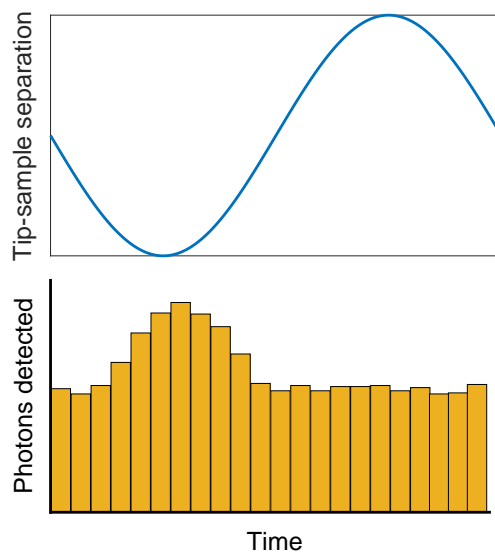
#### 7.3.1 *Creation of Data Acquisition Program*

To detect tip-enhanced fluorescence, a program needed to be written which could simultaneously acquire AFM-tip position data alongside the number of photons detected. FPGA programming provided a suitable solution for this, being able to acquire multiple data sets at differing rates.

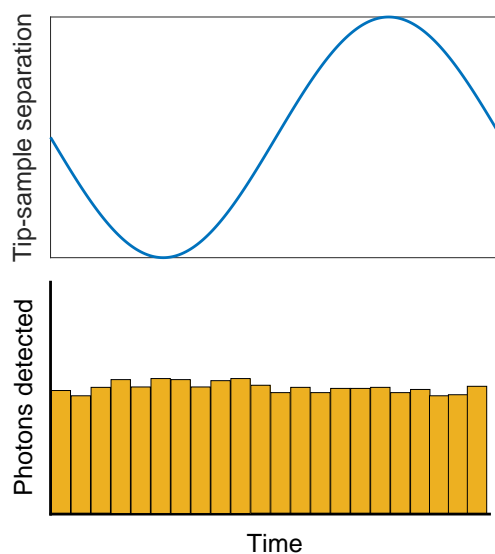
Firstly, a suitable signal needed to be found which corresponded to the AFM-tip position in real time. For this, the z-voltage output on the signal access module box of the AFM was used. For its acquisition, the z-voltage output was connected to the analogue input channel of the NI 5761 within the FPGA, with one data point being read from this channel and written to a 10 000 element first in first out (FIFO) buffer at a rate of 1 MHz. This FIFO buffer was then read as a 10 000 element array by the FPGA host program.

To smooth the signal, the 10000 data points from the FIFO were split into ten smaller arrays of 100 elements, which were then averaged. Figures 7.3 and 7.4 show the effects of smoothing the raw data signal via two averaging methods: the mean and the median. It can be seen in Figure 7.3 that the differences in smoothing method are negligible for cases where high-value noise is not particularly present, and that both methods would sufficiently remove noise from the signal. However, for cases where high-frequency noise spikes of extreme value are present in the raw data (as in Figure 7.4) it can be seen that the median method of smoothing serves as a much better technique than the mean method. This is because outlying extreme values in the 100 element array will have a negligible effect on the median value of the array.

## TIP-ENHANCED FLUORESCENCE



(a)



(b)

Figure 7.2.: Theoretical histograms of detected photons correlated with tip-oscillation, when a fluorophore is present underneath the tip (a), and when no fluorophore is present (b). (a) When the tip is closest to the fluorophore, the rate of detection of photons should increase (i.e., more photons will be detected). (b) When no fluorophore is present, there will be no change in counted photons and the rate of detection will stay broadly the same throughout the whole oscillation cycle. Integration over several oscillations establishes whether a fluorophore is present underneath the tip at that particular time.

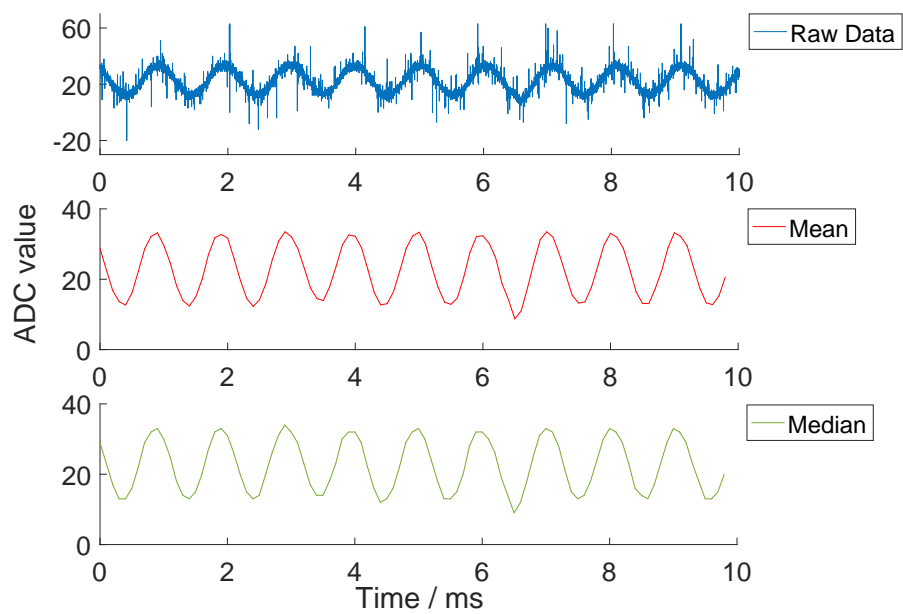


Figure 7.3.: A ten millisecond stream of raw AFM z-data (blue), along with the corresponding smoothed data (red and green). Z-data is in the form of a voltage, read in by the FPGA as an analogue-to-digital conversion (ADC) value. Two methods of smoothing are shown; red and green signals indicate the removal of noise components by taking the mean value and the median value of every 100 raw data-points, respectively.

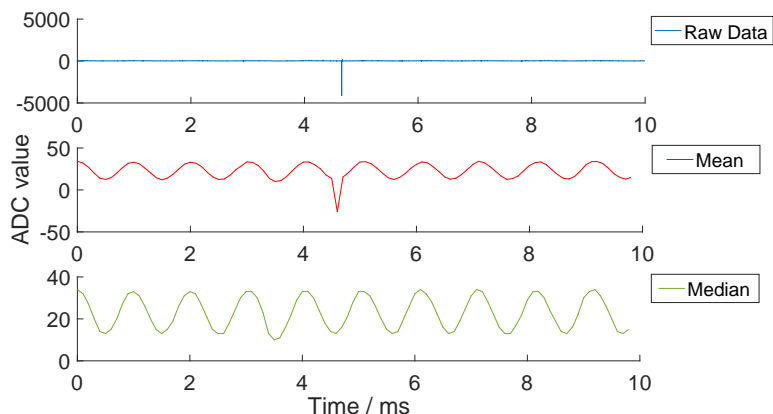


Figure 7.4.: A ten millisecond stream of raw AFM z-data (blue), along with the corresponding smoothed data (red and green). Red and green signals again indicate the removal of noise components by taking the mean value and the median value of every 100 raw data-points, respectively. It can be seen in this case that the presence of extreme ADC values in the raw data has a greater effect on the signal acquired by taking the mean of the raw data, rather than the median value method.

In the LabVIEW host program, the median value of every 100 elements read from the FIFO is stored in an array. Simultaneously, the number of photons that have been detected since the last calculated median value is measured and stored in a second array.

### 7.3.2 Creation of the Histogram

For this proof-of-concept investigation, tip-enhancement is detected following data acquisition, using post-processing analysis.

The higher the AFM z-voltage, the more extended the tip is, i.e. the closer the tip is to the sample. It can therefore be expected that if fluorescence enhancement has occurred, there will be a corresponding increase in the number of photons detected at high ADC values. It follows that fluorescence enhancement could be detected by taking the average number of photons that have been counted for each individual ADC voltage value. Taking the average was found to be a better alternative than summing all photons for each ADC value over every oscillatory period. This is because ADC values do not each occur the same number of times over one oscillatory cycle. If the method of summing over each cycle was chosen, there would be significantly fewer

photons in some ADC bins merely because they occur fewer times. Nevertheless, the occurrence of ADC values will have an effect on the accuracy of enhancement detection, so the uncertainty on each average photon value was also calculated for each bin. This uncertainty is calculated as the standard deviation of photon count values for each ADC bin, divided by  $\sqrt{N}$ , where  $N$  is the number of times the particular ADC value has been recorded within the data stream from the text file.

A histogram (such as that presented in Figure 7.7) is created using a MATLAB program which shows the average number of photons detected for each ADC voltage value. A corresponding error bar is displayed as an area of lighter colour which surrounds each data point, indicating the range of the averaged photon counts. The error depends upon the range of photon values that have been detected for that particular AFM-tip position and also how many times that particular position has been recorded in the data stream.

### 7.3.3 *Development of Customised Coverslips to Aid Alignment*

To help with the detection of fluorescence enhancement for this proof of concept investigation, as much of the sample needs to be covered with fluorescent material as possible. This is because repeated tip-enhanced fluorescence measurements should not be performed on just one position in the sample, as this location will have undergone photobleaching from previous acquisitions. Because the scan size of the AFM is limited to around ( $170 \times 170$ ) microns, achieving a bulk area of fluorescence across the sample would mean that once beam-tip alignment has been achieved, repeated measurements can be made across this whole scan area without needing to withdraw the tip and move to a different sample location. A fluorescent polymer seems like an obvious choice for this purpose. However, spin-coating a fluorescent polymer onto a glass slide leaves an even distribution of fluorescence material with non-distinct features, which is unsuitable for the alignment method outlined in Chapter 5. For this reason, a method was developed to pre-prepare coverslips such that they would have recognisable features on them which are present in both the AFM and fluorescence images. These features can then be used to aid alignment, before experiments to quantify tip-enhancement can be carried out on the other fluorescent material present on the slide.

Photoresist was chosen as a suitable material for the features, because it is inexpensive and widely-used for lithography applications. A pattern of three squares was repeated every  $150 \mu\text{m}$  across the glass

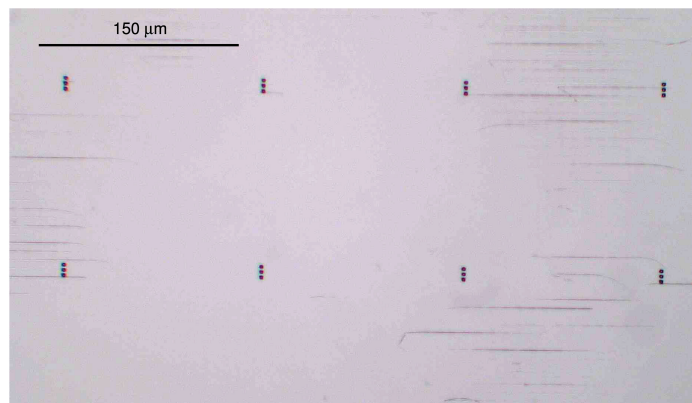
coverslip, in the  $x$ - and  $y$ -directions. This spacing was chosen to ensure that there is at least one set of squares within each AFM scan area with which to aid alignment. The squares had a size of  $2\ \mu\text{m}$ , and were each separated by a  $2\ \mu\text{m}$  interval.

To create the patterned coverslips, the coverslips were first cleaned using a three-stage process. A hotplate was used to heat *n*-Butylacetate, which was subsequently wiped onto the glass coverslip using a cotton bud, removing organic matter from the slide. The *n*-Butylacetate was then removed by submerging the coverslip in acetone for 10 to 30 seconds. The final stage of the clean was to submerge the coverslip into isopropyl alcohol for 10 to 30 seconds to remove any other debris from the slide. The coverslips were then dried with nitrogen and transferred to a hot plate. The coverslips were heated to  $100\ ^\circ\text{C}$  for one minute to remove any remaining moisture from the surface of the coverslip. Photoresist (AZ 1514 H - DNQ Novolac) was then spin-coated onto the coverslip to a thickness of  $1.4\ \mu\text{m}$  to  $1.8\ \mu\text{m}$ . The slides were then heated on a hotplate at  $100\ ^\circ\text{C}$  for one minute to allow to dry. A mask-writer (Heidelberg Instruments  $\mu\text{PG}$  101) was used to expose the photoresist according to a template developed using K-Layout software. A laser power of  $15\ \text{mW}$  was used to expose the areas of the coverslip where the squares were not present, according to the template. Following exposure, the photoresist was developed by submerging the coverslip in AZ developer (0005) for one minute. The developer was then washed off using deionised water and the coverslip was dried with nitrogen. Light microscopy images of the final patterned coverslips can be seen in Figure 7.5.

The photoresist squares are visible in both the optical and AFM images (see Figure 7.6), providing features with which to align the tip-enhanced fluorescence microscope according to the method discussed in Chapter 5.

#### 7.4 RESULTS

To detect fluorescence enhancement, a solution of poly(3-hexylthiophene-2,5-diyl) (P3HT) was developed using the method previously described in Section 4.3.1.  $1\ \mu\text{l}$  of the P3HT solution was pipetted onto the prepared glass slides introduced in the previous section, such that a small amount of fluorescent material was visible in the centre of the glass slide. This sample was mounted onto the stage of the AFM and, using the live-feed images from the USB camera, the boundary between the P3HT area and the clear glass was located. By moving the sample around using the AFM stage, a part of the boundary which

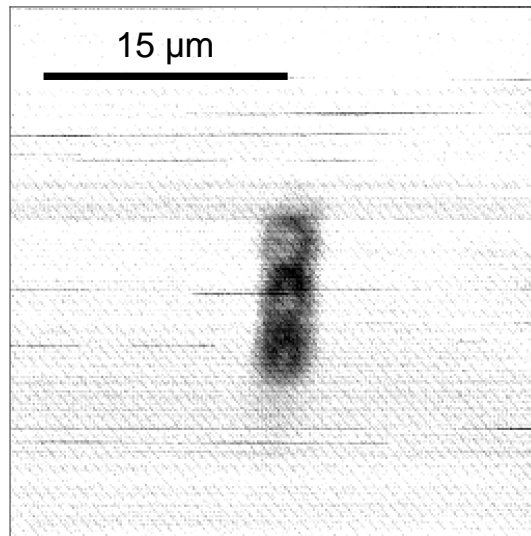


(a)

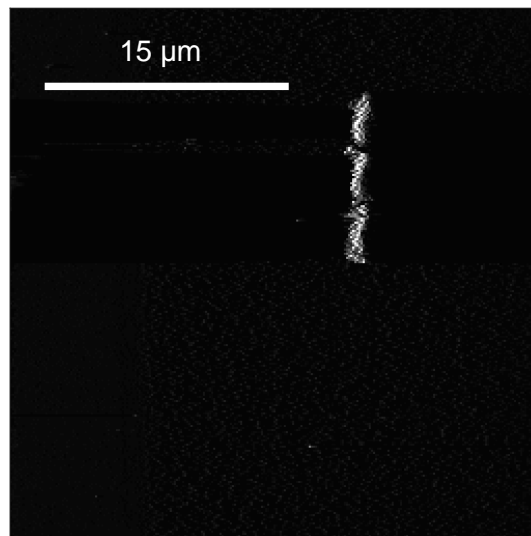


(b)

Figure 7.5.: Light microscopy images of patterned coverslips. Three photoresist squares of diameter  $2\ \mu\text{m}$  are patterned, each spaced  $2\ \mu\text{m}$  apart. The three-square pattern is then repeated across the glass coverslip at intervals of  $150\ \mu\text{m}$ .



(a) Optical image



(b) AFM image

Figure 7.6.: Optical and AFM images of the photoresist squares, obtained simultaneously. Optical image was obtained by removing the  $\lambda = 570 \text{ nm}$  long-pass filter from the collection pathway and detecting scatter of the incident laser beam. AFM image is of the peak force error parameter.

was within approximately 60 microns of three photoresist squares was found and coarsely centred underneath the AFM-tip. The 570 nm long-pass filter was removed from the SPCM pathway and, using the alignment technique introduced in Chapter 5<sup>1</sup>, the AFM-tip was aligned with the incident focussed laser beam by correlating the photoresist squares in the optical scatter image and the AFM image.

When an offset of less than one micron was achieved between the AFM and optical images, the 570 nm long-pass filter was repositioned back into the optical pathway, and the AFM scan area was changed to be centred on an area of P3HT with a scan size of zero microns (AFM stage not scanning). The LabVIEW data acquisition program was run to collect fluorescence photon data from the P3HT sample as the AFM-tip oscillated in the z-direction above the sample. Data was acquired for one minute, before being input to the MATLAB histogram program. For the data acquired in this chapter, gold-coated AFM-tips were used. To produce these, OLTESPA probes (Bruker) were coated with gold using a thermal evaporator.

Figure 7.7 shows typical histograms of photon counts with respect to the phase-oscillation of the AFM-tip, acquired when the AFM-tip is positioned over an area of fluorescent P3HT. The phase of oscillation is defined as  $\pi$  radians being the point where the AFM-tip is closest to the sample; 0 to  $\pi$  radians is where the AFM-tip is approaching the sample, and  $\pi$  to  $2\pi$  radians is the tip retracting. Cases where the AFM-tip has been aligned with the incident excitation laser using the method outlined in Chapter 5, and also when the AFM-tip is misaligned with the beam are shown in Figures 7.7a and 7.7b respectively. The PeakForce amplitude (the total z-distance covered by the AFM-tip) chosen for the data acquired and presented in these figures was 1000 nm, although several amplitudes were trialled from 300 nm to 1000 nm without causing any significant change to the results.

It can be seen on Figure 7.7a that the average number of photons detected varies over the course of one oscillatory cycle of the AFM-tip. As expected from a fluorescence enhancement effect, the number of photons increases when the AFM-tip approaches the sample (0 to  $\pi$  radians), and then reduces again as the AFM-tip retracts ( $\pi$  to  $2\pi$  radians). Also around the point of closest approach on Figure 7.7a, the error bars increase in magnitude: this could be due to a combination of factors. The first is that, because that point is a turning point in the oscillatory cycle, its corresponding AFM z-voltage occurs fewer times over the data taking session than all other AFM z-voltage values. With fewer data points to calculate the average, the uncertainty on

<sup>1</sup> with the multi-mode optical fibre being utilised in the set-up

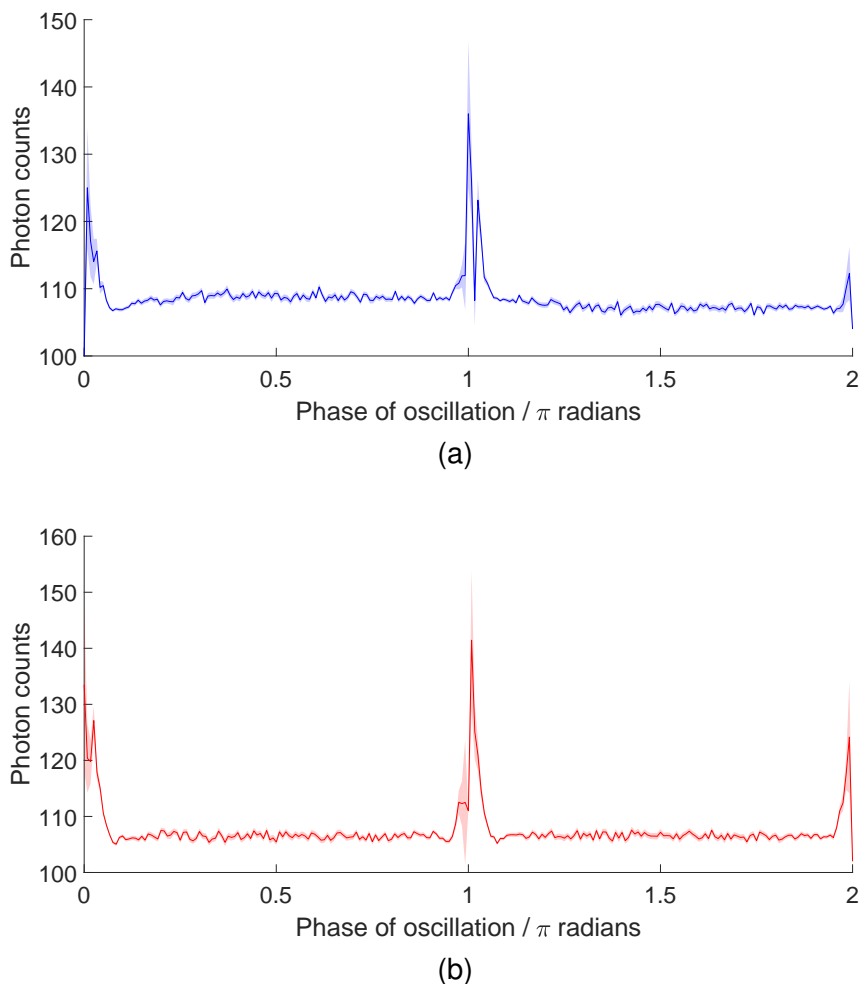


Figure 7.7.: Average number of photons detected with respect to the phase of oscillation of the AFM-tip, whilst the probe was imaging a sample of fluorescent P3HT. (a) Data obtained following alignment of the AFM-tip with the excitation laser via the correlation method outlined in Chapter 5. (b) Data obtained after the AFM-tip was repositioned to be far away ( $\approx 10 \mu\text{m}$ ) from the incident excitation laser. Error in detected photons is shown in light-blue and light-red for tip-alignment and tip-misalignment, respectively.

the average value will be higher. The second factor influencing the error bar magnitude is the standard deviation of the photon count values achieved for that particular AFM-tip position. The larger error bar could be due to a larger standard deviation of values within the same phase bin, which could be due to detection of both fluorescence quenching and fluorescence enhancement when the AFM-tip is at its closest position to the sample.

The increase in the number of detected photons when the AFM-tip is at its furthest point away from the sample cannot be explained by fluorescence enhancement. Moreover, Figure 7.7b shows that the same increase in photon counts can be seen when the AFM-tip is on closest approach to the sample, but when the AFM-tip has been moved far away ( $\approx 10 \mu\text{m}$ ) from the excitation and collection area. For this case, no fluorescence enhancement should be detected because the AFM-tip is no longer aligned with the excitation beam, and light needs to be incident on the tip to induce enhancement. This indicates that the increase has been caused by a factor unrelated to fluorescence enhancement.

## 7.5 DISCUSSION

It has been shown that the number of detected photons does vary as the tip-to-sample separation changes, with a definite increase in photons being detected when the tip is closest to the fluorescent sample. This is a result that has been achieved multiple times through repeated experiments. However, it has been shown that the increase in photons seen as the tip approaches the sample cannot be due to a fluorescence enhancement effect, because the same pattern was seen for the case where the AFM-tip was intentionally misaligned with the incident excitation laser - a condition which should give zero enhancement for the area being imaged with the SPCM.

There is one potential reason for an increase in photons at the point where the AFM-tip is closest to the sample, which would occur regardless of beam-tip alignment. It could be that, as the tip makes contact with the sample, the glass slide is moving around on the AFM stage. Movement of the sample could induce scatter, which could manifest as an increase in photon counts for the bins corresponding to the smallest tip-sample separation. Movement of the sample would usually be restricted through use of a sample clamp, purchased alongside the AFM. However, the use of a home-made sample holder (described in Section 4.2.2) to provide more structural support to thin coverslip glass whilst it is being imaged with the AFM has meant that

the sample clamp does not fit over the samples used for the work in this thesis. One potential fix for this problem would be to use a weak glue to provide more adhesion between the sample and the sample stage whilst the sample is being imaged, or to fabricate a new sample holder.

If the increase in photons is due to sample scatter, the question could be asked as to why the average number of photons was not further increased from this inherent level for the case where the AFM-tip was aligned with the excitation laser. Fluorescence enhancement should have meant that more photons were being detected for the bins representing the smallest tip-sample separations, on top of the additional photons being seen from sample scatter. It could be that the background light is too high for the enhancement effect to be detected. Methods to improve the signal-to-noise ratio could include varying the focussing position of the objective lens. For the data obtained here, the focal position was such that the full width at half maximum (FWHM) of the excitation laser spot was tightest. However, it could be that a focus at a higher position is required for significant enhancement detection, since the AFM-tip is actually located above the slide. Another variable affecting fluorescence enhancement is the emitter itself [49, 50]. Varying both the fluorescent material and the z-focus are therefore suggested areas for future research.

Nevertheless, with regards to the detection method developed here, the results are promising. If the hypothesis is correct (that the increase in detected photons as the AFM-tip makes contact with the sample is due to sample scatter), it means that a data acquisition method has been created which can successfully correlate photon counts from the sample with the position of the AFM-tip. There is no reason why this program would not also detect an increase in the number of photons that has arisen due to fluorescence enhancement.

Another promising outcome of the results from this chapter has been the development and testing of pre-patterned slides to aid alignment between the AFM-tip and the excitation beam using the methods outlined in Chapters 5 and 6. Having distinct structures which are present in both the AFM image and the count image has made alignment using the manual program more user-friendly. Using these pre-prepared glass slides for sample development may also improve the reliability of the automated version of the alignment program, particularly if a modification is made to the program whereby only small subsets of the images are used for the cross-correlation calculation: the small subsets could be the areas containing only the three squares in both images. This would remove the need to find a sample-specific op-

timising algorithm for the images before the cross-correlation methods (as was outlined in Chapter 6).

These patterned squares could be improved however, by using a different material for patterning. The squares are currently made from photoresist which will detach from the glass slide if they come into contact with a solvent. If the squares are to be covered with a fluorescent sample which contains a solvent (as was the case here), a permanent material should be used for patterning the squares. If resources allow, gold or aluminium squares would be suitable for this application. These alternative slides would be produced by first creating a glass slide which is patterned with the inverse of the photoresist squares trialled in this thesis (i.e., a glass slide which is mostly covered in photoresist, but which has small squares of uncoated glass). This slide should then be coated with aluminium or gold before carrying out a lift-off process, whereby the photoresist is stripped from the slide with a solvent (e.g. acetone) to remove all metal which is attached to photoresist. Further to this, adding titanium or nickel to the slide before patterning gold or aluminium will increase adhesion.

In addition to improving the sample preparation and stability, the next stage in the development of the tip-enhancement detection method would be to achieve histograms similar to those that have been presented here, but in real-time using a LabVIEW FPGA. Using an FPGA allows data processing to be performed in parallel to data acquisition, but at a different rate, so the creation of histograms could be added to the same program in which data is currently acquired, without affecting data acquisition.

## 7.6 CONCLUSION

A detection method has been developed which performs post-acquisition analysis to correlate the number of photons emitted by a fluorescent sample with the AFM-tip z-position, with the aim of determining whether fluorescence enhancement has occurred. The method is based upon simultaneous acquisition of photon count data and AFM z-voltage with a LabVIEW FPGA, allowing a histogram of the average photon counts detected to be produced in terms of the AFM-tip position.

It has been shown that the average number of photons detected does vary over the course of one oscillatory cycle of the AFM-tip, with an increase in photon counts being detected for the smallest tip-to-sample separations, as expected from the enhancement effect. However, having also achieved the same result for the case where the AFM-tip has been intentionally misaligned with the excitation beam, it is highly

probable that the results obtained here are due to scatter rather than fluorescence enhancement effects. Nevertheless, if this theory is correct, it means that a method has been developed which can successfully detect changes in the rate of photon detection relative to tip-position, and should be sufficient to detect the fluorescence enhancement effect, should the effect have occurred.

Another promising aspect of the results from this chapter has been the development of patterned glass slides which contain distinctive features (in the form of squares) with which to aid alignment between the fields-of-view of the AFM and fluorescence images. Not only do these squares make alignment easier with the manual version of the alignment program (Chapter 5), but they may also increase the reliability of the automated version (Chapter 6) by only performing cross-correlation on small subsets of the images and eliminating the need to produce sample-specific image processing algorithms.

## REFERENCES

- <sup>42</sup>J. Azoulay, A. Débarre, A. Richard and P. Tchénié, 'Quenching and enhancement of single-molecule fluorescence under metallic and dielectric tips', *Europhysics Letters (EPL)* **51**, 374–380 (2007).
- <sup>43</sup>H. F. Hamann, A. Gallagher and D. J. Nesbitt, 'Near-field fluorescence imaging by localized field enhancement near a sharp probe tip', *Applied Physics Letters* **76**, 1953–1955 (2000).
- <sup>44</sup>S. Kühn, U. Håkanson, L. Rogobete and V. Sandoghdar, 'Enhancement of single-molecule fluorescence using a gold nanoparticle as an optical nanoantenna', *Physical Review Letters* **97**, 1–4 (2006).
- <sup>45</sup>T. J. Yang, G. Lessard and S. R. Quake, 'An apertureless near-field microscope for fluorescence imaging', *Appl. Phys. Lett.* **76**, 378–380 (2000).
- <sup>46</sup>W. Tröbsinger, A. Kramer, M. Kreiter, B. Hecht and U. P. Wild, 'Single-molecule near-field optical energy transfer microscopy', *Applied Physics Letters* **81**, 2118–2120 (2002).
- <sup>49</sup>V. V. Protasenko, A. Gallagher and D. J. Nesbitt, 'Factors that influence confocal apertureless near-field scanning optical microscopy', *Optics Communications* **233**, 45–56 (2004).
- <sup>50</sup>N. Hayazawa, K. Furusawa, A. Taguchi, S. Kawata and H. Abe, 'Tip-enhanced two-photon excited fluorescence microscopy with a silicon tip', *Applied Physics Letters* **94**, 2–4 (2009).

---

## CONCLUSIONS

---

### 8.1 MICROSCOPE STATUS

This thesis has focussed upon the development of a tip-enhanced fluorescence microscope, based upon the addition of optical components to a commercially-available atomic force microscope (AFM) for the achievement of super-resolution fluorescence images. It should be the case that an enhancement effect occurs only when the AFM-tip is within 10 nm of the fluorescent molecule [42–46], and therefore an increase in the number of detected photons will be observed when the tip-sample separation is reduced. This microscope therefore uses a single photon counting module (SPCM) to obtain images, such that individual photons can be detected and subsequently correlated to the z-position of the AFM-tip.

In order to induce enhancement, the AFM-tip first needs to be aligned into the fluorescence excitation and collection light pathway. Not only does this induce the plasmonic effects at the tip-apex through light striking the tip, but it also ensures that the area being enhanced is also the area from which light is being collected. In this thesis, a method has been developed which correlates sample features between an AFM and a fluorescence image which have been taken simultaneously to obtain beam-tip alignment. Because the fluorescence image is determined by the position of the stationary incident laser beam with respect to the sample, and the AFM image is determined by the position of the stationary AFM-tip with respect to the sample, the offset between the fields-of-view across both images is indicative of the distance between the AFM-tip and the incident excitation beam. For the work performed here, a galvanometer was introduced into the optical set-up in order to translate the incident beam the required distance to become aligned with the AFM-tip above the sample.

Although fluorescence enhancement has not been detected with this microscope, a program has been developed which can successfully correlate the number of photons emitted by the sample to the AFM-

## CONCLUSIONS

tip z-position. With the current microscope, an increase in photons can be seen as the AFM-tip makes contact with the sample; it has been shown that this increase is probably due to scatter because it is seen also for the case where the AFM-tip is not aligned with the excitation and collection pathways. In order to obtain super-resolution images using the set-up developed in this thesis, further investigation will be required. Immediate future works should aim to design a sample holder which provides the structural support required for probing a thin piece of coverglass with the AFM-tip, whilst still enabling the AFM sample clamp to securely fasten the sample in place on the stage.

It has been shown throughout this thesis however, that this microscope functions extremely well as an instrument upon which simultaneous fluorescence and AFM imaging is possible. Correlative fluorescence and AFM imaging is a highly attractive technique for use in biological imaging, because it enables force and mechanical measurements to be obtained for particular structures whose location is known due to the specificity of fluorescence imaging. While most correlative imaging techniques are performed consecutively using post-processing correlation methods [40, 134, 135], the ability to perform these two measurements simultaneously is highly valuable, because it allows the mechanical properties of a structure to be tracked over time as changes in the sample occur. The alignment programs that were developed in Chapters 5 and 6 are particularly useful for this application, because the objective of these programs is to align the fields-of-view of both techniques. Even if sample-tracking is not the chosen application however, this instrument could still be beneficial because the alignment programs eliminate the requirement for large areas of the sample to be imaged with one technique, as would usually be the case to ensure that the features of interest are present in both images.

To conclude, the microscope in its current form works well for applications in correlative fluorescence and AFM imaging, providing an instrument upon which these two techniques can be performed simultaneously. Simultaneous imaging is possible due to the alignment methods which have been developed in Chapters 5 and 6, whereby features in the images are correlated to calculate the distance that the incident laser spot needs to be translated to become aligned with the AFM-tip. The alignment program operates alongside AFM data acquisition in order to continuously correct for drift in the hardware, maintaining alignment between the two fields-of-view over the course of the imaging session. The original aim of developing a super-resolution tip-enhanced fluorescence microscope has not yet been realised, but a

method has been developed which successfully correlates the detected photons with the position of the AFM-tip. Although further investigation is needed, this detection method should be sufficient to observe fluorescence enhancement should the effect be successfully induced with the instrument.

## 8.2 FUTURE WORK

The obvious avenue for further work regarding this microscope would be investigations into the enhancement effect. It is not currently known whether or not the microscope has successfully been able to enhance the fluorescence emission, or whether or not the detection method outlined in Chapter 7 is sufficient enough to detect the effect. Immediate future work should aim to develop a method for securing the sample in place at the AFM stage to remove the potential for scatter to occur when the tip makes contact with the sample, because this may obscure enhancement data. Investigations should also be carried out into changing the fluorescent material, and also varying the focal point, to optimise enhancement. As well as this, perhaps an alternative AFM-probe for the experiments can be found. Currently, the probes used for the microscope have a visible tip-apex (Bruker OLTESPA), which was chosen to speed up the initial alignment process as the position of the tip along the cantilever is known. These AFM-probes are coated with gold using a thermal evaporator after purchasing, but it could be that the gold is being removed from the underside of the AFM-tip during the AFM imaging required at the start of the session to obtain alignment. If gold is no longer present on the AFM-tip itself, it could be that the enhancement effect is being significantly reduced. Steps could be taken to deposit a layer of nickel or titanium onto the AFM-probe before gold evaporation to improve wear resistance and ensure that gold is still present on the tip itself for the enhancement experiment.

Additional future work should also take measures to reduce the background light from the fluorescent samples. For the investigation into the detection of the enhancement effect (Chapter 7), bulk fluorescence samples were used. It was thought that this would enable easily repeated investigations once alignment between the AFM-tip and the excitation beam had been achieved. However, these samples may not be the best to use for detection of the enhancement effect. Figure 8.1 shows how the area of the background signal might be affected by the choice of sample. For bulk fluorescent samples containing densely packed fluorophores (left), there will be multiple fluorescent molecules emitting light within the area of the excitation beam. In this case, the

## CONCLUSIONS

area of the background can be approximated by the area of the focussed excitation spot at the sample, given by  $\pi R^2$ , where  $R$  is the radius of the excitation laser spot. Instead, it is suggested that nanolithography samples be created, consisting of lines of fluorescent molecules which are just nanometres in width. For these samples, the area of the background can be approximated as  $2Rw$ , where  $w$  is the width of the protein lines (see Figure 8.1). Because the enhancement effect occurs over such a small area (given by the area of the AFM-tip apex), it is preferable to reduce the background signal such that the areas of enhancement and background are more comparable. Fluorescent line samples would theoretically act to reduce the fluorescence background.

For a more quantitative analysis, Figure 8.2 shows how the ratio between the area of enhancement (approximated as the area of the AFM-tip apex) and the area of the background varies with excitation beam diameter for the two different sample types: bulk fluorescence (blue) and nanolithography (red) samples. The ratio has been calculated using the above equations for the two different background areas, and also by assuming that an AFM-tip with a radius of approximately 10 nm is being used for enhancement. A value of 1 nm has been used for the theoretical width  $w$  of the fluorescent lines. It can be seen that the area of enhancement for the case of the bulk fluorescent sample is on the order of 1000 times smaller than the area of the background signal, which would make the enhancement effect difficult to detect. However, by switching to a nanolithography sample, the ratio between the two areas is much closer to 1, signifying a huge reduction in the background signal: even for the largest beam diameters (which would give the largest background signal), the area over which the enhancement effect occurs is still only about 5 times smaller than the area of the background. This might make the enhancement signal easier to detect. The theoretical results from Figure 8.2 also indicate that changing the sample type will have a much greater effect on the background signal than simply reducing the beam diameter. If the objective lens is switched to one with a higher numerical aperture (NA) value, allowing an excitation beam diameter approaching 400 nm to be achieved, this will still have little effect on reducing the background signal for the case where bulk fluorescent samples continue to be used. It is therefore advised that the effect of fluorophore distribution be investigated further as a measure of reducing the background signal.

If all of these factors are varied, and enhancement is still not detected, this would imply that the method of correlating photon counts to AFM-tip  $z$ -position is not sufficient to observe the enhancement effect.

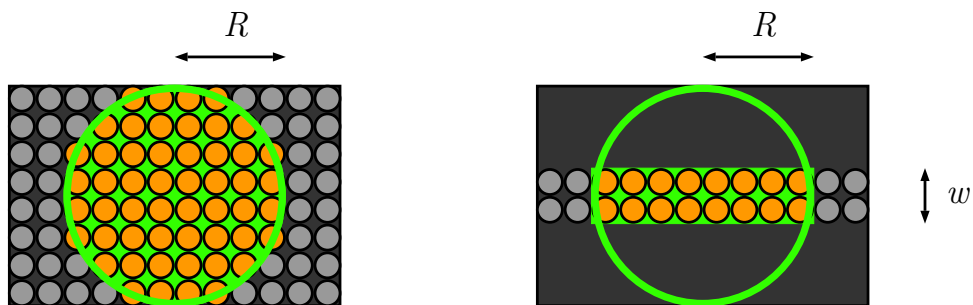


Figure 8.1.: The potential benefits of using nanolithography fluorescent line samples over bulk fluorescence samples for enhancement detection. The theoretical background signals produced by bulk fluorescent samples (left) and fluorescent line samples (right) is given by the area covered by emitting fluorophores. Fluorophores present in the sample are represented by grey circles, with fluorophores which are illuminated by the green excitation beam (and which are therefore emitting light themselves) shown in orange. The area over which the background occurs is proportional to  $R^2$  for the bulk fluorescent samples, and proportional to  $2R$  for the case of the fluorescent line samples, where  $R$  is the radius of the focused excitation beam; nanolithographic fluorescent samples should therefore provide a reduced background signal.

## CONCLUSIONS

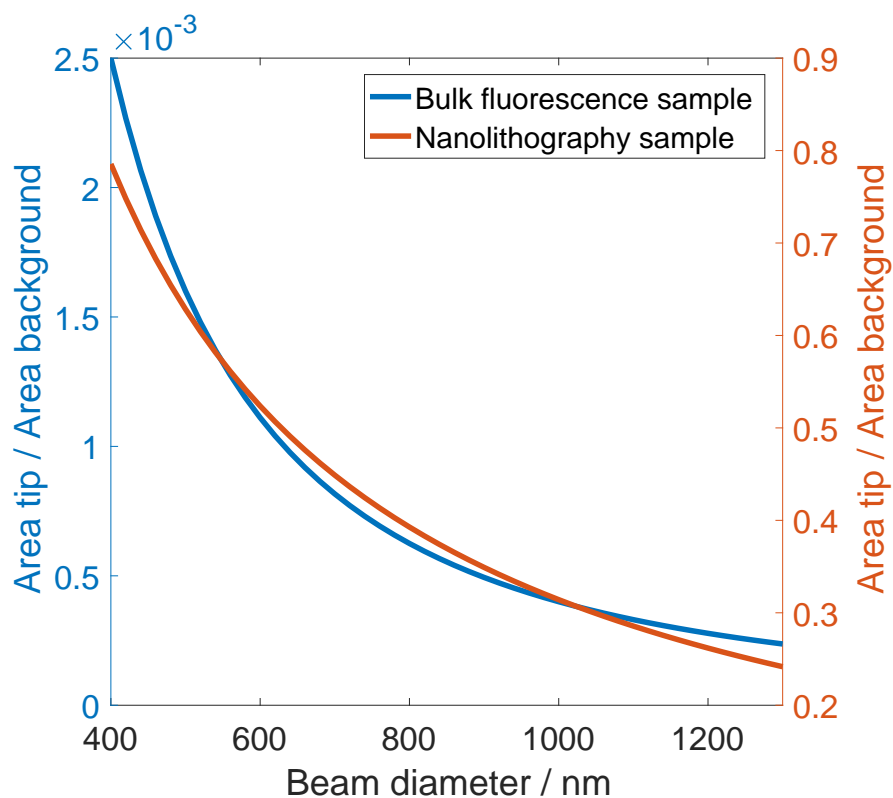


Figure 8.2.: Quantitative analysis of how the ratio between the enhancement area and background area would vary for two sample types, with changing fluorescence excitation beam diameter. Bulk fluorescent sample data and nanolithographic fluorescent sample data are shown in blue and red, respectively. For the case of fluorescent lines produced by nanolithography, the area of enhancement is more comparable to the area of the background, indicating that the enhancement effect might be easier to observe for this sample type.

In such a case, an alternative method for detecting the enhancement effect could be investigated using the instrument developed in this thesis. Because the hardware includes a SPCM to detect individual photons, the optical system could quite easily be modified to instead obtain fluorescence lifetime measurements. All that would be required in this case is for the diode laser used for excitation to be chopped or exchanged for a pulsed laser, and a program to be developed which measures the time between the laser emission and the first detected fluorescence photon from the sample. Fluorescence enhancement is a shortening of the lifetime of a fluorescent molecule, so if a shortening can be measured, it would imply that enhancement has occurred. One advantage of this detection method over the technique being used in this thesis is that scatter can be distinguished from the fluorescence emission process due to the relative timescales over which both processes occur.

Aside from the potential to use this instrument for tip-enhanced fluorescence applications, it has been shown that the set-up has immediate uses in the field of correlative microscopy. There are also several improvements that could be made to the microscope for applications in this area. It was found that, for the work performed in this thesis, the manual version of the alignment program (developed in Chapter 5) was more reliable across a wider range of samples than the automated version of the program (developed in Chapter 6). The automated version of the program extracts both the fluorescence and AFM image from the most recent data file, and passes one whole image over the other, calculating the cross-correlation coefficient for each offset between the two images. This gives a measurement of similarity between the two images to find the most likely offset between the two fields-of-view. This function was found to work sporadically because the fluorescence and AFM images acquired here are not identical.

The reliability of the automated program could be improved by prompting the user to select a small subset of one of the images with which to perform the cross-correlation measurement. This same area could then be detected and used for cross-correlation in subsequent data acquisitions, retaining the benefits of having an automated version of the program. In particular, combining this functionality with samples that have been fabricated onto the pre-patterned glass slides that were developed in Chapter 7 would vastly improve the reliability of this automated program, because there would be well-defined similar structures in both the fluorescence and the AFM image on which to perform the cross-correlation measurement.

## CONCLUSIONS

For those wanting to adapt a commercially-available AFM to enable simultaneous fluorescence imaging, there are potential improvements which could be made to the system. First of all, it would be possible to obtain stimulated emission depletion (STED) imaging on this instrument by overlaying an additional doughnut-shaped beam on top of the current excitation beam, such that a smaller laser spot is used to excite the sample. Previous investigations have seen resolutions of less than 50 nm with STED [36] on biological samples. By aligning an additional pathway for the doughnut beam with the current excitation pathway before the galvanometer, the resolution benefits of STED could be added to the instrument. As well as this, it would not be too difficult to incorporate multicolour imaging into the optical set-up. This could be done by inserting additional excitation pathways for alternative laser wavelengths, and using a removeable dichroic mirror which can be changed to suit the excitation wavelength being used at that particular time. In order to achieve simultaneous multicolour imaging, multiple SPCMs could be incorporated into the collection pathway through the use of beamsplitters and filters, such that each SPCM is detecting the emission of a specific fluorescent probe in the sample.

A sample-scanning AFM has been used for the development of the instrument in this thesis. Using this type of AFM would provide obvious advantages when it comes to the formation of tip-enhanced fluorescence images, because alignment theoretically only needs to be achieved once between the AFM-tip and the incident excitation beam. If a tip-scanning AFM was used instead, it would be exceptionally difficult to develop a method whereby both the incident laser beam and the collection pathway need to follow the AFM-tip during imaging, providing the necessary conditions for enhancement and also detecting the increase in photons. However, it is suggested here that the initial alignment could be made much easier by having a tip-scanning AFM, allowing fine control over the AFM-tip's (x,y) position. It is therefore theorised that the best AFM to use for developing a tip-enhanced fluorescence microscope would be one which possesses both tip-scanning and sample-scanning capabilities: tip-scanning operation to aid alignment between the AFM-tip and the incident excitation beam, and then sample-scanning operation for data acquisition once alignment has been achieved.

## REFERENCES

- <sup>36</sup>B. Hein, K. I. Willig and S. W. Hell, 'Stimulated emission depletion (STED) nanoscopy of a fluorescent protein-labeled organelle inside

- a living cell', *Proceedings of the National Academy of Sciences of the United States of America* **105**, 14271 (2008).
- <sup>40</sup>A. E. X. Brown, A. Hategan, D. Safer, Y. E. Goldman and D. E. Discher, 'Cross-correlated TIRF/AFM reveals asymmetric distribution of force-generating heads along self-assembled, "synthetic" myosin filaments', *Biophysical Journal* **96**, 1952–1960 (2009).
- <sup>42</sup>J. Azoulay, A. Débarre, A. Richard and P. Tchénié, 'Quenching and enhancement of single-molecule fluorescence under metallic and dielectric tips', *Europhysics Letters (EPL)* **51**, 374–380 (2007).
- <sup>43</sup>H. F. Hamann, A. Gallagher and D. J. Nesbitt, 'Near-field fluorescence imaging by localized field enhancement near a sharp probe tip', *Applied Physics Letters* **76**, 1953–1955 (2000).
- <sup>44</sup>S. Kühn, U. Håkanson, L. Rogobete and V. Sandoghdar, 'Enhancement of single-molecule fluorescence using a gold nanoparticle as an optical nanoantenna', *Physical Review Letters* **97**, 1–4 (2006).
- <sup>45</sup>T. J. Yang, G. Lessard and S. R. Quake, 'An apertureless near-field microscope for fluorescence imaging', *Appl. Phys. Lett.* **76**, 378–380 (2000).
- <sup>46</sup>W. Tröbsinger, A. Kramer, M. Kreiter, B. Hecht and U. P. Wild, 'Single-molecule near-field optical energy transfer microscopy', *Applied Physics Letters* **81**, 2118–2120 (2002).
- <sup>134</sup>J. V. Chacko, F. C. Zanicchi and A. Diaspro, 'Probing cytoskeletal structures by coupling optical superresolution and AFM techniques for a correlative approach', *Cytoskeleton* **70**, 729–740 (2013).
- <sup>135</sup>G. Maubach and W. Fritzsche, 'Precise positioning of individual DNA structures in electrode gaps by self-organization onto guiding microstructures', *Nano Letters* **4**, 607–611 (2004).



---

## BIBLIOGRAPHY

---

- <sup>1</sup>L. Rayleigh, 'XXXI. Investigations in optics, with special reference to the spectroscope', *The London, Edinburgh, and Dublin Philosophical Magazine and Journal of Science* **8**, 261–274 (1879).
- <sup>2</sup>F. L. Pedrotti, *Introduction to optics*, edited by L. S. ( S. Pedrotti, 2nd ed. (Englewood Cliffs, N.J. : Prentice Hall, c1993, Englewood Cliffs, N.J., 1993).
- <sup>3</sup>F. Graham-Smith, *Optics*, edited by J. H. ( H. Thomson and J. H. Thomson (London, London, 1971).
- <sup>4</sup>M. Born and E. Wolf, *Principles of optics: electromagnetic theory of propagation, interference and diffraction of light* (Elsevier, 1980).
- <sup>5</sup>G. A. Boutry, R. Auerbach and W. T. Wintringham, 'Instrumental optics', *Physics Today* **15**, 68–70 (1962).
- <sup>6</sup>B. Rossi, *Optics*. (Reading Mass., Reading (Mass.), 1957).
- <sup>7</sup>E. Hecht, *Schaum's outline of theory and problems of optics* (New York, New York, 1975).
- <sup>8</sup>E. Abbe, 'VII.—On the Estimation of Aperture in the Microscope.', *Journal of the Royal Microscopical Society* **1**, 388–423 (1881).
- <sup>9</sup>E. Abbe, 'Beiträge zur Theorie des Mikroskops und der mikroskopischen Wahrnehmung', *Archiv für mikroskopische Anatomie* **9**, 413–418 (1873).
- <sup>10</sup>E. Hecht, 'Optics 4th edition', *Optics, 4th Edition*, Addison Wesley Longman Inc, 1998 (1998).
- <sup>11</sup>K. D. Vernon-Parry, 'Scanning electron microscopy: an introduction', *III-Vs Review* **13**, 40–44 (2000).
- <sup>12</sup>J. C. Meyer, C. O. Girit, M. F. Crommie and A. Zettl, 'Imaging and dynamics of light atoms and molecules on graphene', *Nature* **454**, 319 (2008).
- <sup>13</sup>Now Nanotechnology, 'Hitachi Launches World's Highest Resolution FE-SEM', [http://www.nanotech-now.com/news.cgi?story\\_id=4261](http://www.nanotech-now.com/news.cgi?story_id=4261) (2011).

## Bibliography

- <sup>14</sup>P. D. Nellist, M. F. Chisholm, N. Dellby, O. L. Krivanek, M. F. Murfitt, Z. S. Szilagy, A. R. Lupini, A. Y. Borisevich, J. Sides William H. and S. J. Pennycook, 'Direct Sub-Angstrom Imaging of a Crystal Lattice', *Science* **305** (2004) 10.1126/science.1100965.
- <sup>15</sup>John Innes, 'Electron microscopy', [https://www.jic.ac.uk/microscopy/intro\\_EM.html](https://www.jic.ac.uk/microscopy/intro_EM.html) (2016).
- <sup>16</sup>L. E. C. Van De Leemput and H. Van Kempen, 'Scanning tunnelling microscopy', *Reports on Progress in Physics* **55**, 1165–1240 (1992).
- <sup>17</sup>G. Binnig and F. Quate, 'Atomic Force Microscope', *Physical Review Letters* **56**, 930 (1986).
- <sup>18</sup>G. Schmalz, 'Über Glatte und Ebenheit als physikalisches und physiologisches Problem', *Verein Deutscher Ingenieure*, 1461–1467 (1929).
- <sup>19</sup>T. O. Stadelmann, *Antidot superlattices in InAs-GaSb double heterostructures: transport studies* (University of Oxford, 2006).
- <sup>20</sup>J. Mou, J. Yang and Z. Shao, 'Atomic Force Microscopy of Cholera Toxin B-oligomers Bound to Bilayers of Biologically Relevant Lipids', *Journal of Molecular Biology* **248**, 507–512 (1995).
- <sup>21</sup>D. J. Müller, F. A. Schabert, G. Büldt and A. Engel, 'Imaging purple membranes in aqueous solutions at sub-nanometer resolution by atomic force microscopy.', *Biophysical journal* **68**, 1681–6 (1995).
- <sup>22</sup>T. Walz, P. Tittmann, K. H. Fuchs, D. J. Müller, B. L. Smith, P. Agre, H. Gross and A. Engel, 'Surface Topographies at Subnanometer-resolution Reveal Asymmetry and Sidedness of Aquaporin-1', *Journal of Molecular Biology* **264**, 907–918 (1996).
- <sup>23</sup>D. Fotiadis, L. Hasler, D. J. Müller, H. Stahlberg, J. Kistler and A. Engel, 'Surface Tongue-and-groove Contours on Lens MIP Facilitate Cell-to-cell Adherence', *Journal of Molecular Biology* **300**, 779–789 (2000).
- <sup>24</sup>D. J. Müller and A. Engel, 'Voltage and pH-induced channel closure of porin OmpF visualized by atomic force microscopy', *Journal of molecular biology* **285**, 1347–1351 (1999).
- <sup>25</sup>D. J. Müller, H.-J. Sass, S. A. Müller, G. Büldt and A. Engel, 'Surface structures of native bacteriorhodopsin depend on the molecular packing arrangement in the membrane', *Journal of Molecular Biology* **285**, 1903–1909 (1999).
- <sup>26</sup>F. J. Giessibl, 'Advances in atomic force microscopy', *Reviews of modern physics* **75**, 949 (2003).

- <sup>27</sup>M. J. Rust, X. Zhuang and M. Bates, 'Sub-diffraction-limit imaging by stochastic optical reconstruction microscopy (STORM)', *Nature Methods* **3**, 793–795 (2006).
- <sup>28</sup>M. Heilemann, S. Van De Linde, M. Schüttpelz, R. Kasper, B. Seefeldt, A. Mukherjee, P. Tinnefeld and M. Sauer, 'Subdiffraction-Resolution Fluorescence Imaging with Conventional Fluorescent Probes', *Angewandte Chemie International Edition* **47**, 6172–6176 (2008).
- <sup>29</sup>M. G. L. Gustafsson, 'Surpassing the lateral resolution limit by a factor of two using structured illumination microscopy', *Journal of Microscopy* **198**, 82–87 (2000).
- <sup>30</sup>S. W. Hell et al., *The 2015 super-resolution microscopy roadmap*, 2015.
- <sup>31</sup>M. G. L. Gustafsson, 'Nonlinear structured-illumination microscopy: wide-field fluorescence imaging with theoretically unlimited resolution.', *Proceedings of the National Academy of Sciences of the United States of America* **102**, 13081–13086 (2005).
- <sup>32</sup>E. H. Rego, L. Shao, J. J. Macklin, L. Winoto, G. A. Johansson, N. Kamps-Hughes, M. W. Davidson and M. G. L. Gustafsson, 'Nonlinear structured-illumination microscopy with a photoswitchable protein reveals cellular structures at 50-nm resolution.', *Proceedings of the National Academy of Sciences of the United States of America* **109**, E135–43 (2012).
- <sup>33</sup>E. Rittweger, K. Y. Han, S. E. Irvine, C. Eggeling and S. W. Hell, 'STED microscopy reveals crystal colour centres with nanometric resolution', *Nature Photonics* **3**, 144–147 (2009).
- <sup>34</sup>B. Harke, J. Keller, C. K. Ullal, V. Westphal, A. Schönle and S. W. Hell, 'Resolution scaling in STED microscopy', *Optics express* **16**, 4154 (2008).
- <sup>35</sup>K. I. Willig, R. R. Kellner, R. Medda, B. Hein, S. Jakobs and S. W. Hell, 'Nanoscale resolution in GFP-based microscopy', *Nature Methods* **3**, 721–723 (2006).
- <sup>36</sup>B. Hein, K. I. Willig and S. W. Hell, 'Stimulated emission depletion (STED) nanoscopy of a fluorescent protein-labeled organelle inside a living cell', *Proceedings of the National Academy of Sciences of the United States of America* **105**, 14271 (2008).
- <sup>37</sup>Y. Sako, S. Minoghchi and T. Yanagida, 'Single-molecule imaging of EGFR signalling on the surface of living cells', *Nature Cell Biology* **2**, 168 (2000).
- <sup>38</sup>D. Axelrod, 'Cell-substrate contacts illuminated by total internal reflection fluorescence', *The Journal of cell biology* **89**, 141 (1981).

## Bibliography

- <sup>39</sup>Y. Fu, P. W. Winter, R. Rojas, V. Wang, M. McAuliffe and G. H. Patterson, 'Axial superresolution via multiangle TIRF microscopy with sequential imaging and photobleaching', *Proceedings of the National Academy of Sciences* **113**, 4368–4373 (2016).
- <sup>40</sup>A. E. X. Brown, A. Hategan, D. Safer, Y. E. Goldman and D. E. Discher, 'Cross-correlated TIRF/AFM reveals asymmetric distribution of force-generating heads along self-assembled, "synthetic" myosin filaments', *Biophysical Journal* **96**, 1952–1960 (2009).
- <sup>41</sup>K. Kwakwa, A. Savell, T. Davies, I. Munro, S. Parrinello, M. A. Purbhoo, C. Dunsby, M. A. A. Neil and P. M. W. French, 'easySTORM: a robust, lower-cost approach to localisation and TIRF microscopy', *Journal of Biophotonics* **9**, 948–957 (2016).
- <sup>42</sup>J. Azoulay, A. Débarre, A. Richard and P. Tchério, 'Quenching and enhancement of single-molecule fluorescence under metallic and dielectric tips', *Europhysics Letters (EPL)* **51**, 374–380 (2007).
- <sup>43</sup>H. F. Hamann, A. Gallagher and D. J. Nesbitt, 'Near-field fluorescence imaging by localized field enhancement near a sharp probe tip', *Applied Physics Letters* **76**, 1953–1955 (2000).
- <sup>44</sup>S. Kühn, U. Håkanson, L. Rogobete and V. Sandoghdar, 'Enhancement of single-molecule fluorescence using a gold nanoparticle as an optical nanoantenna', *Physical Review Letters* **97**, 1–4 (2006).
- <sup>45</sup>T. J. Yang, G. Lessard and S. R. Quake, 'An apertureless near-field microscope for fluorescence imaging', *Appl. Phys. Lett.* **76**, 378–380 (2000).
- <sup>46</sup>W. Tröbsinger, A. Kramer, M. Kreiter, B. Hecht and U. P. Wild, 'Single-molecule near-field optical energy transfer microscopy', *Applied Physics Letters* **81**, 2118–2120 (2002).
- <sup>47</sup>V. V. Protasenko, M. Kuno, A. Gallagher and D. J. Nesbitt, 'Fluorescence of single ZnS overcoated CdSe quantum dots studied by apertureless near-field scanning optical microscopy', *Optics Communications* **210**, 11–23 (2002).
- <sup>48</sup>L. Novotny, R. Bian and X. Xie, 'Theory of Nanometric Optical Tweezers', *Physical Review Letters* **79**, 645–648 (1997).
- <sup>49</sup>V. V. Protasenko, A. Gallagher and D. J. Nesbitt, 'Factors that influence confocal apertureless near-field scanning optical microscopy', *Optics Communications* **233**, 45–56 (2004).
- <sup>50</sup>N. Hayazawa, K. Furusawa, A. Taguchi, S. Kawata and H. Abe, 'Tip-enhanced two-photon excited fluorescence microscopy with a silicon tip', *Applied Physics Letters* **94**, 2–4 (2009).

- <sup>51</sup>L. Novotny, 'Single molecule fluorescence in inhomogeneous environments', *Applied Physics Letters* **69**, 3806–3808 (1996).
- <sup>52</sup>W. L. Barnes, 'Fluorescence near interfaces: the role of photonic mode density', *Journal of Modern Optics* **45**, 661–699 (1998).
- <sup>53</sup>D. M. Hercules, 'Fluorescence and phosphorescence analysis: principles and applications', *Fluorescence and Phosphorescence Analysis: Principles and Applications*/Ed. David M. Hercules. New York, NY: Interscience Publishers, c1966. (1966).
- <sup>54</sup>R. R. Chance, A. Prock and R. Silbey, 'Molecular fluorescence and energy transfer near interfaces', *Adv. Chem. Phys* **37**, 65 (1978).
- <sup>55</sup>R. X. Bian, R. C. Dunn, S. Xie and P. T. Leung, 'Single molecule emission characteristics in near-field microscopy', *Physical Review Letters* **75**, 4772–4775 (1995).
- <sup>56</sup>W. P. Ambrose, P. M. Goodwin, J. C. Martin and R. A. Keller, 'Alterations of single molecule fluorescence lifetimes in near-field optical microscopy.', *Science (New York)* **265**, 364–7 (1994).
- <sup>57</sup>C. Girard, O. J. F. Martin and A. Dereux, 'Molecular life time changes induced by nanometer scale optical fields', *Physical Review Letters* **75** (1995).
- <sup>58</sup>M. Thomas, J. J. Greffet, R. Carminati and J. R. Arias-Gonzalez, 'Single-molecule spontaneous emission close to absorbing nanostructures', *Applied Physics Letters* **85**, 3863–3865 (2004).
- <sup>59</sup>J. N. Farahani, D. W. Pohl, H. J. Eisler and B. Hecht, 'Single quantum dot coupled to a scanning optical antenna: A tunable superemitter', *Physical Review Letters* **95** (2005) 10.1103/PhysRevLett.95.017402.
- <sup>60</sup>N. Anderson, A. Bouhelier and L. Novotny, 'Near-field photonics: tip-enhanced microscopy and spectroscopy on the nanoscale', *Journal of Optics A: Pure and Applied Optics* **8**, S227–S233 (2006).
- <sup>61</sup>N. J. D. Mol, M. J. E. Fischer and J. M. Walker, *Surface Plasmon Resonance Methods and Protocols* (Humana Press, 2010).
- <sup>62</sup>M. Fox, *Optical properties of solids* (Oxford, Oxford, 2010).
- <sup>63</sup>A. Eguiluz and J. J. Quinn, 'Hydrodynamic model for surface plasmons in metals and degenerate semiconductors', *Physical Review B* **14**, 1347–1361 (1976).
- <sup>64</sup>L. Novotny, E. J. Sánchez and X. Sunney Xie, 'Near-field optical imaging using metal tips illuminated by higher-order Hermite–Gaussian beams', *Ultramicroscopy* **71**, 21–29 (1998).

## Bibliography

- <sup>65</sup>O. J. F. Martin and C. Girard, 'Controlling and tuning strong optical field gradients at a local probe microscope tip apex', *Appl. Phys. Lett.* **70**, 705–707 (1997).
- <sup>66</sup>L. Aigouy, A. Lahrech, S. Grāsillon, H. Cory, A. C. Boccara and J. C. Rivoal, 'Polarization effects in apertureless scanning near-field optical microscopy: an experimental study', *Optics Letters* **24**, 187–189 (1999).
- <sup>67</sup>R. Reisfeld and V. Levchenko, 'The influence of surface plasmons on fluorescence of the dye Lumogen F red 300 in condensed phase', *Optical Materials* **63**, 88–94 (2017).
- <sup>68</sup>P. Anger, P. Bharadwaj and L. Novotny, 'Enhancement and quenching of single-molecule fluorescence', *Physical Review Letters* **96**, 3–6 (2006).
- <sup>69</sup>B. Palash, A. Pascal and N. Lukas, 'Nanoplasmonic enhancement of single-molecule fluorescence', *Nanotechnology* **18**, 44017 (2007).
- <sup>70</sup>N. S. Abadeer, M. R. Brennan, W. L. Wilson and C. J. Murphy, 'Distance and plasmon wavelength dependent fluorescence of molecules bound to silica-coated gold nanorods', *ACS Nano* **8**, 8392–8406 (2014).
- <sup>71</sup>O. Kulakovich, N. Strelak, A. Yaroshevich, S. Maskevich, S. Gaponenko, I. Nabiev, U. Woggon and M. Artemyev, 'Enhanced Luminescence of CdSe Quantum Dots on Gold Colloids', *Nano Letters* **2**, 1449–1452 (2002).
- <sup>72</sup>G. W. Ford and A. Arbor, 'Electromagnetic Interactions of Molecules With Metal Surfaces With Metal Surfaces', *Physics Reports* **113**, 195–287 (1984).
- <sup>73</sup>S. A. Maier, *Plasmonics: fundamentals and applications* (Springer Science & Business Media, 2007).
- <sup>74</sup>J. Azoulay, A. Débarre, A. Richard and P. Tchénio, 'Field enhancement and apertureless near-field optical spectroscopy of single molecules', *Journal of Microscopy* **194**, 486–490 (1999).
- <sup>75</sup>A. Bouhelier, M. Beversluis, A. Hartschuh and L. Novotny, 'Near-Field Second-Harmonic Generation Induced by Local Field Enhancement', *Physical Review Letters* **90**, 8–11 (2003).
- <sup>76</sup>A. L. Demming, F. Festy and D. Richards, 'Plasmon resonances on metal tips: Understanding tip-enhanced Raman scattering', *Journal of Chemical Physics* **122**, 1–7 (2005).

- <sup>77</sup>N. I Cade, T. Ritman-Meer, K. A Kwaka and D. Richards, 'The plasmonic engineering of metal nanoparticles for enhanced fluorescence and Raman scattering.', *Nanotechnology* **20**, 285201 (2009).
- <sup>78</sup>A. Hartschuh, M. Beversluis, A. Bouhelier and L. Novotny, 'Tip-enhanced optical spectroscopy', *Philosophical Transactions of the Royal Society A* **362**, 807–819 (2004).
- <sup>79</sup>E. H. Synge, 'III. A microscopic method', *The London, Edinburgh, and Dublin Philosophical Magazine and Journal of Science* **11**, 65–80 (1931).
- <sup>80</sup>L. Novotny, *Principles of nano-optics*, edited by B. Hecht (Cambridge : Cambridge University Press, 2006, Cambridge, 2006).
- <sup>81</sup>T. Plakhotnik, E. A. Donley and U. P. Wild, 'Single-Molecule Spectroscopy and Dynamics at Room Temperature', *Annual Review of Physical Chemistry* **48**, 181–212 (1997).
- <sup>82</sup>A. Lewis, M. Isaacson, A. Harootunian and A. Muray, 'Development of a 500 Å spatial resolution light microscope. I. light is efficiently transmitted through  $\lambda/16$  diameter apertures', *Ultramicroscopy* **13**, 227–231 (1984).
- <sup>83</sup>D. W. Pohl, W. Denk and M. Lanz, 'Optical stethoscopy: Image recording with resolution  $\lambda/20$ ', *Applied Physics Letters* **44**, 651–653 (1984).
- <sup>84</sup>T. Enderle, T. Ha, D. F. Ogletree, D. S. Chemla, C. Magowan and S. Weiss, 'Membrane specific mapping and colocalization of malarial and host skeletal proteins in the Plasmodium falciparum infected erythrocyte by dual-color near-field scanning optical microscopy', *Proceedings of the National Academy of Sciences* **94**, 520–525 (1997).
- <sup>85</sup>H. Heinzelmann, T. Lacoste, T. Huser, H. J. Güntherodt, B. Hecht and D. W. Pohl, 'Instrumental developments and recent experiments in near-field optical microscopy', *Thin Solid Films* **273**, 149–153 (1996).
- <sup>86</sup>M. F. Garcia-Parajo, J. A. Veerman, A. G. T. Ruiter and N. F. Van Hulst, 'Near-field optical and shear-force microscopy of single fluorophores and DNA molecules', *Ultramicroscopy* **71**, 311–319 (1998).
- <sup>87</sup>E. Betzig, J. K. Trautman, T. D. Harris, J. S. Weiner and R. L. Kostelak, 'Breaking the Diffraction Barrier: Optical Microscopy of a Nanometric Scale', *Science* **251**, 1468–1470 (1991).
- <sup>88</sup>E. Betzig and R. Chichester, 'Single molecules observed by near-field scanning optical microscopy.', *Science* **262**, 1422–1425 (1993).

## Bibliography

- <sup>89</sup>J. M. Gerton, L. A. Wade, G. A. Lessard, Z. Ma and S. R. Quake, 'Tip-enhanced fluorescence microscopy at 10 nanometer resolution', *Physical Review Letters* **93**, 5–8 (2004).
- <sup>90</sup>E. Sánchez, L. Novotny and X. Xie, 'Near-Field Fluorescence Microscopy Based on Two-Photon Excitation with Metal Tips', *Physical Review Letters* **82**, 4014–4017 (1999).
- <sup>91</sup>B. I. Yakobson, A. Larosa, H. D. Hallen and M. A. Paesler, 'Thermal/optical effects in NSOM probes', *Ultramicroscopy* **61**, 179–185 (1995).
- <sup>92</sup>F. Zenhausern, Y. Martin and H. K. Wickramasinghe, 'Scanning interferometric apertureless microscopy: optical imaging at 10 angstrom resolution.', *Science (New York, N.Y.)* **269**, 1083–5 (1995).
- <sup>93</sup>R. Hillenbrand and F. Keilmann, 'Material-specific mapping of metal/semiconductor/dielectric nanosystems at 10 nm resolution by backscattering near-field optical microscopy', *Applied Physics Letters* **80**, 25–27 (2002).
- <sup>94</sup>A. Hartschuh, E. J. Sánchez, X. S. Xie and L. Novotny, 'High-Resolution Near-Field Raman Microscopy of Single-Walled Carbon Nanotubes', *Physical Review Letters* **90**, 095503 (2003).
- <sup>95</sup>N. Hayazawa, Y. Saito and S. Kawata, 'Detection and characterization of longitudinal field for tip-enhanced Raman spectroscopy', *Applied Physics Letters* **85**, 6239–6241 (2004).
- <sup>96</sup>J. S. Lloyd, A. Williams, R. H. Rickman, A. McCowen and P. R. Dunstan, 'Reproducible electrochemical etching of silver probes with a radius of curvature of 20 nm for tip-enhanced Raman applications', *Applied Physics Letters* **99**, 1–4 (2011).
- <sup>97</sup>W. Denk, J. H. Strickler and W. W. Webb, 'Two-photon laser scanning fluorescence microscopy.', *Science (New York, N.Y.)* **248**, 73–6 (1990).
- <sup>98</sup>Z. Ma, J. M. Gerton, L. A. Wade and S. R. Quake, 'Fluorescence near-field microscopy of DNA at Sub-10Å nm resolution', *Physical Review Letters* **97**, 1–4 (2006).
- <sup>99</sup>H. G. Frey, F. Keilmann, A. Kriele and R. Guckenberger, 'Enhancing the resolution of scanning near-field optical microscopy by a metal tip grown on an aperture probe', *Applied Physics Letters* **81**, 5030–5032 (2002).
- <sup>100</sup>H. G. Frey, S. Witt, K. Felderer and R. Guckenberger, 'High-resolution imaging of single fluorescent molecules with the optical near-field of a metal tip', *Physical Review Letters* **93**, 1–4 (2004).

- <sup>101</sup>P. J. Schuck, D. P. Fromm, A. Sundaramurthy, G. S. Kino and W. E. Moerner, 'Improving the mismatch between light and nanoscale objects with gold bowtie nanoantennas', *Physical Review Letters* **94**, 14–17 (2005).
- <sup>102</sup>C. Mu, B. D. Mangum, C. Xie and J. M. Gerton, 'Nanoscale Fluorescence Microscopy Using Carbon Nanotubes', *IEEE Journal of Selected Topics in Quantum Electronics* **14**, 206–216 (2008).
- <sup>103</sup>E. Shafran, B. D. Mangum and J. M. Gerton, 'Energy transfer from an individual quantum dot to a carbon nanotube', *Nano Letters* **10**, 4049–4054 (2010).
- <sup>104</sup>C. Höppener and L. Novotny, 'Antenna-based optical imaging of single Ca<sup>2+</sup> transmembrane proteins in liquids.', *Nano Letters* **8**, 642–646 (2008).
- <sup>105</sup>T. Härtling, P. Reichenbach and L. M. Eng, 'Near-field coupling of a single fluorescent molecule and a spherical gold nanoparticle', *Optics Express* **15**, 12806–12817 (2007).
- <sup>106</sup>R. Reisfeld, M. Grinberg, V. Levchenko, B. Kukliński, S. Mahlik, S. Magdassi and M. Grouchko, 'Sol-gel glasses with enhanced luminescence of laser dye Rhodamine B due to plasmonic coupling by copper nanoparticles', *Optical Materials* (2013) **10**. 1016/j.optmat.2013.11.011.
- <sup>107</sup>R. Reisfeld, V. Levchenko, F. Piccinelli and M. Bettinelli, 'Amplification of light emission of chiral pyridine Eu(III) complex by copper nanoparticles', *Journal of Luminescence* **170**, 820–824 (2016).
- <sup>108</sup>R. Reisfeld, V. Levchenko, A. Lazarowska, S. Mahlik and M. Grinberg, 'Intensification of luminescence of Europium-EDTA complex in polyvinyl pyrrolidone films by copper nanoparticles', *Optical Materials* **59**, 3–7 (2016).
- <sup>109</sup>R. Reisfeld, T. Saraidarov, G. Panzer, V. Levchenko and M. Gaft, 'New optical material europium EDTA complex in polyvinyl pyrrolidone films with fluorescence enhanced by silver plasmons', *Optical Materials* **34**, 351–354 (2011).
- <sup>110</sup>R. Reisfeld, M. Pietraszkiewicz, T. Saraidarov and V. Levchenko, 'Luminescence intensification of lanthanide complexes by silver nanoparticles incorporated in sol-gel matrix', *Journal of Rare Earths* **27**, 544–549 (2009).

## Bibliography

- <sup>111</sup>V. Levchenko, M. Grouchko, S. Magdassi, T. Saraidarov and R. Reisfeld, 'Enhancement of luminescence of Rhodamine B by gold nanoparticles in thin films on glass for active optical materials applications', *Optical Materials* **34**, 360–364 (2011).
- <sup>112</sup>P. Eaton and P. West, *Atomic Force Microscopy*: (Oxford University Press, Mar. 2010).
- <sup>113</sup>G. Meyer and N. M. Amer, 'Novel optical approach to atomic force microscopy', *Applied Physics Letters* **53**, 1045–1047 (1988).
- <sup>114</sup>T. Göddenhenrich, 'Force microscope with capacitive displacement detection', *Journal of Vacuum Science & Technology A: Vacuum, Surfaces, and Films* **8**, 383 (1990).
- <sup>115</sup>D. Rugar, H. J. Mamin and P. Guethner, 'Improved fiber-optic interferometer for atomic force microscopy', *Applied Physics Letters* **55**, 2588–2590 (1989).
- <sup>116</sup>F. J. Giessibl, 'High-speed force sensor for force microscopy and profilometry utilizing a quartz tuning fork', *Applied Physics Letters* **73**, 3956–3958 (1998).
- <sup>117</sup>R. Wiesendanger, 'Scanning force microscopy (SFM)', in *Scanning probe microscopy and spectroscopy: methods and applications* (Cambridge University Press, Cambridge, 1994), pp. 210–264.
- <sup>118</sup>P. K. Hansma et al., 'Tapping mode atomic force microscopy in liquids', *Applied Physics Letters* **64**, 1738–1740 (1994).
- <sup>119</sup>J. P. Cleveland, B. Anczykowski, A. E. Schmid and V. B. Elings, 'Energy dissipation in tapping-mode atomic force microscopy', *Applied Physics Letters* **72**, 2613–2615 (1998).
- <sup>120</sup>G. Oncins and J. Díaz-Marcos, 'Atomic Force Microscopy : probing the Nanoworld', *Handbook of instrumental techniques from CCiTUB* (2012).
- <sup>121</sup>B. Pittenger, N. Erina and C. Su, 'Quantitative Mechanical Property Mapping at the Nanoscale with PeakForce QNM', *Burker Application Note* **128**, 1–12 (2009).
- <sup>122</sup>B. V. Derjaguin, V. M. Muller and Y. U. P. Toporov, 'Effect of contact deformation on the adhesion of particles.', *Journal of colloid and interface science* **52**, 105–108 (1975).
- <sup>123</sup>D. B. Murphy, *Fundamentals of light microscopy and electronic imaging* (New York : Wiley, 2001, New York, 2001).
- <sup>124</sup>J. R. Lakowicz, *Principles of Fluorescence Spectroscopy* (Springer US, 2007).

- <sup>125</sup>J. Kapuscinski, 'DAPI: a DNA-Specific Fluorescent Probe', *Biotechnic & Histochemistry* **70**, 220–233 (1995).
- <sup>126</sup>J. A. Cooper, 'Effects of cytochalasin and phalloidin on actin.', *The Journal of Cell Biology* **105**, 1473 LP –1478 (1987).
- <sup>127</sup>M. W. Fishburn, 'Fundamentals of CMOS single-photon avalanche diodes', Massachusetts Institute of Technology **Thesis** (2012).
- <sup>128</sup>F. Zappa, S. Tisa, A. Tosi and S. Cova, 'Principles and features of single-photon avalanche diode arrays', *Sensors and Actuators, A: Physical* **140**, 103–112 (2007).
- <sup>129</sup>Spcm-Aqr Series, 'Single Photon Counting Module', Biomedical Solutions Datasheet, [http://sites.fas.harvard.edu/phys191r/Bench\\_Notes](http://sites.fas.harvard.edu/phys191r/Bench_Notes) (2007).
- <sup>130</sup>M. Lanzagorta, *Introduction to reconfigurable supercomputing [electronic resource]*, edited by S. Bique and R. Rosenberg (San Rafael, Calif. 1537 Fourth Street, San Rafael, CA 94901 USA : Morgan & Claypool Publishers, c2009, San Rafael, Calif. (1537 Fourth Street, San Rafael, CA 94901 USA), 2010).
- <sup>131</sup>M. Gokhale, *Reconfigurable computing : accelerating computation with field-programmable gate arrays*, edited by P. S. Graham (New York : Springer-Verlag, 2005, New York, 2005).
- <sup>132</sup>S. Hauck and A. DeHon, *Reconfigurable Computing: The Theory and Practice of FPGA-Based Computation*, Systems on Silicon (Elsevier Science, 2010).
- <sup>133</sup>E. Tlelo-Cuautle, J. d. J. Rangel-Magdaleno and L. G. la Fraga, 'Introduction to Field-Programmable Gate Arrays', in *Engineering applications of fpgas: chaotic systems, artificial neural networks, random number generators, and secure communication systems* (Springer International Publishing, Cham, 2016), pp. 1–32.
- <sup>134</sup>J. V. Chacko, F. C. Zanicchi and A. Diaspro, 'Probing cytoskeletal structures by coupling optical superresolution and AFM techniques for a correlative approach', *Cytoskeleton* **70**, 729–740 (2013).
- <sup>135</sup>G. Maubach and W. Fritzsche, 'Precise positioning of individual DNA structures in electrode gaps by self-organization onto guiding microstructures', *Nano Letters* **4**, 607–611 (2004).
- <sup>136</sup>J. Doke, 'Ginputc', version 1.0.0.1, <https://uk.mathworks.com/matlabcentral/fileexchange> (2012).

## Bibliography

- <sup>137</sup>J. K. Hobbs, T. J. McMaster, M. J. Miles and P. J. Barham, 'Direct observations of the growth of spherulites of poly(hydroxybutyrate-co-valerate) using atomic force microscopy', *Polymer* **39**, 2437–2446 (1998).
- <sup>138</sup>Y. Xie, Y. Li, L. Xiao, Q. Qiao, R. Dhakal, Z. Zhang, Q. Gong, D. Galipeau and X. Yan, 'Femtosecond Time-Resolved Fluorescence Study of P3HT / PCBM Blend Films', *Journal of Physical Chemistry*, 14590–14600 (2010).
- <sup>139</sup>M. Li, P. Xu, J. Yang and S. Yang, 'Donor- p -acceptor double-cable polythiophenes bearing fullerene pendant with tunable donor / acceptor ratio : A facile postpolymerization †', *Journal of Materials Chemistry*, 3953–3960 (2010).
- <sup>140</sup>M. L. Petrus, R. K. M. Bouwer, U. Lafont and D. H. K. Murthy, 'Polymer Chemistry optoelectronic properties', *Polymer Chemistry*, 4182–4191 (2013).
- <sup>141</sup>N. Otsu, 'A threshold selection method from gray-level histograms', *IEEE Transactions on Systems, Man, and Cybernetics* **9**, 62–66 (1979).
- <sup>142</sup>R. O. Duda, *Pattern classification and scene analysis*, edited by P. E. Hart and P. E. Hart (New York Chichester : Wiley-Interscience, 1973, New York Chichester, 1973).
- <sup>143</sup>A. Goshtasby, S. H. Gage and J. F. Bartholic, 'A Two-Stage Cross Correlation Approach to Template Matching', *IEEE Transactions on Pattern Analysis and Machine Intelligence* **PAMI-6**, 374–378 (1984).
- <sup>144</sup>D. I. Barnea and H. F. Silverman, 'A Class of Algorithms for Fast Digital Image Registration', *IEEE Transactions on Computers* **C-21**, 179–186 (1972).
- <sup>145</sup>S. D. Wei and S. H. Lai, 'Fast Template Matching Based on Normalized Cross Correlation With Adaptive Multilevel Winner Update', *IEEE Transactions on Image Processing* **17**, 2227–2235 (2008).

# A

---

## ALIGNING THE TIP-ENHANCED FLUORESCENCE MICROSCOPE: AN ALTERNATIVE METHOD INCORPORATING LOCK-IN AMPLIFICATION

---

### A.1 INTRODUCTION

It was shown earlier in this thesis that a method has been developed to align the tip-enhanced fluorescence microscope based upon analysing fluorescence and atomic force microscope (AFM) images which have been simultaneously acquired. By determining the offset between the fields-of-view of the two images, the distance between the incident excitation beam and the AFM-tip can be estimated and corrected for using a 2D galvanometer.

Prior to the development of this method, various other techniques were trialled to align the AFM-tip with the excitation laser. The introduction of a galvanometer into the optical set-up was crucial in all of the methods tested. A galvanometer enables the position of the incident focussed laser spot to be controlled, allowing the excitation laser to be snaked across the area where the AFM-tip was thought to be.

An initial alignment method was designed which aimed to exploit the enhancement effect itself in order to determine the position of the AFM-tip. With the AFM-tip located within 10 nm of a fluorescent emitter, it should be the case that an increased number of photons will be detected from this location, only when the incident beam becomes aligned with the AFM-tip. Therefore, if the incident excitation spot is snaked across the area of the tip, and photons are simultaneously counted, a fluorescence image can be developed in which the location of the AFM-tip should manifest itself as a hot-spot of photon counts. A schematic of this concept can be seen in Figure A.1.

When this experiment was trialled, no hotspots were seen within the photon count map. One possible explanation for this was that the enhancement signal itself was small compared to the background. The enhancement is present over an area which is approximately the

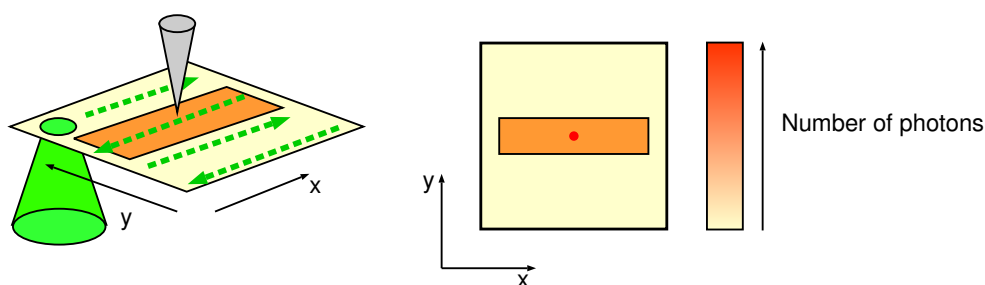


Figure A.1.: Initial experiments to locate AFM-tip. Left: the experimental setup. AFM-tip (grey) is incident on a fluorescent polymer (shown in orange). Incident laser spot (green) is made to snake across the sample, over the area where the AFM-tip is positioned. Right: photons corresponding to each laser position are counted and output as a photon map. The presence of the AFM-tip will have enhanced fluorescence emission from a localised area, producing a hot-spot (red) which is brighter than the surrounding fluorescence.

size of the apex of the AFM-tip, whereas the magnitude of the background signal will be related to the size of the excitation beam: the larger the excitation beam, the more fluorescent molecules that will be emitting light. Given the relative sizes of the AFM-tip and the excitation beam, the signal-to-noise ratio (enhanced fluorescence to normal fluorescence) will be extremely small.

For this reason, a lock-in amplifier was introduced into the hardware. These instruments are used for detecting signals of a known frequency which are small in magnitude, and would otherwise be difficult to detect amongst sources of noise.

## A.2 THEORY

### A.2.1 Lock-In Amplification

Lock-in amplification is a technique used for detecting signals of interest which have a small amplitude, and which may usually be lost amongst large amplitudes of noise or interference. Lock-in amplification (also called synchronous detection) relies upon prior knowledge of the signal that the user is attempting to detect - usually the frequency of the signal.

A lock-in amplifier exploits the mathematics of combining two oscillating signals. The amplifier is made up of a signal multiplier, followed by a low-pass filter. The detector is supplied with two signals: one is a reference signal  $R(t)$  which has a frequency  $\omega_R$  (equal to the signal of

interest), and the other is the signal obtained from the experiment  $s(t)$  which will contain both the signal of interest and the additional noise and interference components. Assuming that the two signals can be represented by oscillating voltages each with a particular frequency and phase, they can be written in terms of their rms voltages  $V_R$  and  $V_s$ :

$$R(t) = \sqrt{2}V_R \cos[\omega_R t + \phi_R] \quad (\text{A.1})$$

$$s(t) = \sqrt{2}V_s \cos[\omega_s t + \phi_s] \quad (\text{A.2})$$

In this case, their product  $V_p(t)$  can be written as the sum of two cosine waves. One cosine wave has a frequency at the sum of the two individual frequencies, and the other has a frequency equal to the frequency difference of the two:

$$V_p(t) = 2V_R V_s \cos[(\omega_R + \omega_s)t + \phi_R + \phi_s] + 2V_R V_s \cos[(\omega_R - \omega_s)t + \phi_R - \phi_s] \quad (\text{A.3})$$

The product  $V_p(t)$  of the two input signals is then passed through a low-pass filter. The cut-off frequency of the low-pass filter is chosen such that its value is much less than the frequency of the reference signal [1]. Since the term  $(\omega_R + \omega_s)$  will always be equal to or larger than  $\omega_R$ , the first cosine term in  $V_p(t)$  is filtered out by the low pass filter, leaving just the second cosine term: an oscillating voltage with a frequency  $|\omega_R - \omega_s|$ . The greater the difference between the frequencies of the two input signals, the greater the frequency of their product. Due to the presence of the low-pass filter, these high frequencies will be removed, and the output of the lock-in amplifier will therefore be closer to zero for signals which differ greatly in frequency. Crucially, when the frequency of the signal from the experiment ( $\omega_s$ ) is equal to the reference frequency ( $\omega_R$ ), the frequency of the second cosine term in  $V_p(t)$  becomes zero; a non-oscillating DC result is achieved.

This technique essentially gives a means of comparing the signal from an experiment with a reference signal. By locking-in to the expected frequency of the signal, all high voltage noise and interference which are at a frequency different to the signal of interest will be attenuated by the lock-in amplifier. If the DC component of the output is large, this means that a large amount of the experimental signal is

at the expected frequency. This DC component is also known as the *R-value*, and is read directly from the lock-in amplifier through a BNC output. The lock-in amplifier used in this investigation was a USB lock-in by Anfatec.

### A.2.2 *Experimental Hypothesis*

For this experiment, a number of assumptions are made. The main assumption is that when light is incident on an object which is oscillating at a particular frequency, the scattered light from the object will also have a strong frequency component at that of oscillation. Relating this to the experiment in this thesis, it is expected that any light scattered from the AFM-tip will have a large frequency component at 1 kHz: the frequency of tip oscillation when the AFM is operated in PeakForce quantitative nanomechanical mapping (QNM) mode.

This experimental set-up will therefore be similar to that shown in Figure A.1, but instead of counting the number of photons, the frequencies in the photon-counting signal will be analysed using a lock-in amplifier. The reference signal will be that of PeakForce tapping (1 kHz). It is hypothesised that, if a map of the lock-in output signal relative to incident beam position can be produced (rather than the map of photon counts shown in Figure A.1), the highest output will be seen at the location of the AFM-tip. Like the experiment described earlier, this may manifest itself as a hot-spot since the lock-in amplifier produces its highest output voltage (*R-value*) when the input signal (scattered photon signal) has a frequency which is closest to the reference frequency.

## A.3 METHOD

### A.3.1 *Experimental Arrangement*

The experimental set-up in terms of the hardware remains the same as for the rest of this thesis (see Figure 4.1), with some additional hardware components added to analyse the output of the single photon counting module (SPCM). The only difference is that the fluorescence filter (570 nm LP) is removed for this experiment, because the scatter of the incident laser beam ( $\lambda = 532$  nm) is being measured.

Since the SPCM output is actually a signal of TTL pulses with each pulse representing the detection of one photon, the output should be filtered before being input to the lock-in amplifier. If the hypothesis

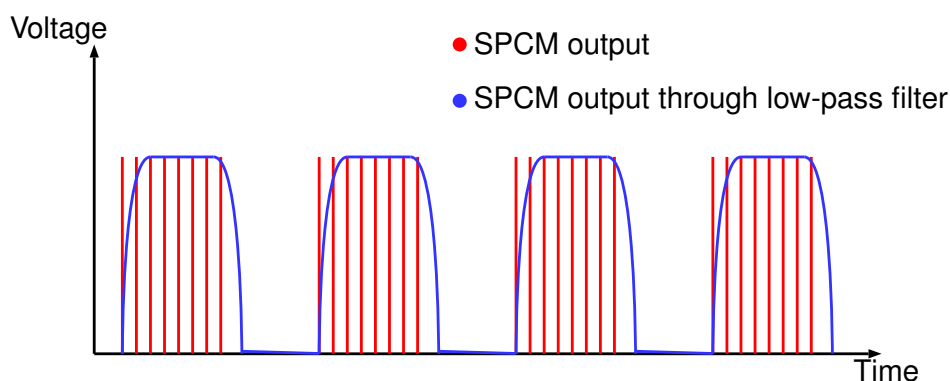


Figure A.2.: Diagram to show filtering effect on SPCM output. Red signal shows typical output from the SPCM, with each individual TTL pulse signifying one detected photon. It is assumed that TTL pulses will group together at the frequency of tip-oscillation as photons are scattered. If a low-pass filter is applied, the output could be smoothed to obtain the signal depicted in blue, ready for input to the lock-in amplifier.

outlined in Section A.2.2 is correct, photons will be reflected at a frequency equal to that of tip oscillation and a SPCM output similar to that depicted in red in Figure A.2 may be expected, in which individual photons are grouped together at the frequency of tip-oscillation. Therefore applying a low-pass filter with a cut-off frequency around 3 kHz should smooth the output towards that depicted in blue in Figure A.2. This filtered output would be a signal which should have a frequency approximately equal to the expected scattering frequency. Further away from the  $(x,y)$  tip position, a sporadic stream of TTL pulses would be expected. This filtered signal will be supplied to the lock-in amplifier for frequency analysis. In this experiment, a pre-amplifier (Stanford Research Systems SR560) was used to filter the SPCM output signal.

Regarding the reference signal, the lock-in amplifier used in this investigation has an option to lock in to a sinusoidal input, which makes it compatible for locking-in with the AFM z-voltage output from the SAM-V (signal access module). This output is analogous to the z-position of the AFM-tip, and therefore has a frequency equal to tip-oscillation. However, the lock-in amplifier expects a sinusoidal signal centred around 0 V. To achieve this, a signal conditioner was developed, as outlined in the following section.

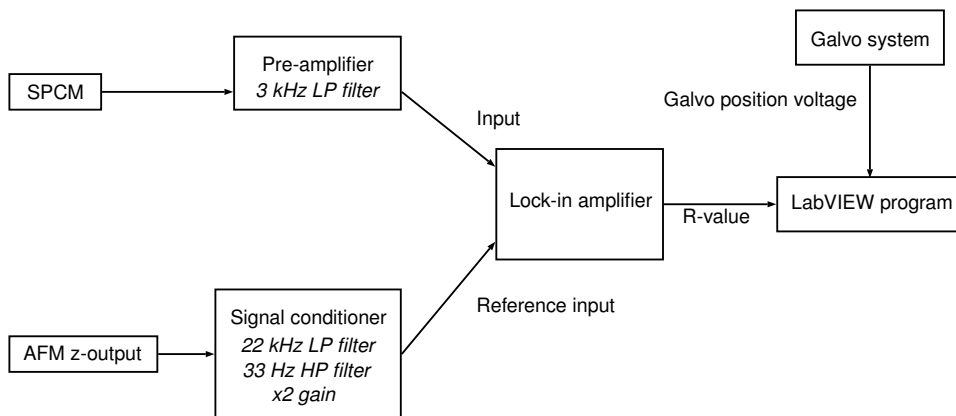


Figure A.3.: Schematic of experimental set-up for aligning AFM-tip with excitation laser using the lock-in amplifier. Both the SPCM output and the AFM z-output (analogous to tip position) are filtered before being input to the lock-in amplifier. The final LabVIEW program records the (x,y) voltage that has been sent to the galvanometer (galvo system) and the R-value that has been measured at that particular position, whilst the galvanometer is made to snake the laser spot across the AFM-tip.

Following the development of the signal conditioner, the PeakForce frequency of AFM operation could consistently be locked-in by the amplifier through the reference input. A program similar to that described in Section 4.2.3 was created to control the position of the incident focussed laser spot. LabVIEW was used to apply a variable voltage to the two axes of the 2D galvanometer such that the incident laser spot would snake across the sample. The R-value output from the lock-in amplifier was read at every position allowing a map to be built up of R-value against the supplied galvanometer (x,y) voltage. A flow diagram indicating the final filtering process is depicted in Figure A.3.

### A.3.2 *Developing a Signal-Conditioner to Assist Lock-In Amplification*

It was described in Section A.3.1 that a signal conditioner needed to be developed as an additional piece of hardware, in order to remove the DC offset from the z-voltage signal of the AFM, and allow the reference signal to be locked in by the amplifier. Following further investigation with an oscilloscope, it was found that the output amplitude of the z-voltage from the SAM-V was close to the minimum amplitude required for locking in (a minimum of  $\pm 35$  mV). For this reason, it was

decided that the signal conditioner should also amplify the z-voltage output to ensure that consistent locking-in could be achieved. Knowing that the maximum tapping frequency for PeakForce QNM mode is 1 kHz, a final low-pass filter was added to the design to remove any high frequency noise from the AFM signal.

To create the signal conditioner, a circuit diagram was first designed using EAGLE PCB (printed circuit board) design software. Using the same software, a schematic of the board layout could then be generated. The final circuit diagram can be seen in Figure A.4. The production process for the amplifier was as follows; the board schematic was printed onto a sheet of acetate, which was then taped to the top of the PCB (so that it was in contact with the photoresist layer). With the acetate in place, the board was then exposed to an ultraviolet lamp for two minutes. Following exposure, the schematic was developed by placing the board in a NaOH solution (5 g/l in water) for around 6 minutes. The PCB was then washed with water and dried with nitrogen, ready for etching. Etching was performed in an ammonium persulfate solution ( $(\text{NH}_4)_2\text{S}_2\text{O}_8$  220 g/l in water). The PCB board was submerged into the solution for around 90 minutes, allowing the copper to dissolve in areas which had previously been exposed to the ultraviolet light. The remaining copper layer formed the electronic circuit. The PCB was removed from the etching solution, rinsed with water, and then rinsed further by isopropanol to make sure that all of the etching solution, along with any stubborn pieces of photoresist, had been removed from the board. Care was taken when handling the final etched PCB not to scratch the surface of the board with tweezers. Components were soldered to the PCB and the final board was inserted into an aluminium enclosure for protection.

To test that the signal conditioner was working, the AFM was operated in PeakForce QNM mode and the frequency was varied between 0.25 kHz, 0.5 kHz and 1 kHz, with the response of the lock-in amplifier being monitored using the supplied software. The detected frequency of the reference signal was found to match the PeakForce frequency on the AFM software in all cases, and the signal could consistently be locked-in for prolonged periods of time, even with fluctuations in the DC offset of the raw z-voltage signal.

#### A.4 RESULTS

The galvanometer was made to scan the focussed laser spot across the area of the AFM-tip by varying the voltages of its x- and y-axis accordingly. A clear glass slide was positioned at the sample stage, allowing

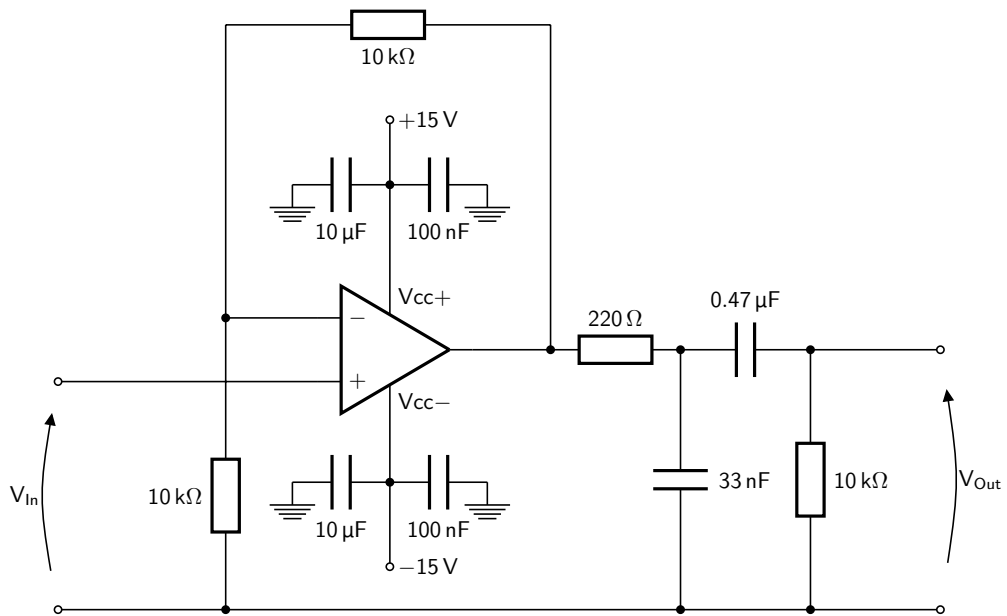


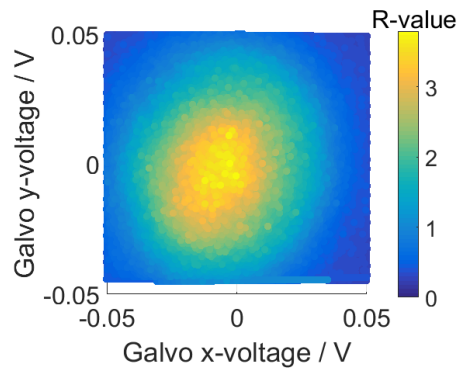
Figure A.4.: Circuit diagram for final signal conditioner. An operational amplifier chip was used to increase the gain by a factor of 2. The output of the amplifier was then filtered, first by a low-pass ( $\approx 22$  kHz) and then a high-pass (33 Hz) filter, to target the 1 kHz signal of tip-oscillation whilst removing DC and very high-frequency noise components.

the AFM-tip to engage with a surface. A scan size of zero microns was chosen to limit additional scatter from the motion of the sample. With the low-pass filtered output from the SPCM being input to the lock-in amplifier, along with the reference signal of the z-position of the AFM-tip, the R-value output from the lock-in amplifier was recorded and plotted against the corresponding galvanometer voltages. Examples of these plots can be seen in Figure A.5.

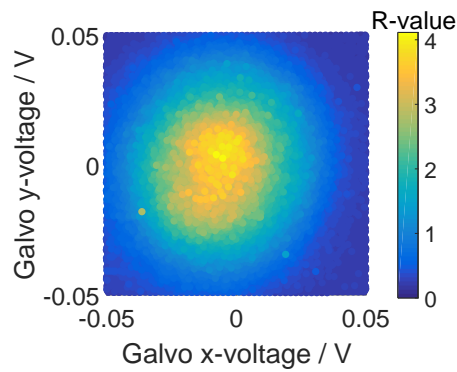
Figure A.5a shows the results of the R-value map with respect to the applied galvanometer (x,y) voltage when the AFM-tip was aligned in the detection area of the SPCM. These results were taken by moving the incident laser across the glass slide at a rate of one line per 10 seconds, with one line covering a length of approximately 7  $\mu\text{m}$ . At first, these results look promising. There is a definite area of high R-value in the centre of the image, leading to the assumption that this is where the highest proportion of the photon count signal is at the frequency of the reference signal. This could mean that light is scattered strongest at 1 kHz here, and that this could be where the AFM-tip is located. The results do not look exactly as expected however. One might expect that a very discrete area with a high R-value will be present, whereas elsewhere the R-value will be an approximately constant and very low value. A very gradual reduction in R-value is seen here from the centre of the image towards the edges.

To double check that this area of high R-value was dependent on AFM-tip position, the tip was moved far away from the incident beam and data was acquired once again, the results of which can be seen in Figure A.5b. It can be seen that, despite the lack of the AFM-tip in the field-of-view, this same area of high R-value is present in the image: an unexpected result. For comparison, Figure A.5c shows a similar map of the number of photons counted for each galvanometer orientation, taken immediately before data acquisition with the lock-in amplifier. Comparing this image to the R-value maps in Figure A.5, it seems that the area of highest R-value corresponds to the area with greatest number of detected photons.

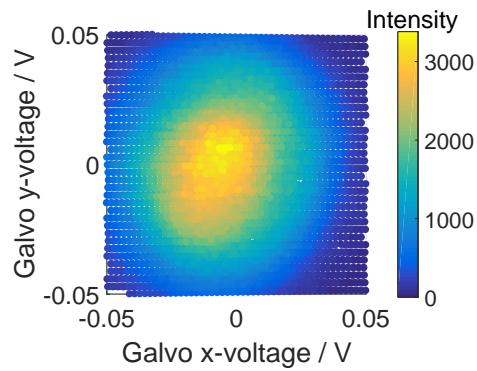
To investigate this further, a sample of aforementioned phase-separated P<sub>3</sub>HT-polystyrene polymer blend was imaged using the AFM. The output signal from the SPCM was split using a BNC t-junction, with one part of this split signal being input to the AFM hardware for the simultaneous fluorescence imaging described throughout this thesis. The other portion however, was filtered and input to the lock-in amplifier as described in Section A.3.1, along with the reference signal of the z-voltage. The output signal of the lock-in amplifier was then input to the AFM hardware in the same way as the output of the SPCM.



(a)



(b)



(c)

Figure A.5.: R-values and intensity plotted against galvanometer (x,y) voltages (analogous to incident laser position) for the case where the AFM-tip is aligned in the collection area (a) and where the AFM-tip has been misaligned (b). Also shown in (c) for comparison is the photon counts (intensity) plotted against galvanometer (x,y) voltages, acquired immediately before lock-in amplification data.

The aim of this was to simultaneously produce images of AFM height, fluorescence count and R-value for the sample to determine their relationship. For imaging, the fluorescence filter (570 nm LP) was replaced back into the set-up. The results of this experiment can be seen in Figure A.6. This figure shows that the same details are found in all images, including the R-value image: this is strong evidence that the R-value is dependent mostly on the number of photons being detected, rather than the position of the incident laser beam relative to the AFM-tip (both of which are stationary during this type of data acquisition).

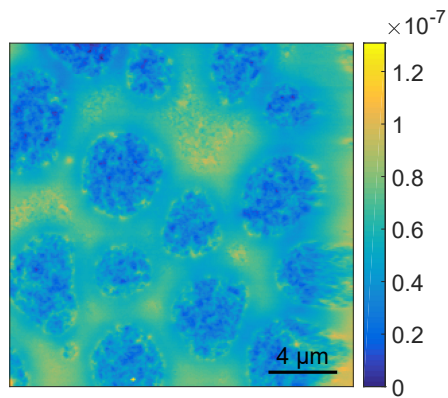
Further evidence of this can be seen in Figure A.7. For this data, AFM and R-value images were obtained simultaneously, again of the phase-separated P<sub>3</sub>HT sample (seen in the top two images of the figure). However, following this acquisition, the AFM-tip was withdrawn and the AFM was operated in *false engage* mode. This enabled an R-value image of the same area of sample as previous to be obtained with the tip withdrawn from the sample and also not oscillating in the z-direction. This R-value image can be seen in Figure A.7c. The same features can be seen in this new R-value image as in the previous R-value image where the tip was engaged above the sample. Moreover, the R-value has broadly stayed the same (or may have even slightly increased) for the case where the tip is withdrawn from the surface. This is a curious result, because it implies that the R-value is not at all dependent on tip-oscillation or tip location.

#### A.5 DISCUSSION

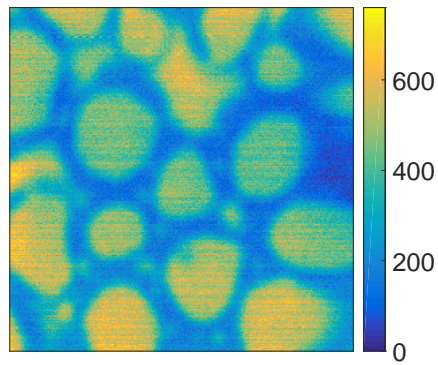
The original objective of the experiment in this chapter was to determine whether or not lock-in amplification could be used to aid alignment between a focussed excitation beam and an AFM-tip, to induce fluorescence enhancement in the current microscope.

It was thought that, as the focussed excitation beam is moved around underneath the sample, the point at which it is incident on the oscillating AFM-tip would be the point at which the largest number of photons would be scattered at the oscillation frequency. By setting the reference signal for the lock-in amplifier to this frequency, a high R-value should be achieved only at the position of the AFM-tip, with an approximately-constant low value elsewhere across the sample. However, the results presented in this chapter are not as expected.

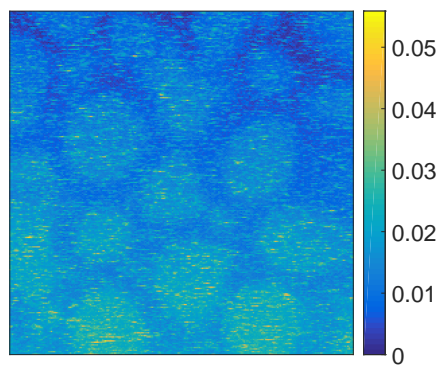
It has been shown in all results that the R-value tends to have large dependence only on the number of photons being detected. The particularly unusual result however is that the R-value in this experiment



(a)

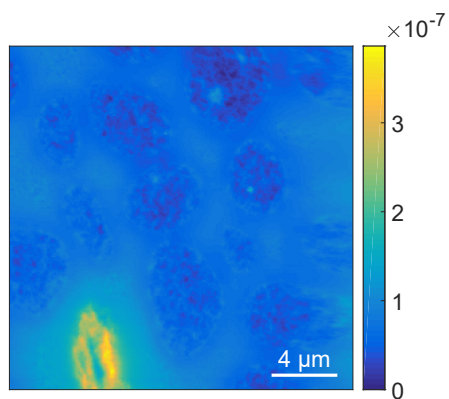


(b)

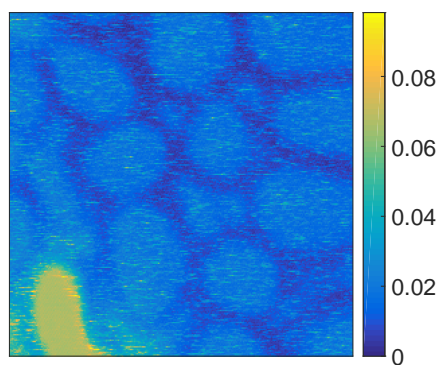


(c)

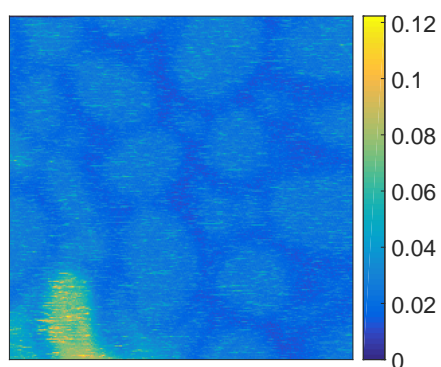
Figure A.6.: Images of a sample of P3HT captured simultaneously. Shown are AFM-height image (a), fluorescence image (b), and R-value image (c) from the output of the lock-in amplifier.



(a)



(b)



(c)

Figure A.7.: Images of a sample of P3HT polymer blend. AFM-height (a) and R-value (b) images taken simultaneously. Following this, the AFM-tip was withdrawn and an isolated R-value image was obtained without the tip oscillating: the results of this can be seen in (c).

has seemingly no dependence whatsoever on the tip-oscillation frequency, with practically the same result being achieved when the AFM-tip was engaged compared to when the AFM-tip was withdrawn. The R-value is a voltage whose magnitude can be thought of as the similarity in frequency between the SPCM output and AFM-tip oscillation. Therefore vastly different R-values should be expected between the case where the AFM-tip is engaged and oscillating at 1 kHz, and the case where the AFM-tip is withdrawn and not oscillating.

There were a number of assumptions made in the creation of this experiment, with the main assumption being that the AFM-tip would scatter photons at the frequency at which it oscillates. It was thought that this might manifest as 1 kHz pulses in the output signal of the SPCM, in which TTL pulses are grouped together. It could be the case that the AFM-tip does not scatter a substantial number of photons to have an affect on the output of the SPCM, especially amongst the large background signal. This explanation is feasible given the very small size of the tip-apex<sup>1</sup> over which to scatter photons. Although this could be due to an error in the theory, hardware issues cannot be ruled out as a potential flaw in this experiment. It could be that the TTL signal from the SPCM is not a suitable signal to be locked-in with the amplifier, even with the additional filtering steps applied to it. Further investigations should trial replacing the SPCM with a conventional photodiode, producing an analogue output proportional to the number of photons that have been detected. An example of a similar set-up can be found [2]. Direct fluctuations in the analogue signal due to scatter from the AFM-tip may be more optimum for lock-in amplification.

## A.6 CONCLUSION

This chapter has outlined a theoretical method using lock-in amplification for aligning a focussed laser spot with the tip of an atomic force microscope, the requirement for inducing fluorescence-enhancement in the current microscope.

An experiment was designed in which the 2D galvanometer can be used to vary the incident position of the excitation beam around the area where the AFM-tip is thought to be. It is assumed that the incident laser beam will be scattered strongly by the oscillating tip when the two are aligned, and that this may manifest itself as pulsing within the SPCM output signal.

---

<sup>1</sup> average of 7 nm radius for the probes in use

All results obtained in this initial experiment indicate that the output of the lock-in amplifier is not affected by the presence of the AFM-tip, but more the number of photons being detected at the particular area due to the alignment between the light pathways in the microscope. This result is surprising, and could indicate a problem with either the theory or the experimental set-up. It is likely that, given the small size of the tip-apex, the scatter of light by the AFM-tip is too small to have an effect on the TTL output signal from the SPCM and that this is the reason why this technique has not been successful. Future investigations should replace the SPCM with a detector capable of outputting an analogue signal proportional to the number of photons detected (such as a photodiode) to see whether the experimental arrangement can be improved. It is inconclusive whether this method could eventually be used as a technique for aligning a tip-enhanced fluorescence microscope, but the results of this experiment have been interesting and could warrant further research; it would be useful to find as many techniques as possible for aligning a tip-enhanced fluorescence microscope, making the technique attainable with differing resources and varying budgets.

## REFERENCES

- <sup>1</sup>M. L. Meade, *Lock-in amplifiers: principles and applications*, 1 (Mike Meade, 1983).
- <sup>2</sup>S. G. Stanciu, D. E. Tranca, C. Ruggiero, G. A. Stanciu, E. Dellacasa, A. Antipov, R. Hristu and L. Pastorino, 'Combined far-field, near-field and topographic imaging of nano-engineered polyelectrolyte capsules', *Materials Letters* **183**, 105–108 (2016).